Crustal displacements in Greenland caused by ice mass variability

Nielsen, Karina; Forsberg, René; Khan, Shfaqat Abbas; Knudsen, Per

Publication date:
2012

Document Version
Publisher's PDF, also known as Version of record

Citation (APA):
Nielsen, K., Forsberg, R., Khan, S. A., & Knudsen, P. (2012). Crustal displacements in Greenland caused by ice mass variability. Kgs. Lyngby: Technical University of Denmark (DTU).

Crustal displacements in Greenland caused by ice mass variability

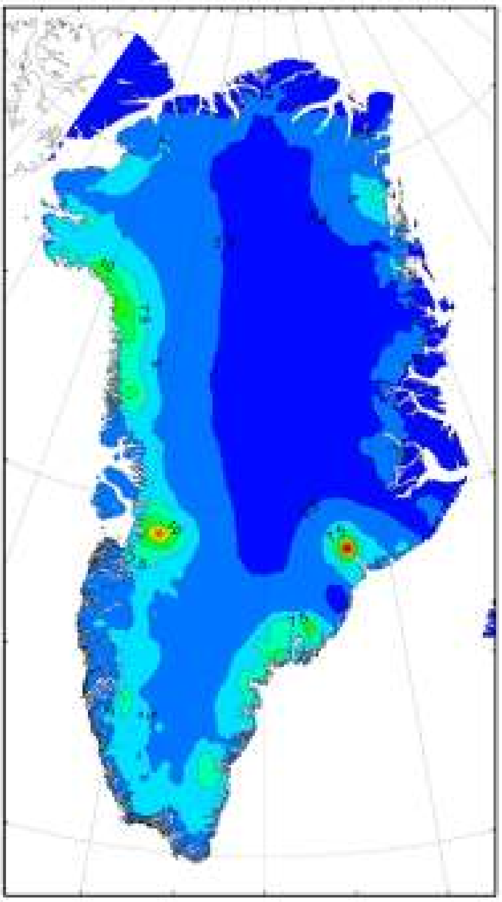

Ph.D. thesis

Karina Nielsen

DTU Space - National Space Institute
August 2012

Crustal displacements in Greenland caused by ice mass variability

Ph.D. thesis

Karina Nielsen
Department of Geodesy
DTU Space

Supervisor:	Shfaqat Abbas Khan, DTU Space
Co-supervisor:	Per Knudsen, DTU Space
	René Forsberg, DTU Space

Karina Nielsen
Department of Geodesy
DTU Space
Elektrovej bygn. 327
DK–2800 Kgs. Lyngby
Denmark
Phone: (+45) 4525–9764
Email: `karni@space.dtu.dk`

Preface

This thesis has been submitted to the Technical University of Denmark (DTU) as part of the requirements for obtaining the PhD degree. The research presented in this thesis has been carried out at the Department of Geodesy at DTU Space with Shfaqat Abbas Khan as the main supervisor and Per Knudsen and René Forsberg as co-supervisors. The research was funded by KVUG (Kommissionen for Videnskabelige Undersøgelser i Grønland) and DTU. In this PhD project data from GNET (Greenland GPS Network) was used. GNET is funded by NSF (National Science fondation) and co-funded by DTU. UNAVCO is responsible for hardware and the GPS sites have been established by UNAVCO, Ohio State University and DTU-Space. This thesis includes four scientific papers; Sørensen et al. (2011), Nielsen et al. (2012a), Nielsen et al. (2012b), and Nielsen et al. (2012c).

I would like to thank my three supervisors for excellent supervision, especially Shfaqat Abbas Khan, for his dedication to this PhD project. I would also like to thank all my colleagues and coauthors who have been a part of this thesis, especially Louise S. Sørensen for a great collaboration. I would also like to thank Valentina Barletta for good discussions about elastic uplift modeling and glacial isostatic adjustment. Also thanks to Stine Kildegaard Rose and Emil Nielsen for proof reading of parts of the thesis.

During the PhD project, I visited prof. Giorgio Spada for two month at Dipartimento di Scienze di Base e Fondamenti (DiSBeF), Università di Urbino "Carlo Bo", Urbino, Italy. Giorgio Spada has been a true source of inspiration, and we have had a great collaboration during this PhD, which hopefully will continue in the future. I would like to thank Giorgio Spada and his colleagues for having me at their department and for introducing me to true Italian hospitality. I would also like to thank my family for joining me at this trip, without them it would not have been possible.

Thanks to my supervisor Shfaqat Abbas Khan I had the opportunity to visit Greenland and experience glaciers including Jakobshavn Isbræ up close. This experience have given me a better understanding of my estimates.

Finally, I would like to thank family for supporting me and in particular Anders for his never failing love and support, and for taking care of our three wonderful children Cathrine, Victor, and Oscar during this at time work demanding process.

Kgs. Lyngby, August 2012

Karina Nielsen

Abstract

The climate of the Earth is changing. A consequence of this is observed at the polar regions such as Greenland, where the ice sheet is melting with an increasing rate. The unloading of ice causes the Earth to respond elastically in terms of uplift and an outward horizontal deformation of the crust. This motion can be measured by permanent Global Positioning System (GPS) receivers. Hence, the rates of crustal displacement are an indirect measure of the occurring mass changes. Currently, 55 GPS sites are located around the margin of the Greenland ice sheet, continuously providing information about the state of the ice sheet. However, the Earth is also adjusting viscoelastically to variations in the late Pleistocene ice sheets i.e. glacial isostatic adjustment (GIA). Observed rates of crustal displacement therefor contain signals from both past and present ice mass variations. Hence, to interpret the observed rates a separation of theses signals are needed.

In this thesis, observed rates of crustal displacement are combined with modeled elastic rates to obtain constraints on the vertical displacement rate related to GIA. Observed rates are furthermore used to assess the local mass balance of Upernavik Isstrøm and Jakobshavn Isbræ.

GIA is an important correction in gravity-based mass balance estimates. It is therefore important to obtain reliable GIA predictions. Observed rates of crustal displacement can be used to constrain the GIA response, assuming that the present-day response, can be accurately modeled and removed. Over a period of a few decades, the GIA rate is assumed to be constant. Hence, changes in the observed rate results from the present-day changes. Here, mass change grids, derived from Ice, Cloud,and land Elevation Satellite (ICESat) data from three overlapping time spans are used to estimate the modeled elastic displacement rates at five permanent GPS sites in Greenland (THU1, SCOR, QAQ1, KULU, and KELY). These rates are compared to observed rates, which are estimated in the same time spans. An agreement in the temporal behavior between the modeled elastic and observed displacement rates indicates, that the modeled elastic displacements are well captured. Based on this analysis, the GIA rates are estimated to -1 ± 0.6 mm/yr at KELY, 2 ± 0.7 mm/yr at SCOR, and 0.5 ± 0.5 mm/yr at QAQ1. At the sites KULU and THU2 the elastic displacement rates could not be accurately estimated.

Gradients of crustal displacement rates near Upernavik Isstrøm and Jakobshavn Isbræ are modeled and compared to observed rates, to assess the mass balance of these glaciers. By considering displacement gradients, contributions from the mass loss of the rest of the ice sheet and GIA are reduced. Hence, gradients of crustal displacement roughly represent the local mass balance. Here, an agreement of 0.8 mm/yr or better is obtained. This indicates that the mass balances of these glaciers are well captured.

Dansk resumé

Jordens klima er under forandring. En konsekvens af dette kan ses i områderne ved polerne som fx. Grønland, hvor indlandsisen smelter med stigende hastighed. Når isen forsvinder medfører dette, at Jorden reagerer elastisk i form af landhævning og en udadgående horisontal deformation af skorpen. Disse bevægelser kan måles med permanente Global Positioning System (GPS) modtagere. Hastigheden af skorpebevægelserne er således et indirekte mål af de igangværende masseændringer. I øjeblikket er der 55 GPS stationer placeret hele vejen rundt om randen af indlandsisen, som kontinuerligt bidrager med information om indlandsisens tilstand. Jorden reagerer imidlertid også viskoelastisk på variationer i de sen Pleistocæne iskapper, dette kaldes glacial isostatisk justering (GIA). Observerede hastigheder af skorpens bevægelser består derfor af signaler fra både nutidige og fortidige masseændringer. For at kunne fortolke de observerede hastigheder, er det derfor nødvendigt at adskille disse signaler.

I denne afhandling kombineres observerede og modelerede hastigheder af de elastiske bevægelser, for at fastlægge de vertikale bevægelser relateret til GIA. De observerede hastigheder bruges yderligere til at validere massebalancen af Upernavik Isstrøm og Jakobshavn Isbræ, ved Grønlands vestkyst.

GIA er en vigtig korrektion ved tyngde basserede massebalance estimater. Det er derfor vigtigt at have pålidelige estimater af GIA. Observerede hastigheder af skorpebevægelsen kan bruges til at validere GIA signalet ved antagelse af at det nutidige signal kan bestemmes præcist, og derved kan det fjernes. Over en periode på nogle få årtier kan det antages, at GIA signalet er konstant. Ændringer i den observerede hastighed skyldes derfor de nutidige forandringer. Her, benyttes masseændringskort baseret på Ice, Cloud, and land Elevation Satellite (ICESat) data fra tre overlappende tidsrum til at modellere hastigheden af de elastiske skorpebevægelser ved fem permanente GPS stationer (THU1, SCOR, QAQ1, KULU, and KELY). Disse hastigheder sammenlignes med observerede hastigheder, der dækker det samme tidsrum. En overensstemmelse i den tidslige udvikling mellem hastighederne af den observerede og modellerede elastiske skorpebevægelse, indikerer at de elastiske skorpebevægelser er godt modellerede. Basseret på denne analyse, bestemmes GIA hastighederne til ca. -1 ± 0.6 mm/år ved KELY, 2 ± 0.7

mm/år ved SCOR og 0.5 ± 0.5 mm/år ved QAQ1. Ved stationerne KULU og THU2 kunne hastigheden af de elastiske skorpebevægelser ikke beregnes præcist nok.

Hastighedsgradienter af skorpebevægelsen nær Upernavik Isstrøm og Jakobshavn Isbræ modelleres og sammenlignes med observerede hastigheder for at vurdere massebalancen af disse gletchere. Ved at betragte gradienter af skorpebevægelsen, reduceres bidraget fra massetabet af den resterende del af indlandsisen og GIA. Gradienter af skorpebevægelsen repræsenterer således stort set den lokale massebalance. Her opnås en overensstemmelse på 0.8 mm/år eller bedre. Dette indikerer, at massebalancen for disse gletchere er godt bestemt.

List of abbreviations

ATM	Airborne Topographic Mapper
DEM	Digital Elevation model
GNET	Greenland GPS Network
GLAS	Geoscience Laser Altimeter System
GIA	Glacial Isostatic Adjustment
GMF	Global Mapping Function
GPS	Global Positioning System
GRACE	Gravity Recovery and Climate Experiment
GrIS	Greenland ice sheet
ICESat	Ice, Cloud, and land Elevation Satellite
InSAR	Interferometric Synthetic Aperture Radar
IGS	International GNSS Service
JPL	Jet Propulsion Laboratory
LDC	Loading Deformation Coefficient
LGM	Last Glacial Maximum
LIA	Little Ice Age
LIDAR	Light Detection And Ranging
LVIS	Laser Vegetation Imaging Sensor
NSIDC	National Snow and Ice Data Center
POLENET	Polar Earth Observing Network
PREM	Preliminary Reference Earth Model
REF	Reference Earth Model
RSL	Relative Sea Level
SELEN	Sea LevEL EquatioN solver
SLE	Sea Level Equation
SMB	Surface Mass Balance

Table of Contents

Papers

1

Introduction

The main topic for this PhD study is crustal displacements related to both past and present-day changes in the ice load of the Greenland ice sheet. This chapter is intended as an introduction, where the motivation and background for this study is outlined. Results obtained in previous studies are also presented here.

1.1 Motivation

Sea level rise caused by climate changes has become an urgent issue, particularly in the equatorial regions where the impact of sea level rise from the melting of polar ice sheets has the largest effect (Solomon, 2007). The global sea level rise from ice covered regions is estimated to 1.48 ± 0.26 mm/yr (Jacob et al., 2012). The Greenland ice sheet is one of the major contributors to sea level rise, where the ice tied up is equivalent to a sea level rise of 7.5 m (Alley et al., 2005). The ice sheet is currently loosing mass at a rate between 200 and 250 Gt/yr based on Ice, Cloud, and land Elevation Satellite (ICESat) and Gravity Recovery and Climate Experiment (GRACE) data between 2002 and 2009 (Velicogna, 2009; Sørensen et al., 2011; Schrama et al., 2011; Sasgen et al., 2012). This is equivalent to a global sea level rise of approximately 0.66 ± 0.08 mm/yr (Sørensen et al., 2011). The mass loss is caused by melting from the surface (Van Den Broeke et al., 2009) and dynamic thinning of outlet glacier (Pritchard et al., 2009), with the glaciers Helheim, Kangerdlugssuaq, and Jakobshavn Isbræ as the largest individual contributors (Howat et al., 2011). It is therefor important to monitor and measure the ongoing changes of the Greenland ice sheet with different techniques, to get a better understanding of the interaction between the climate and the ice sheet.

1.2 Monitoring changes of the Greenland ice sheet

The Greenland ice sheet has changed dramatically during the last decade. Some of these changes are indicated by an acceleration in the flow velocities of outlet glaciers (Joughin et al., 2010), which lead to increased discharge. A considerable retreat of the glaciers fronts is also observed (Joughin et al., 2010; McFadden et al., 2011; Bjørk et al., 2012). Furthermore, Studies have show that the total mass balance of the Greenland ice sheet has increased (Rignot and Kanagaratnam, 2006; Rignot et al., 2011). To monitor these changes various techniques are used. In the following some of the most important methods are presented.

1.2.1 Altimetry

Altimetry is a technique to determine the surface elevation. Measurements are conducted from satellites and airplanes with laser or radar instruments. In laser altimetry, the electromagnetic signal is reflected at the surface, while in radar altimetry the signal penetrates into the snow and ice column, and is reflected at different interfaces. By performing repeated measurements of the surface elevation over the ice sheet, surface elevation changes can be derived (Pritchard et al., 2009; Slobbe et al., 2009; Sørensen et al., 2011). By making appropriate assumptions of the snow and ice densities, an estimate of the mass change can be derived.

1.2.2 Gravity

Repeated measurements of the Earth's gravity field from the GRACE satellites, is a method to observe mass changes of the ice sheet (Velicogna and Wahr, 2005; Velicogna, 2009; Sørensen and Forsberg, 2010), since a change in the ice mass distribution causes a change in the gravity field. A part of the observed gravity change is not related to present-day ice mass changes, but results from redistribution of mantle material related to the process of GIA. To isolate the gravity changes related to the ongoing ice mass changes, corrections for glacial isostatic adjustment (GIA) must be applied.

1.2.3 Mass budget

In the mass budget method the various components of mass loss and gain are compared (Rignot and Kanagaratnam, 2006; Van Den Broeke et al., 2009; Rignot et al., 2011). Surface ablation and dynamic discharge at the ice margin contribute to the mass loss, while precipitation and sublimation contribute to mass gain of the ice sheet. The surface processes are quantified as the surface mass balance (SMB), which can be determined from regional atmospheric climate models and in situ measurements of precipitation and surface melt. Ice discharge can be derived from ice flow velocities, measured by interferometric synthetic aperture radar (InSAR) or Global Positioning System (GPS). The ice thickness can be measured by radio echo sounding.

1.2.4 Crustal displacements

A more indirect method of monitoring mass changes of the ice sheet, is by continuously measuring crustal displacements with GPS receivers, located on the bedrock near the ice margin (Khan et al., 2007, 2010b; Thomas et al., 2011; Bevis et al., 2012). When a load of ice is added or removed from the Earth's surface it responds elastically, which results in an instantaneous deformation of the crust. In other words the Earth acts as a weight, where the mass change is proportional to the rate of crustal displacement. Loading/unloading also causes displacement of mantle material beneath the load, which results in a delayed response of the surface. This signal is detectable after a few decades to thousands of years, depending on the size of the load and the viscosity in the mantle. This process is referred to as the Earth's viscoelastic response to past glacial changes called GIA. If the system (Earth + load) is left undisturbed it will reach a new isostatic equilibrium after a period of time (typically thousands of years).

1.3 Separating the elastic and viscoelastic signals of crustal displacements

A GPS receiver measures the combined crustal response; the elastic response; GIA; and possibly other factors such as tectonics and local hydrology. Hence, without any additional information it is not possible to separate these signals. In the following signals that are not related to ice mass variability are ignored.

As for the crustal displacements, the surface gravity also reflects changes related to both past and present-day ice mass variability. A change in the surface gravity related to the present ice mass variability contains an elastic response due to the elastic deformation of the Earth's crust and the direct attraction from the changing mass. The change in surface gravity related to GIA is composed of a response due to mass redistribution in the mantle and a response related to the corresponding height change of the surface. Wahr et al. (1995) estimated the GIA rates of gravity and vertical crustal displacement for a combination of different ice histories and mantle viscosity profiles, and found an empirical ratio of approximately -0.15 μGal/mm between the rates of viscoelastic gravity and crustal displacement. A similar ratio applies to the relation between the rates of elastic gravity and crustal displacement. De Linage et al. (2007) found a ratio of approximately -0.26

μGal/mm. This ratio also accounts for the direct attraction. Mémin et al. (2011) further showed that the elastic ratio also depends on the topography (the height difference between the load and observation point) and the ice elevation changes. Hence, with these empirical ratios and measurements of both absolute gravity and vertical crustal displacements, it is possible to uniquely separate the signals related to present day ice mass changes from those related to past glacial variations.

The first measurements of absolute gravity in Greenland was carried out at the permanent GPS sites KELY and KULU annually from 1995/1996 to 2000 (Wahr et al., 2001a). DTU-Space (Emil Nielsen) have since 2009 performed campaigns of absolute gravity with an A10 gravimeter in Greenland. At the moment there are 18 sites around the edge of Greenland, where measurements of both gravity and crustal displacements are performed, but the time series are still too short to give reliable results. The A10 measures with an uncertainty of up to 10 μGal. Hence, if considering the free-air gradient of -0.31 μGal/mm (Mémin et al., 2011), it requires a displacement of more than 30 mm to detect a gravity change, when the measurement error is taken in to account. Uplift rates at the edge of the Greenland ice sheet are in the range of a few mm to a few tens mm, hence in some places, it can take years to detect changes in the surface gravity.

Another method to separate the elastic and viscoelastic signals of crustal displacement, is to rely on the modeled results of one of the signals. This is the approach taken in this PhD study. An overview of how these signal can be modeled is given in Chapter 4 and 5.

1.4 Scientific objectives

In this thesis GPS rates of crustal displacements are used to constrain glacier mass balance, with spacial focus on Upernavik Istrøm and Jakobshavn Isbræ. The GPS rates will contain elastic displacements related to local ice mass changes from the glacier, elastic displacements due to ice mass changes from the rest of the ice sheet, and GIA. These contributions are modeled and compared to the observed rates.

Furthermore GPS rates are used to constrain GIA models of the Greenland ice sheet. At present day the elastic signal is up to an order of magnitude larger than the viscoelastic signal near the ice margin where ice is being discharged through outlet glaciers. Hence to constrain GIA it is important to have a highly accurate model for the elastic crustal displacements. Here, temporal changes in the observed and modeled elastic rates are used to validate the quality of the modeled elastic crustal displacements.

1.5 An overview of GPS measurements of crustal displacements

During the last two decades GPS measurements of crustal displacement related to ice mass variability have been used to gain information about e.g. Earth rheology, de-glaciation histories and the present day ice mass loss. In Greenland, Wahr et al. (2001a,b) used GPS measurements from three sites; THU1, KELY, and KULU. Based on five years of continuous data they concluded that the area around KELY was subsiding rather than uplifting as predicted by the ICE-3G GIA model (Tushingham and Peltier, 1991). The subsidence was explained by an advance of the western ice sheet margin in the area of KELY during the past 4000 years. The advance was further supported by geological and archaeological evidence found in the area. The advance of the southwestern ice margin was also suggested in an independent study by Dietrich et al. (2005). They established a campaign style GPS network consisting of 10 GPS sites, which were located along two lines between Ilulissat in the north and Paamiut in the south. Measurements were carried out during the summer between 1995 and 2002. By considering relative GPS rates they found subsidence of the bedrock adjacent to the ice margin except for the area around Ilulissat, where uplift was observed, due to the elastic response caused by ice discharge from the nearby Jakobshavn Isbræ. Khan et al. (2008) extended the work done by Wahr et al. (2001b) by analyzing longer time series from the previously used GPS sites and including data from the more recent established GPS sites Scoresbysund SCOB, SCOR, and QAQ1. To get an improved constraint on the GIA model estimates, they corrected the GPS rates for the Earth's elastic response to the ongoing ice mass changes. This was done by estimating the vertical crustal response due to ice mass loss from the largest outlet glaciers, Helheim, Kangerdlugssuaq, Jakobshavn plus contributions from an area representing the smaller glaciers in southeast Greenland. Later, Spada et al. (2012) used a 5 $\times$ 5 km resolution ICESat-derived mass balance model (Sørensen et al., 2011) to account for the elastic response due to the ongoing ice mass loss. Hence, by applying an elastic model of such detail, they obtained an improved constraint on the GIA signal at the GPS locations used in Khan et al. (2008). In their work, they further demonstrated that even smaller glaciers in the vicinity of a GPS site can make a significant contribution to the elastic displacement and hence cannot be ignored. (Bevis et al., 2012) analyzed GPS data from all the Greenland GPS Network (GNET) sites, and found uplift rates of up to 30.5 mm/yr at KUAQ at the southeast coast of Greenland. They further showed a considerable uplift anomaly i 2010, even at sites located far from the ice margin, related to the wide-spread melting event in 2010 (Tedesco et al., 2011).

GPS measurements have also been used in more local studies in Greenland to

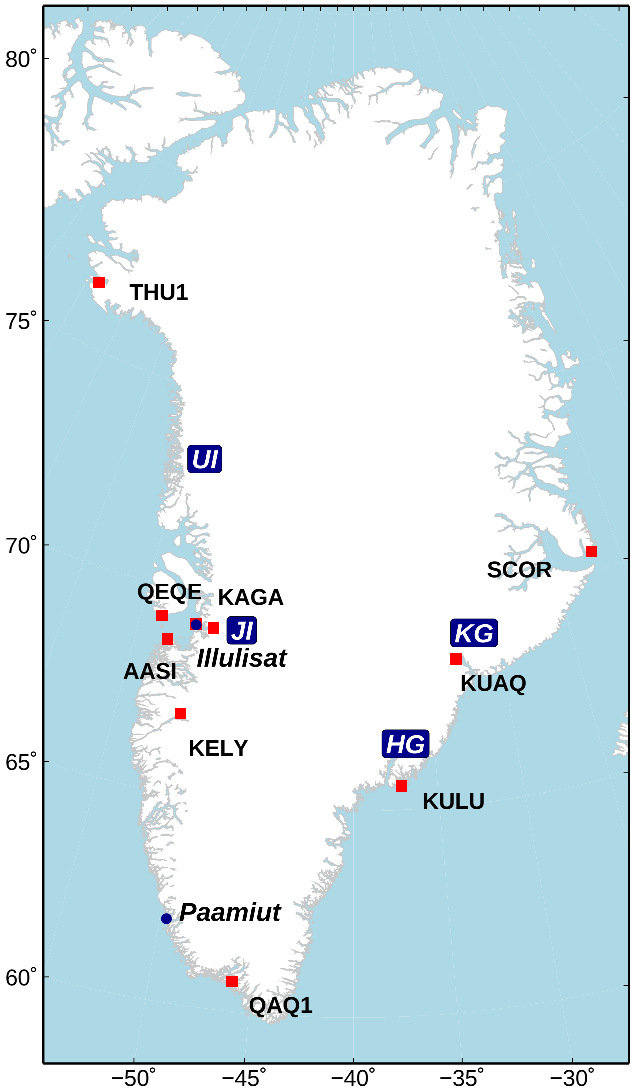

Figure 1.1: Site map of Greenland. Red squares indicate the location of selected permanent GPS sites, the location of outlet glaciers (rectangles) and cities (dots) mentioned in the text are also indicated.

obtain constraints on the recent glacial ice mass loss. Khan et al. (2007) observed large crustal uplift rates at KULU located ∼90 km from the calving front of Helheim glacier. They demonstrated that this rates could only be explained by the ongoing ice mass loss of Helheim, Kangerdlugssuaq and surface melting of the along the southeast Greenlandic coast. In a study around Jakobshavn Isbræ Khan et al. (2010b) analyzed GPS measurements from four sites located between 5 and 150 km from the front. They found, that the GPS rates dropped considerably at the sites further away from the front, suggesting that the observed uplift rates mainly were related to the present day ice mass loss from Jakobshavn Isbræ.

In other ice covered regions several studies have used GPS measurement in a similar way. Larsen et al. (2005) and Dietrich et al. (2010) observed high uplift rates of 32 mm/yr in southeast Alaska and 39 mm/yr in Patagonia, respectively. These high rates of vertical uplift was mainly related to the Earth's viscoelastic response due to ice unloading since the Little Ice Age (LIA) and the elastic response due to the present day melting. Sato et al. (2006) used GPS measurement in Svalbard and concluded that the observed rates could only be explained by a combination of the present day melting and the viscoelastic response to past glacial variability. In Antarctica Thomas et al. (2011) found, by analyzing data from 52 GPS stations, that GIA models often overestimates the GIA signal.

1.6 Structure of the thesis

This thesis is based on four papers I-IV, these are briefly summarized in Chapter 2, and an introduction, that presents the adequate background regarding the data and methods, which are used in the papers. Chapter 3 presents the different data types, that are used in this thesis. The crustal displacements caused by the present day ice mass variability is investigated in Chapter 4, where the area of Jakobshavn Isbræ is used as a case study. In Chapter 5 the principle of GIA is presented, and in Chapter 6 it is shown how the combination of modeled and observed rates of crustal displacement can be used to constrain both the GIA signal and the mass balance of local glaciers. The overall discussion, conclusion, and suggestions for future work is presented in Chapter 7.

2

Scientific papers

Paper 1

Sørensen, L. S., Simonsen, S. B., Nielsen, K., Lucas-Picher, P., Spada, G., Adalgeirsdottir, G., Forsberg, R. and Hvidberg, C. S., 2010. *Mass balance of the Greenland ice sheet (2003–2008) from ICESat data - the impact of interpolation, sampling and firn density*, The Cryosphere, 5, 173-186.

The mass balance of the Greenland ice sheet is derived from ICESat data (2003-2008), where firn compaction and density modeling are taken into account. Elevation changes are derived using three different methods. These are interpolated onto a 5 × 5 km grid and corrected for signals, which are not related to a mass changes such as; firn compaction, inter-campaign elevation bias, vertical bedrock motion, caused by present and past ice mass variability. The corrected and gridded elevation changes are converted to mass changes by applying a surface density model. The mass loss estimates are in the range of 191 ± 23 Gt/yr to 240 ± 28 Gt/yr, depending on the method.

Paper 2

Nielsen, K., Sørensen, L. S., Khan, S. A., Spada, G., Simonsen, S. B., and Forsberg, R., 2012. *Towards constraining glacial isostatic adjustment in Greenland using ICESat and GPS observations*, accepted for publication in the International Association of Geodesy Symposia (IUGG Melbourne, 2011).

Temporal variations in the modeled and observed uplift rates are compared. The modeled elastic rates are based on ICESat-derived mass change grids in three overlapping time spans 2004-2007, 2005-2008, and 2006-2009. The modeled elastic rates are compared to observed rates at the permanent GPS sites THU1, SCOR, QAQ1, KULU, and KELY. An agreement in the temporal behavior between the modeled and observed rates at the sites SCOR, QAQ1, and KELY suggests, that the elastic displacement rates are well captured at these sites. Hence, these site are useful for constraining GIA.

Paper 3

Nielsen, K., Khan, S. A., Korsgaard, N. J., Kjær, K. H, Wahr, J., Bevis, M., Stearns, L. A, and Timm, L. H., 2012. *Crustal uplift due to ice mass variability on Upernavik Isstrøm, west Greenland*, accepted for publication in Earth and Planetary Science Letters.

This paper investigates recent changes on the Upernavik Isstrøm. Based on elevation changes between a SPOT 5 Digital Elevetion Model (DEM) from 2008 and NASA's Airborne Topographic Mapper (ATM) laser altimetry data a the mass loss is estimated to be -6.7 ± 4.2 Gt/yr. To assess this mass loss estimate the observed and modeled rates of vertical crustal displacements are compared at two GPS sites, SRMP and UPVK, which are located ∼2 and ∼65 km from the front of Upernavik Isstrøm. By analyzing along-track elevation changes from various sources in the period 2005-2011, a large variation, of -15 to -40 m/yr, in the thinning pattern at the front of Upernavik Isstrøm is observed.

Paper 4

Nielsen, K., Khan, S. A., Spada, G., Wahr, J., Bevis, M., Liu, L., and van Dam, T., 2012. *Vertical and horizontal surface displacements near Jakobshavn Isbræ driven by melt-induced and dynamic ice loss*, submitted to Journal of Geophysical Research.

In this paper both horizontal and vertical crustal displacements are analyzed at four GPS sites located between ∼5 and ∼150 km from the front of Jakobshavn Isbræ. To account for plate motion in the horizontal displacements, relative displacements are considered. The horizontal motion point towards west-northwest, suggesting that the majority of the mass loss is south of the GPS sites. Furthermore, uplift anomalies related to the 2010 melting event are estimated. Relative large anomalies (5-6 mm) are found at the distant sites, suggesting that the anomalies are caused by a wide-spread melting. At the site KAGA (near the front) the anomaly is 8.8 mm, which is quite low considering its location. This can be explained by a considerable decrease in the dynamic thinning pattern near the front of Jakobshavn Isbræ.

3

Data

Crustal displacements caused by ice mass variability, can be observed directly by continuous GPS measurements, or predicted by modeling the corresponding response. The latter method requires information regarding changes in the ice load, which can be obtained from measurement of the ice surface elevation. In this Chapter, the primary data types used in this thesis are presented; GPS measurements of crustal displacements and surface elevations.

3.1 GPS

Currently, there are 55 permanent GPS stations located around the edge of the Greenland ice sheet, which continuously provide measurements of 3D surface positions. The earliest GPS stations were installed in the mid 1990s. The stations KELY and KULU were installed by the University of Colorado in cooperation with UNAVCO in 1995 and 1996, and the stations THU1,THU2/THU3, SCOB, SCOR, QAQ1 were installed by the Danish National survey and Cadastre in 1995, 1998, 1997, 2004, and 2001, respectively. It should be noted that THU2 and THU3 used the same GPS antenna but different receivers, while THU1 is a different station located about 963.31 meters from THU2. These stations are part of the International GNSS Service (IGS) (marked with white triangles in Fig. 3.1).

The time series of vertical crustal displacement for these early stations now contain up to 17 years of data, which enables the study of changes in trends. Figure 3.2 shows an example of a GPS site, here KULU, and Figure 3.3 displays the time series of the measured vertical bedrock motion. The time series clearly shows a seasonal signal related to the annual cycle of mass gain and loss. When the entire observation period is considered an evident change in the underling trend is also seen, resulting from increased mass loss in southeast Greenland Khan et al. (2007)

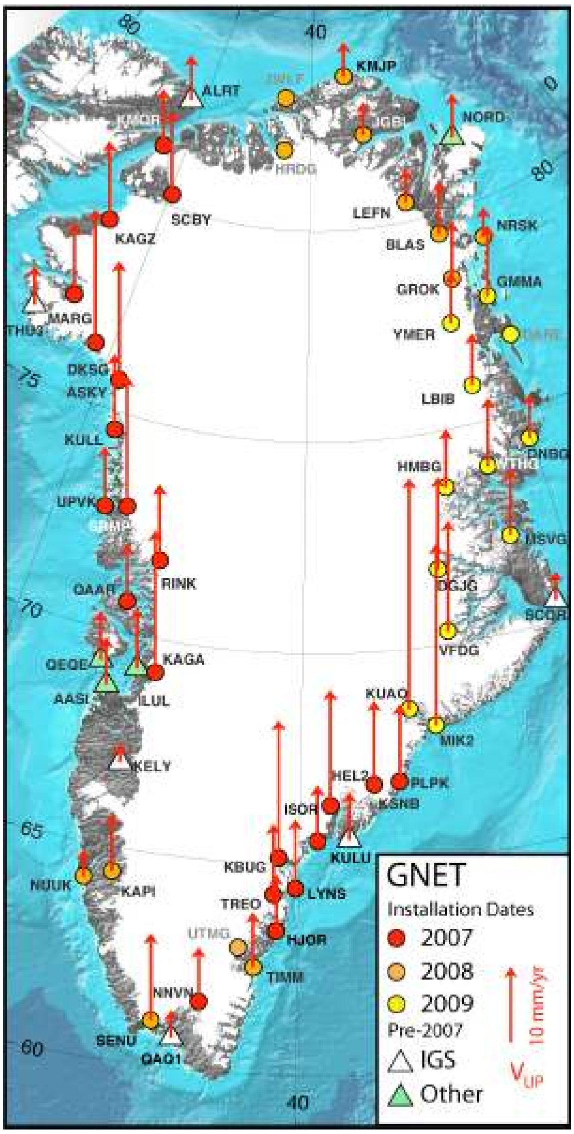

Figure 3.1: Permanent GPS stations in Greenland, and their associated vertical displacement rates estimated by Bevis et al. (2012).

3.1.1 The Greenland GPS network

GNET) is a collection of 45 continuous GPS stations located on bedrock around the margin of the Greenland ice sheet. The stations were installed during summer campaigns in 2007, 2008, and 2009. Many of the stations are located in pairs, with one station located near the ice margin, and the other located close to the coast. This setup enables the study of crustal displacement gradients. GNET is a contribution to the IPY Polar Earth Observing Network (POLENET), with partners from US, Denmark and Luxembourg.

The main purpose of the network is to monitor the present-day ice mass changes

Figure 3.2: GPS station at Kulusuk. The image is from van Dam et al., EOS, 81, pp. 426-427, 2000.

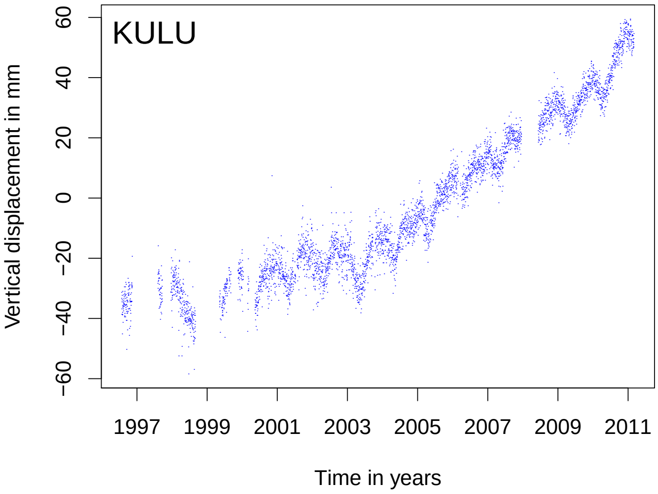

Figure 3.3: Time series of vertical displacements for the site KULU, where each dot represents a daily solution.

of the Greenland ice sheet. The network will also provide improved constraints on GIA, which is an important correction in gravity based mass balance estimates from GRACE data. The GRACE satellites measure the total gravity change resulting from e.g. present day ice mass changes at the surface, and mass redistribution in the mantle related to GIA.

Fig. 3.1 shows GNET vertical displacement rates (Bevis et al., 2012) at most of the permanent stations in Greenland. Their solutions show, that the entire ice margin is uplifting. The largest rates are observed near the Kangerlussuaq glacier in southeast Greenland and along the northwest coasts. These are all areas with considerable mass loss, hence, the observed rates primarily reflects the present-day melting.

3.1.2 Processing

The Processing of the GPS data used in this thesis is done by Shfaqat Abbas Khan, according to Khan et al. (2010b) using the GIPSY OASIS 6.1.2 software package (Zumberge et al., 1997), developed at the Jet Propulsion Laboratory (JPL). GPS rates from the sites used in this thesis are listed in Table 3.1.

The site coordinates are estimated using the orbit products, released in 2010 by the IGS (repro1 products). These include satellite orbits, satellite clock parameters, and Earth orientation parameters. The new orbit products take the satellite antenna phase center offsets into account. Receiver clock parameters are modeled, and the atmospheric delay parameters are modeled using the Global Mapping Function (GMF) (Böhm et al., 2006). Corrections are applied to remove the solid Earth tide and ocean tidal loading. The amplitudes and phases of the main ocean tidal loading terms are calculated with the Automatic Loading Provider (`http://www.oso.chalmers.se/~loading`, Scherneck and Bos (2002)), on the basis of the FES2004 ocean tide model, including correction for center of mass motion of the Earth due to the ocean tides. The site coordinates are computed in the non-fiducial frame and transformed to the ITRF2005 frame, (Altamimi et al., 2007). The secular trends and their uncertainty are esimated as described by Khan et al. (2010b).

The site coordinates are estimated based on data from one day, which results in a time series of displacements (see e.g. Fig. 3.3). Rates are estimates by fitting semi-annual, annual, and linear terms to the displacement time series. In this thesis, both absolute and relative rates are considered. Relative rates represent the motion of one site relative to another.

3.2 Laser altimetry

Satellite and airborne altimetry are methods to obtain surface elevations over ice covered regions. In this PhD thesis surface elevations from NASA's ICESat and IceBridge missions are used to estimate volume changes of the Greenland ice sheet and subsequent modeling of crustal displacements.

An illustration of the measurement principle in laser satellite altimetry is shown in Fig. 3.4, here for the ICESat satellite. The laser on-board the satellite emits a short laser pulse, which is reflected at the Earth's surface. The altitude a of the satellite is then determined by $a = c\frac{\Delta t}{2}$, where Δt is the two-way traveltime, and c is the speed of light. GPS receivers on-board the satellite determine its spatial position, from which the altitude a of the satellite above a reference ellipsoid, can be derived. Hence, from the ellipsoidal height h, and the altitude a, the surface elevation is derived.

3.2.1 ICESat

In the following a short description of the ICESat mission is presented, and a brief overview of the processing steps regarding the estimation of the Greenland mass balance is described.

The NASA satellite ICESat, operated between 2003 and 2009 in a near polar orbit at an altitude of 600 km (NASA-ICESat, 2012). On-board the satellite the

Table 3.1: Absolute and relative displacement rates in mm/yr at the GPS sites used in this PhD project. V_u is the absolute vertical rate, RV_u, RV_e, and RV_n represent the vertical, east, and north components of the relative displacement rates.

Station	Time span	V_u	RV_u	RV_e	RV_n
KULU	Jan 2004-Dec 2007	9.4 ± 0.6	-	-	-
KULU	Jan 2005-Dec 2008	8.9 ± 0.7	-	-	-
KULU	Jan 2006-Dec 2009	7.6 ± 0.6	-	-	-
KELY	Jan 2004-Dec 2007	1.5 ± 0.7	-	-	-
KELY	Jan 2005-Dec 2008	3.4 ± 0.6	-	-	-
KELY	Jan 2006-Dec 2009	3.0 ± 0.6	-	-	-
THU2	Jan 2004-Dec 2007	5.6 ± 0.7	-	-	-
THU2	Jan 2005-Dec 2008	8.1 ± 0.8	-	-	-
THU2	Jan 2006-Dec 2009	8.9 ± 0.6	-	-	-
SCOR	Jan 2004-Dec 2007	3.9 ± 0.7	-	-	-
SCOR	Jan 2005-Dec 2008	4.0 ± 0.7	-	-	-
SCOR	Jan 2006-Dec 2009	3.1 ± 0.6	-	-	-
QAQ1	Jan 2004-Dec 2007	3.3 ± 0.5	-	-	-
QAQ1	Jan 2005-Dec 2008	4.0 ± 0.5	-	-	-
QAQ1	Jan 2006-Dec 2009	3.2 ± 0.5	-	-	-
UPVK	Jul 2007-Apr 2010	7.6 ± 0.6	-	-	-
SRMP	Jul 2007-Apr 2010	16.2 ± 0.6	8.6 ± 0.8[a]	-	-
KAGA	May 2006-Jan 2011	18.6 ± 0.7[b]	12.8 ± 0.6[c]	-1.8 ± 0.3	0.9 ± 0.3
ILUL	Jan 2006-Jan 2011	7.1 ± 0.5[b]	1.9 ± 0.4[c]	-0.8 ± 0.2	0.7 ± 0.2
QEQE	Jan 2006-Jan 2011	6.1 ± 0.5[b]	-0.1 ± 0.4[c]	-0.4 ± 0.2	0.4 ± 0.2
AASI	Jan 2006-Jan 2011	5.9 ± 0.5[b]	-	-	-

[a] Rate relative to UPVK.

[b] Rates based on data until Oct, 2009.

[c] Rates relative to AASI.

Geoscience Laser Altimeter System (GLAS) instrument measured the surface elevation along-track with a resolution of 170 m (NASA-GLAS, 2012). The satellite operated in a 91-day repeat cycle, which has enabled the detections of surface elevation changes over the ice sheets. Due to problems with the lasers on-board, the measurements were only performed 3 times per year approximately 33 days at a time.

Sørensen et al. (2011) used the GLAS/ICESat L2 Antarctic and Greenland Ice Sheet Altimetry (GLA12) data release 31, to estimate the mass balance of the

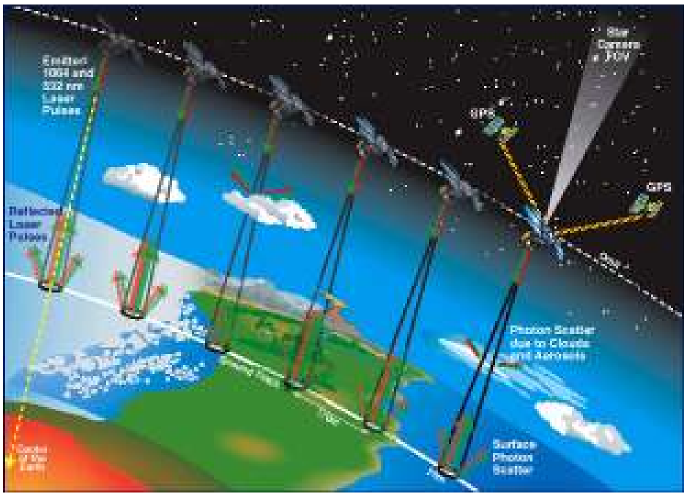

Figure 3.4: Illustration of the measurement principle of the GLAS instrument on-board ICESat `http://www.nasa.gov/vision/earth/lookingatearth/icesat_billion.html`.

Greenland ice sheet. This data set contains surface elevations over ice sheets and is available at the National Snow and Ice Data Center (NSIDC) (NSIDC-ICESat, 2012). The process of deriving a mass balance model of the Greenland ice sheet from ICESat surface elevations is described in detail by Sørensen et al. (2011) and Sørensen (2011). Here the concepts of the processing done in Sørensen et al. (2011), are briefly summarized in bullets.

- Data culling serve to reduce systematic errors and remove less reliable surface elevation estimates from the data set.
- Elevation changes are estimated in 500 m segments along tracks by least squares fitting.
- Volume changes are derived by spatial interpolation of the elevation changes onto a 5 × 5 km grid using ordinary kriging.
- Elevation changes which are not related to actual mass changes are removed. This includes firn compaction, drift of the satellite between campaigns (intercampaign bias), and bedrock elevation related to past and present day ice mass variability.
- Mass changes are obtain by proper modeling of the surface densities.

Figure 3.5 displays three mass balance estimates in water equivalents of the Greenland ice sheet based on elevation changes in three overlapping time spans 2004-2007, 2005-2008, and 2006-2009. These have been estimated by using the method

(M3) described in Sørensen et al. (2011). The mass balance models are characterised by widespread mass loss around the edge of the GrIS, with the most distinct signals at the largest outlet glaciers Helheim, Kangerdlussuaq, and Jakobshavn. A weak signal of mass gain is generally observed in the interior of the ice sheet, and more distinct signals along the northeast coast. When considering the temporal trend over the entire observation period, a pattern of mass loss change is observed. Between 2004-2007 (Figure 3.5a) the mass loss signal is most pronounced at the southeast coast, and later (Figure 3.5b and c) an increase in mass loss is observed along the west and north coast of Greenland along with a weakening of the signal at the southeast coast.

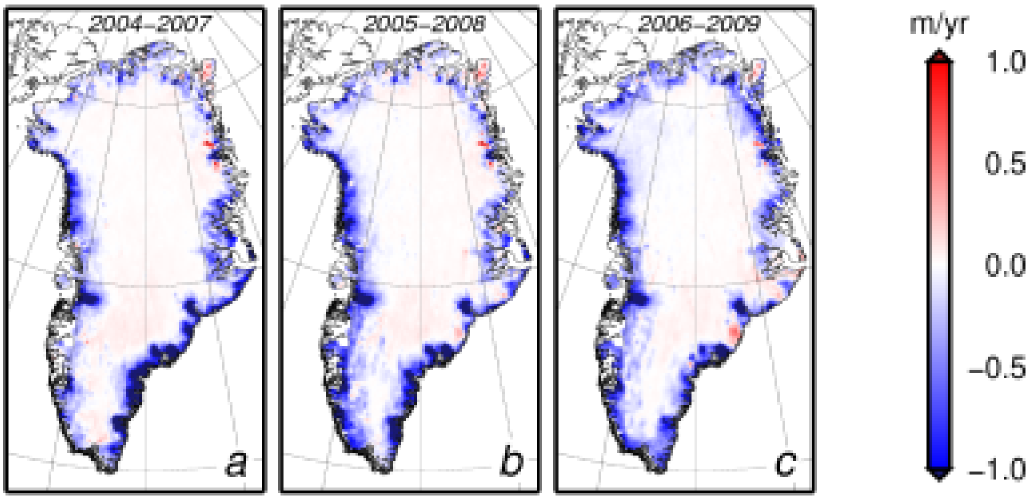

Figure 3.5: Mass balance estimates of the Greenland ice sheet given in water equivalents. The estimates are derived from ICESat data between (a) 2004-2007, (b) 2005-2008, and (c) 2006-2009.

3.2.2 Pre-IceBridge and IceBridge

IceBridge, initiated in 2009, is a program that performs airborne remote sensing surveys over the Earth's polar ice sheets. It is a six year NASA program intended to bridge the gap in elevation measurements between the ICESat-1 mission and the ICESat-2 mission, which is planned for early 2016. The surveys are performed twice a year, in Greenland during March through May and in Antarctica during October through November, with special focus on areas with rapid mass changes. The elevation measurements are performed with NASA ATM, which is a scanning Light Detection And Ranging (LIDAR). Besides elevation measurements, the IceBridge mission also perform measurements of e.g. bed topography, grounding line position, and ice and snow thickness (NASA-IceBridge, 2012).

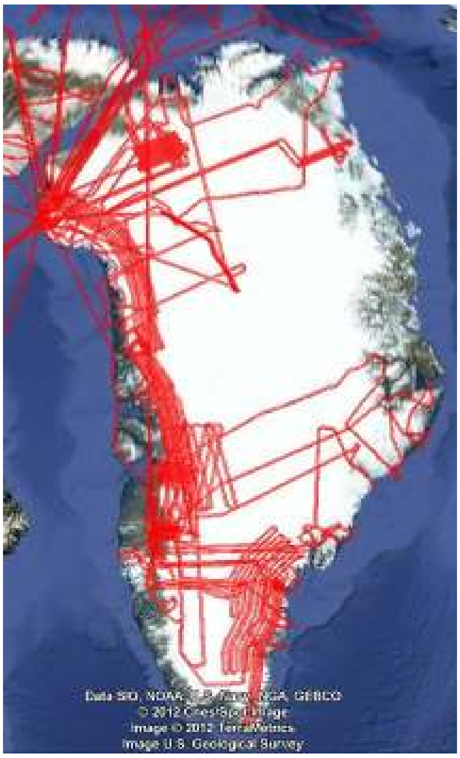

Figure 3.6: Flight trajectories from the ATM 2011 Greenland campaign.

The IceBridge products are available at the NSIDC (NSIDC-IceBridge, 2012). In this PhD project the IceBridge data product IceBridge ATM L2 Icessn Elevation, Slope, and Roughness (ILATM2) (Krabill, 2011) and the pre-IceBridge product Pre-IceBridge ATM Level-2 Icessn Elevation, Slope, and Roughness (BLATM2) (Krabill and Thomas., 2010) are used. These data products contain geo-located smoothed elevation measurements at a spatial resolution of approximately 50 m. The pre-IceBridge elevation measurements cover the period 1993 through 2008. Fig. 3.6 shows an example of an IceBridge ATM campaign, here from 2011. Measurements are primarily collected over areas with a considerable mass loss e.g. along the southeast and western margin of the Greenland ice sheet. Hence, these data sets are particular useful for studying ice elevation changes on a glacier level.

Surface elevation changes from these data sets can be obtained in areas with repeated surveys. To avoids errors related to topography, only points separated by less than 30 m are considered. In areas with sufficient spatial data coverage, a volume loss estimate can be obtained by interpolation of the along-track elevation changes. In this thesis, ordinary local neighbourhood kriging is used as the interpolation method, where information regarding the correlation length is obtained from the empirical variogram. Jakobshavn Isbræ, one of Greenland's largest outlet glaciers, has been surveyed repeatedly by ATM instrument since 1997. Fig.

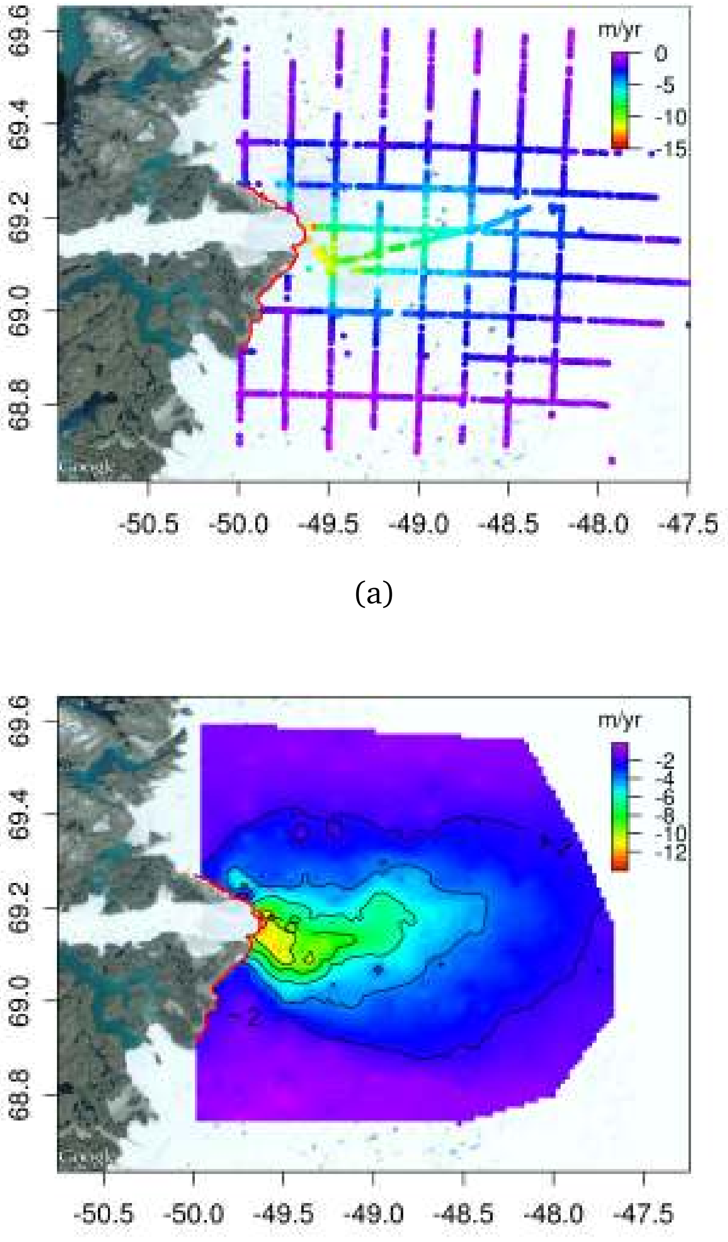

(a)

(b)

Figure 3.7: (a) Along-track linear elevation changes for the area of Jakobshavn Isbræ, based on ATM data from 2006, 2009, 2010, and 2011 (Nielsen et al., 2012c). (b) Elevation changes interpolated onto a 1 × 1 km grid

3.7a shows linear along-track elevation changes for the area of Jakobshavn Isbræ during the time spans 2006-2011, and Fig. 3.7b shows the interpolated elevation changes. Jakobshavn Isbræ is thinning over a large area, where rates of a few m/yr are observed fare inland. At the front thinning rates of up to -15 m/yr are observed. Several studies have used ATM measurements to study Jakobshavn Isbræ e.g. Joughin et al. (2008); Khan et al. (2010b).

4

Elastic displacements due to present day ice mass variability

When a load is placed or removed from the surface of the Earth it causes an instantaneous elastic deformation of the Earth's crust, which depends on the mass of the load and the material properties of the Earth. In relation to glaciers and ice sheets the present day mass changes e.g. dynamic thinning, discharge, surface melting and snowfall are examples of such loads. The elastic displacements, in this thesis, have been estimated using Farrell's Green's functions (Farrell, 1972) or a modified version of a Fortran program by Giorgio Spada (Personal, communication 2011).

4.1 The elastic response to a surface disc load

The Vertical and horizontal responses to an axial symmetric load as a function of the colatitude α are given by (see e.g. Spada (2003))

$$U(\alpha) = \frac{3}{\rho_e} \sum_{n=0}^{n_{max}} h_n \frac{\sigma_n}{2n+1} P_n(\cos\alpha), \tag{4.1}$$

$$V(\alpha) = \frac{3}{\rho_e} \sum_{n=0}^{n_{max}} l_n \frac{\sigma_n}{2n+1} \frac{\partial P_n(\cos\alpha)}{\partial \alpha}, \tag{4.2}$$

where ρ_e is the average density of the Earth, P_n is the Legendre polynomial, n is the harmonic degree, h_n and l_n are the vertical and horizontal Loading Deformation Coefficients (LDCs), sometimes called love numbers. For an elementary disc load the nth harmonic component of the load σ_n is given by (see e.g. Spada et al. (2011))

$$\sigma_n = \frac{\rho_i \, \Delta H}{2} \begin{cases} 1 - \cos\beta & \text{if } n = 0 \\ [-P_{n+1}(\cos\beta) + P_{n-1}(\cos\beta)] & \text{if } n \geq 1 \end{cases} \tag{4.3}$$

Where β is the radius of the disc load. ρ_i is the density of ice, and ΔH is the thickness change of the ice load.

4.2 Load deformation coefficients (LDCs)

The vertical and horizontal LDCs h_n and l_n enter into Eq. (4.1) and (4.2). These LDCs, plus a third LDC k_n related to the gravity potential, are found by solving the elastic equations of motion in spherical coordinates for a self gravitating spherical Earth subjected to a surface load. The equations of motion for such an Earth is given by (see e.g. Farrell (1972))

$$\begin{gathered}\nabla \cdot \tau - \nabla(\rho g \mathbf{s} \cdot \mathbf{e_r}) - \rho \nabla \varphi + g \nabla \cdot (\rho \mathbf{s}) \mathbf{e_r} = 0 \\ \nabla^2 \varphi = -4\pi G \nabla \cdot (\rho \mathbf{s}).\end{gathered} \tag{4.4}$$

Here τ is the stress tensor, ρ is the unperturbed density, g is the gravitational acceleration, φ is the perturbation in the gravitational potential, $\mathbf{s}$ is the displacement vector, and G is the gravitational constant. The system of equations in (4.4) form a coupled set of four second order differential equations. If it is assumed that; (1) the Earth is spherical symmetric hence, its material properties only depend on the radial distance r from the center of the Earth and; (2) the applied surface load is axial symmetric, then the solution becomes independent of the longitude and (4.4) is reduced to a coupled set of three differential equations. Hence, $\mathbf{S}$ and φ can be expressed in term of Legendre polynomials (see e.g. Farrell (1972)).

$$\begin{aligned}\mathbf{s} &= \sum_{n=0}^{\infty} \left(U_n(r) P_n(\cos\theta) \mathbf{e_r} + V_n(r) \frac{\partial P_n(\cos\theta)}{\partial \theta} \mathbf{e}_\theta \right) \\ \varphi &= \sum_{n=0}^{\infty} \Phi_n(r) P_n(\cos\theta).\end{aligned} \tag{4.5}$$

Here U_n, V_n, and Φ_n are the transformed variables and n is the harmonic degree. This expansion reduces (4.4) to a system of six first order linear differential equation, which can be solved numerically with appropriate boundary conditions. A detailed description is found in e.g Longman (1962) and Farrell (1972). The transformed variable are related to the LDCs h_n, l_n, and k_n through the following relation (Farrell, 1972)

$$\begin{pmatrix} U_n(r) \\ V_n(r) \\ \Phi_{1,n}(r) \end{pmatrix} = \Phi_{2,n} \begin{pmatrix} \frac{h_n(r)}{g} \\ \frac{l_n(r)}{g} \\ k_n(r) \end{pmatrix}, \tag{4.6}$$

where $\Phi_{2,n}$ is the transformed potential of the applied force field and $\Phi_{1,n}$ is transformed potential of the Earth's distorted density field. The LDCs depends on the boundary conditions and the material properties of the Earth. Hence, for each solution to Eq. 4.4 a unique set of LDCs exist.

Examples of the LDCs h_n and l_n up to harmonic degree $n = 1024$ are shown in Fig. 4.1a. The solid curves represent LDCs related to an Earth model with Preliminary Reference Earth Model (PREM) (Dziewonski and Anderson, 1981) structure and these are acquired from the Atmospheric Pressure Loading service. The LDCs, represented by the dashed curves, are based on the Earth model JAK (see Section 4.3.2), and are estimated by Pascal Gegout (personal communication, October 2011).

Fig. 4.1b shows the vertical and horizontal responses to a single disc load with a radius of $\beta = 500$ m and a thickness variation of $\Delta H = -1$ m. These are estimated by Eq. (4.1) and (4.2) with $n_{max} = 10^5$. After the harmonic degree $n = 1024$, it is assumed that the asymptotic limit is reached (see Farrell (1972)) The vertical response has its maximum amplitude right beneath the center of the load. The signal decreases rapidly, and at 4 disc radii it is reduced to approximately 10 %. The horizontal displacement is zero right beneath the center of the load, due to symmetry, and has its maximum amplitude at the periphery of the load.

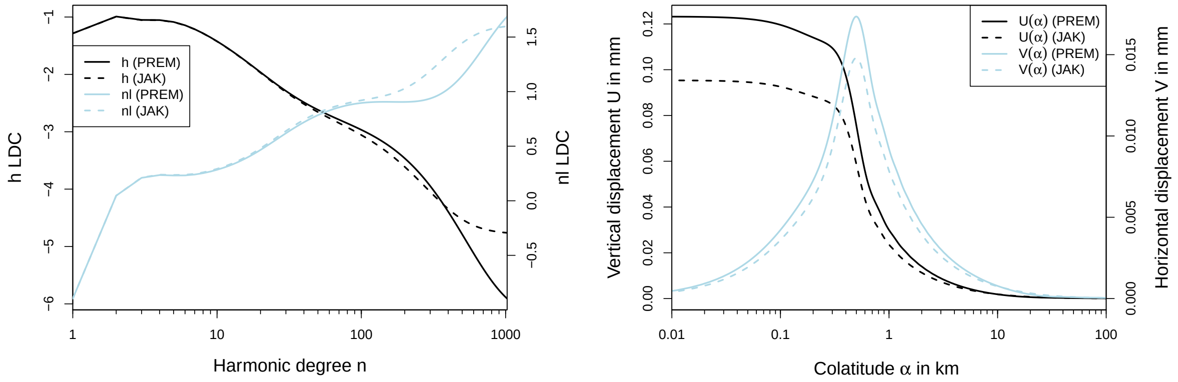

(a) (b)

Figure 4.1: (a) Vertical h (black curves) and horizontal nl (light blue curves) LDCs up to harmonic degrees 1024, where the solid curve is related to the Earth model PREM and the dashed curve is related to the Earth model JAK. (b) Vertical (black curves) and horizontal (light blue curves) displacements from a single disc load with a radius of $\beta = 500$ m and a thickness variation of $\Delta H = -1$ m, where the solid curve is related to the Earth model PREM and the dashed curve is related to the Earth model JAK.

4.3 Modeling of elastic displacements due to present-day ice mass variability.

This Section is intended as a description of how to model the elastic displacements related to the ongoing ice mass changes. As an example, the area of Jakobshavn Isbræ is used. The vertical and horizontal displacements around Jakobshavn are studied in Nielsen et al. (2012c). Here, this work is extended and other subjects related to elastic displacement modeling are discussed.

4.3.1 The elastic response due to a complex load distribution

The equations (4.1) and (4.2) represent the vertical and horizontal responses to a single disc load, given that σ_n is represented by eq. (4.5). To estimate the response from a complex load distribution such as Jakobshavn Isbræ, a convolution is performed between Eq. (4.1) and (4.2) and an ice elevation change grid, with a resolution of β. Hence, at each observation point the displacement is a sum of all the individual responses, defined by the distance to the load and the height of the discs. A linear elevation change grid for the area of Jakobshavn Isbræ, based on ATM data from 2006, 2009, 2010, and 2011, are displayed in Fig. 3.7b. The corresponding displacement fields are shown in Fig. 4.2. The vertical displacement field has a distribution similar to the elevation changes. As for the single disc load, this example illustrates how rapid the signal is reduced as a function of the distance from the front of Jakobshavn Isbræ. The horizontal field, as expected, has a minimum right beneath the load and a maximum at the periphery of the load (see Fig. 4.1b). The horizontal motion points away from areas with mass loss and is directed toward areas with mass gain. Hence, the horizontal motion gives an indication of the origin of the load.

4.3.2 Impact on the elastic response due to the Earth model

Deformation of the Earth's crust depends on the material properties of the Earth. To understand the influence of the Earth model in relation to the elastic response, the vertical displacements related to ice mass loss at Jakobshavn Isbræ (see Fig. 3.7b) are estimated based on two different Earth models, PREM and CRUST2.0 (Bassin et al., 2000) type crust model for the area of Jakobshavn Isbræ overlying a Reference Earth Model (REF) (Kustowski et al., 2008) Earth model. Here after the latter Earth model is referred to as JAK.

CRUST2.0 is a 2×2 degree global crustal model, where each cell is composed of a 7 layer profile consisting of: ice, water, soft sediments, hard sediments, upper

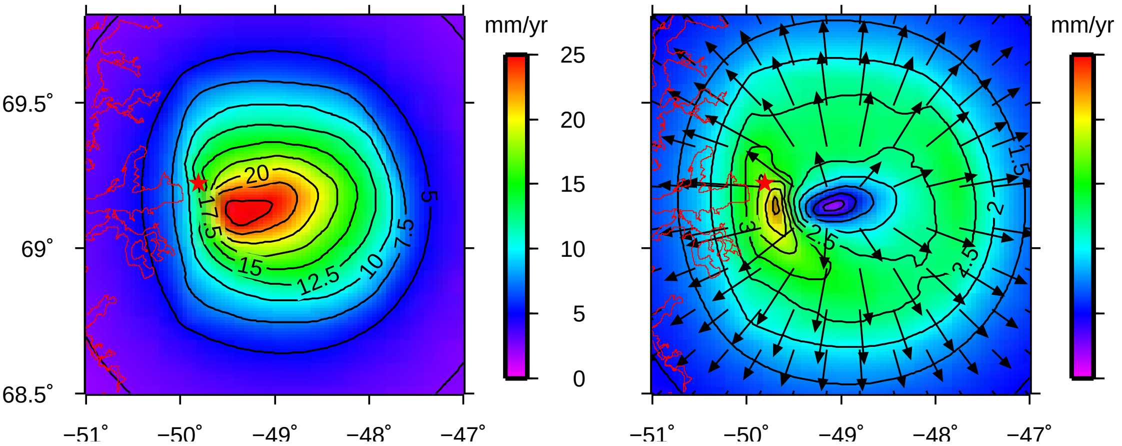

Figure 4.2: The vertical (left) and horizontal (right) displacement field related to the linear thinning of Jakobshavn Isbræ between 2006 and 2011 (see Fig. 3.7b). The red star indicates the positions of the GPS site KAGA.

crust, middle crust, and lower crust. Fig. 4.3 displays the crustal thickness based on the CRUST2.0 model. In Greenland the crustal thickness range between 30 and 40 km, which is higher than the PREM global average crustal thickness of 25 km. The material characteristics of CRUST2.0 for the area of Jakobshavn Isbræ and the

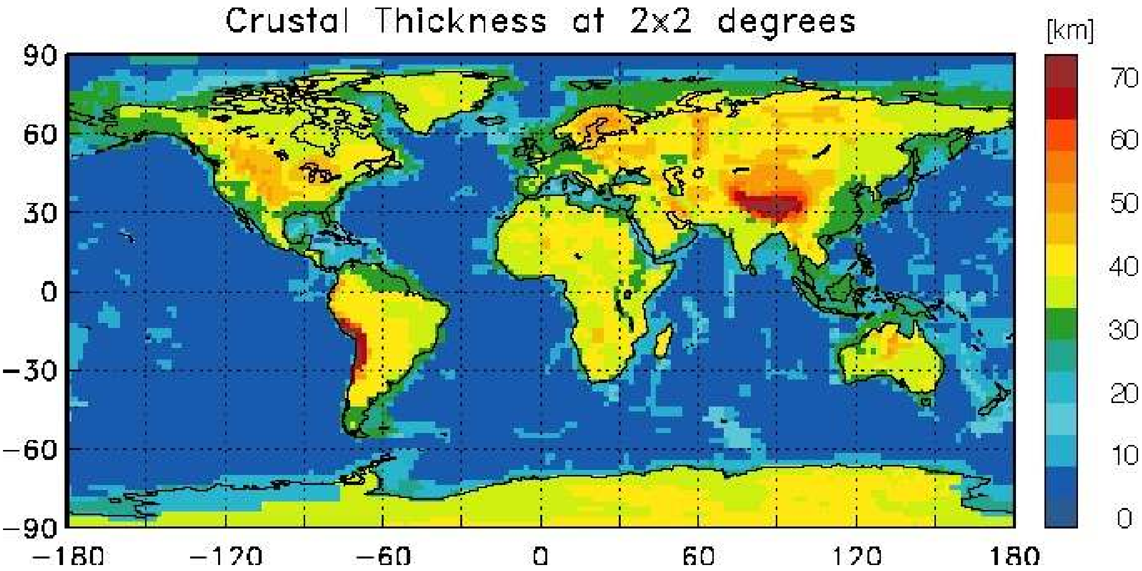

Figure 4.3: Crustal thickness at 2×2 degrees, based on the CRUST2.0 model, acquired from Laske et al. (2012).

crustal part of PREM is summarized in Table 4.1. The major differences between these models are the overall crustal thickness, the radius of the Earth, which is approximately 10 km shorter in the JAK Earth model, and the material properties, here described in terms of bulk modulus K. Bulk modulus (or incompressibility)

Table 4.1: The crustal characteristics of the Earth models JAK and PREM.

Layer	Thickness km	v_p km/s	v_s km/s	ρ kg/cm^3	E GPa	Upper radius km
CRUST2.0						
Ice	0.500	3.810	1.940	0.920	8.7	6361
Upper crust	13.000	6.200	3.600	2.800	59.2	6360
Midel crust	12.000	6.400	3.600	2.850	67.4	6347
Lower crust	12.000	6.800	3.800	2.950	79.6	6335
PREM						
Water	3.000	1.450	0.000	1.020	2.1	6371.0
Crust	12.000	5.800	3.200	2.600	52.0	6368.0
Crust	10.000	6.800	3.900	2.900	75.3	6356.0

describes the resistance of a material to uniform compression. Fig. 4.4 shows a plot of bulks modulus for the upper 50 km of the Earth models PREM (black) and JAK (light blue). Down to a depth of approximately 15 km the JAK Earth model has a higher Bulk modulus compared to PREM.

The vertical LDCs related to the Earth models PREM and JAK in (Fig. 4.1a) start to deviate from each other at the harmonic degree $n = 20$, and until $n = 400$ the JAK model results in the largest response. At higher harmonic degrees PREM results in the largest response. This is consistent with the bulk modulus of the layers (see Table 4.1 and Fig 4.4). A response to a large load (low harmonic degree) is affected by the deeper layers, while the one to small load is only affected by the upper part of the crust.

The vertical displacement for a disc with radius $\beta = 0.5$ km and a thickness $\Delta H = 1$ m are approximately 20% larger beneath the load for the solution based on PREM (solid black curve) compared to that based on JAK (dashed black curve) (Fig. 4.1b). As the distance from the load increases, the two solutions approach each other. This occurs at a distance of approximately 5 km. Fig. 4.5 shows the difference in vertical crustal displacement, related to the complex load distribution at Jakobshavn Isbræ (Fig. 3.7b), between the PREM and JAK solutions. The maximum difference between the two solutions is approximately ± 1 mm/yr. The uplift rates from these solutions at the GPS sites KAGA, ILUL, QEQE, and AASI are listed in table 4.2. At KAGA located 5 km from the front of Jakobshavn Isbræ the difference is 0.7 mm/yr, while the difference is zero at ILUL located 45 km from the front. Hence, the selection of Earth model is only important at sites located in the near vicinity of a large load like Jakobshavn Isbræ.

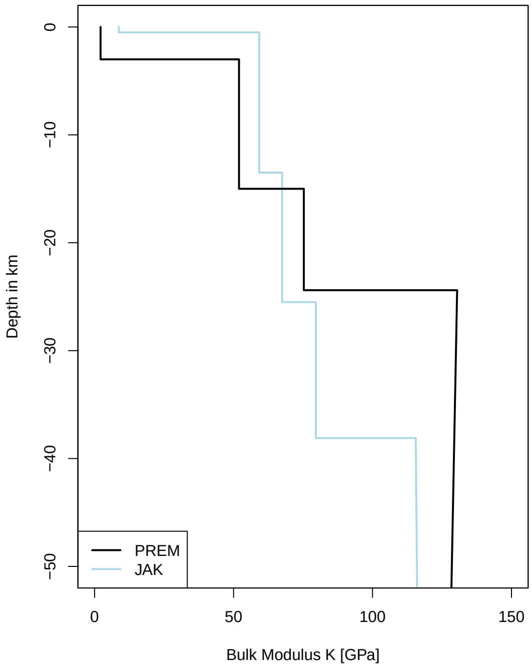

Figure 4.4: The Bulk modulus K in the upper 50 km for the Earth models PREM (black) and JAK (light blue).

Table 4.2: Vertical displacements related to the complex load distribution of Jakobshavn Isbræ. The responses are based on two set of LDCs, PREM and CRUST2.0.

Station	PREM mm/yr	CRUST2.0 mm/yr	Diff. mm/yr
KAGA	12.0	12.7	0.7
ILUL	3.0	3.0	0.0
QEQE	1.1	1.1	0.0
AASI	1.3	1.3	0.0

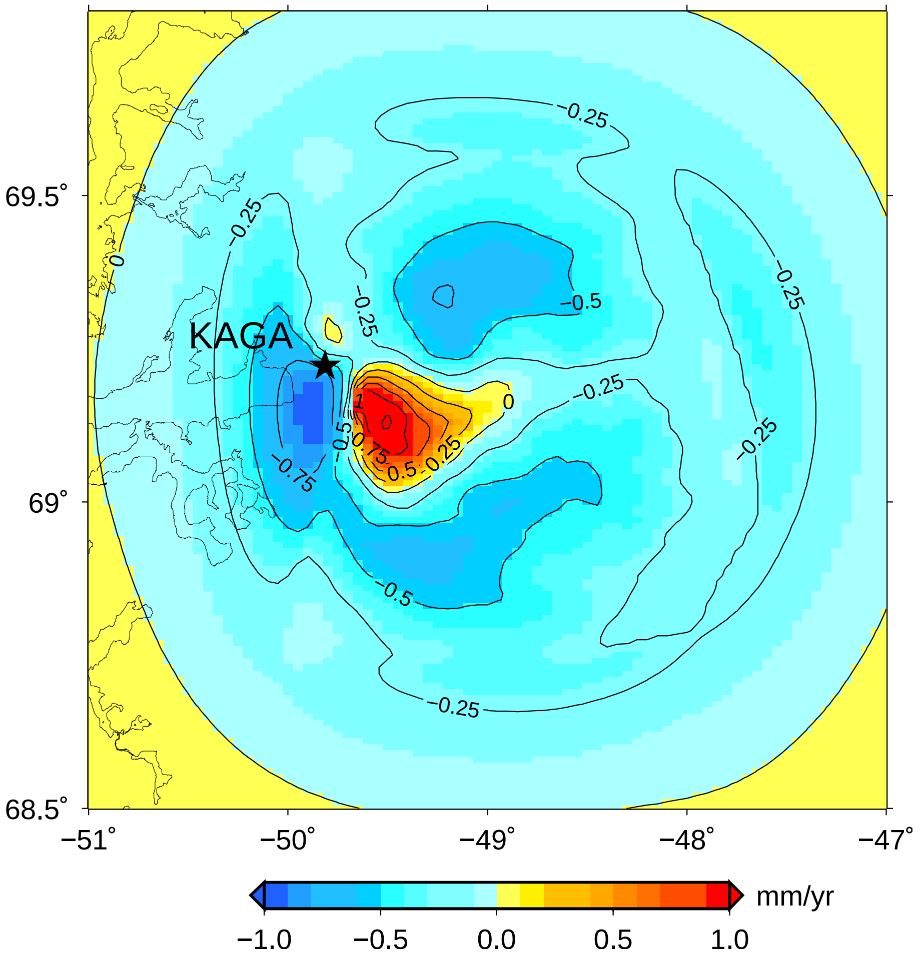

Figure 4.5: The difference in vertical displacements rates related to the complex load distribution at Jakobshavn Isbræ, between the PREM and CRUST2.0 solutions.

5

Glacial isostatic adjustment

During the last 500,000 years (Augustin et al., 2004) the Earth's climate has been following a cyclic pattern with a period of 100,000 years. These climatic variations can be studied in ice cores (Dahl-Jensen et al., 1998) and marine sediment records (Helmke et al., 2002). The cyclic behaviour results from changes in the orbital parameters (eccentricity, obliquity precession) of the Earth, and are referred to as Milankovitch cycles. A cycle contains a cold glacial period, where ice sheets build up, followed by a warm interglacial period, where ice sheets melts or are reduced. During glaciation ocean water is tied up in the ice sheets resulting in a sea level fall and a sea level rise during deglaciation. At the Last Glacial Maximum (LGM) the amount of water that was stored in the ice sheets was equivalent to a global sea level rise of 115-135 m (Milne et al., 2002). This variations in surface loading of ice and ocean water during a glacial cycle causes a response of the Earth, which can be summarized as GIA.

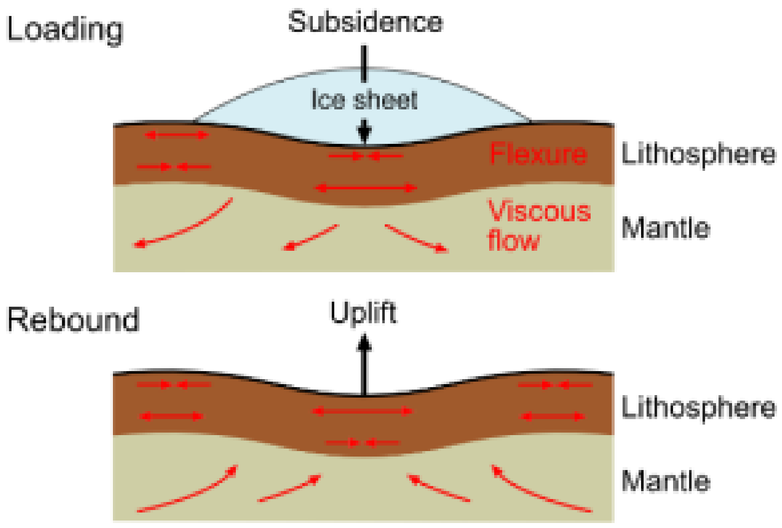

Figure 5.1: Schematic description of GIA. Adapted from GFZ (2012)

Figure 5.1 describes the basic principles in GIA. During glaciation the crust is deformed by the load of the ice sheets resulting in outward flow of mantle material beneath the load. During deglaciation the crust rebounds to its original position and mantle material flows back. The time scale of GIA is typically thousands of years. Besides crustal displacements, which are the primary interest in this thesis, and mass redistribution in the mantle GIA also effects the Earth rotation vector (Mitrovica et al., 2001) and the relative sea level (RSL). RSL is a height defined as the position of the interface between the ocean and the Earth. At present-day RSL=0. The surface of the ocean adjusts according to the gravitational attraction of the Earth. Hence, a change in the ice and ocean distribution and redistribution of mantle material will alter the surface of the ocean and thereby change the relative sea level. The relative sea level also changes as a consequence of the vertical displacement due to loading/unloading.

At present GIA is observed at former and present-day glaciated regions. At Former glaciated regions such as Fennoscandia and North America, crustal displacement related to GIA can be measured directly by GPS receivers. In these areas the observed present-day rates are up to 11 mm/yr (Lidberg et al., 2010; Sella et al., 2007). In areas that are currently glaciated such as Greenland and Antarctica the GIA response is mixed with the present day response caused by the ongoing melting. Hence, making it more difficult to measure the GIA response directly.

GIA depends on the rheology (the viscosity profile) of the Earth and the load distribution as a function of space and time. In the following these topics are discussed in more detail.

The relevant GIA variables, in this thesis, are rates of vertical and horizontal displacement. The contributions have been estimated using the publicly available software the Sea LevEL EquatioN solver (SELEN) version 2.9.8 (Section 5.4) (Spada and Stocchi, 2007), and the vertical and horizontal grids based on ICE-5G (VM2 L90) by Peltier.

5.1 Earth model

At timescales relevant to GIA the Earth acts both as an elastic and viscous solid. Materials that behaves is this way are called viscoelastic and may be represented by Maxwell rheology, where the strain rate is the sum of the elastic and viscous strain rates.

In GIA studies the structure of the Earth is typically approximated by an elastic lithosphere, a viscoelastic mantle and an inviscid core (the Lamé parameter, $\mu = 0$), where the material properties are assumed only to vary as a function of the radial distance. The mantle may be further subdivided into a finer layered structure, often into an upper and lower mantle. The lithosphere thickness generally varies between 70 and 120 km, and the mantle viscosity varies between 10^{19} and 10^{24} Pa s. The viscosity of a material describes its resistance when subjected to an applied stress. Hence, a material with a low viscosity will deform more easy compared to a material with a high viscosity. Furthermore, in GIA studies the Earth is often assumed to be self-gravitating and incompressible. For vertical displacement rates the assumption about incompressibility is appropriate, but for studies of horizontal displacement rates a compressible Earth yields a significant larger response (Tanaka et al., 2011).

5.2 Ice histories

An ice history, sometimes called a deglaciation history, is a model of the ice sheets as a function of space and time. At each location the ice thickness is given at a discrete set of times, typically from the LGM to present day, at each location. The extent of former ice sheets are constrained by geological data (e.g moraine deposits), and the total ice volume can be estimated from far field observations relative sea level (e.g. dating of corals and raised beached), which is a good representation of the eustatic sea level.

Ice history models are modeled through an iterative process, where the estimated sea level change in each time step is compared to data of relative sea level. The ice history and sometimes also the Earth model is then adjusted to obtain a better fit between the observed and predicted relative sea level. Ice models can furthermore be constrained by several glaciological parameters, and follow the physical dynamics of ice.

A widely used global ice histories is ICE-5G (Peltier, 2004). This model is constrained by relative sea level data and dynamic ice sheet modelling. The Greenlandic part of ICE-5G is described in Tarasov and Richard Peltier (2002). ICE-5G is derived simultaneously with the VM2 viscosity profile combined with a lithosphere thickness of 90 km.

Another global model is ANU05 by Kurt Lambeck. It consists of series of regional ice histories with different assumptions about the Earth model. The Greenlandic part, GREEN1, is described in Fleming and Lambeck (2004).

An example of a regional model for Greenland is the Huy2 ice history (Simpson et al., 2009). This model is a Calibration of the 3D thermomechanic ice sheet model Huy1 by (Hybrect 2002) using near field relative sea level data and geological evidence of past ice extent.

5.3 The seal level equation

The solid Earth response and the redistribution of water related to the melting of the late Quaternary ice sheets can be described by the sea level equation (SLE), which describes the spatial and temporal variations of sea level associated with these processes. In the system consisting of the solid Earth, the oceans, and the ice sheets a sea level changes caused by a mass redistribution in this system is given by (Farrell and Clark, 1976)

$$S(\omega,t) = \frac{\Phi}{g} - U + c, \tag{5.1}$$

where t is the time ω is the spatial position, Φ is the incremental perturbation in the gravity potential, g is the gravitational acceleration, U is the vertical displacement, and c is a constant that ensures conservation of mass within the system. According to Farrell and Clark (1976), the term $\frac{\Phi}{g} + c$ represents the change in the radius of the geoid. Hence, the sea level change related to GIA consists of two contributions; (1) the redistribution of masses causes the geoid to change and; (2) at the same time the surface of the solid Earth is displaced.

The SLE can more explicitly, here in the notation of Spada and Stocchi (2007), be written as

$$S(\omega,t) = \frac{\rho_i}{g} G_s \otimes_i I + \frac{\rho_w}{g} G_s \otimes_o S + S^E - \frac{\rho_i}{g} \overline{G_s \otimes_i I} - \frac{\rho_w}{g} \overline{G_s \otimes_o S}. \tag{5.2}$$

The first two terms in Eq. (5.2) are the sea level changes caused by the ice and water loads as a function of time, where ρ_i and ρ_w are the densities of ice and water, I and S are the ice and ocean loads as a function of position and time, $\otimes$ represents a convolution, and $G_s = G_\varphi + gG_u$, where G_φ and G_u are the Green's functions related to the potential perturbation and the vertical displacement. For a spherically, incompressible, and viscoelastic Earth these Green's functions are given by (Peltier, 1974)

$$\left\{ \begin{array}{c} G_u \\ \frac{1}{g} G_\varphi \end{array} \right\} (\alpha,t) = \frac{a}{m_e} \sum_{n=0}^{\infty} \left\{ \begin{array}{c} h_n(t) \\ \delta(t) + k_n \end{array} \right\} P_n(\cos(\alpha)), \tag{5.3}$$

where a and m_e are the radius and mass of the Earth, $h_n(t)$ and $k_n(t)$ are time dependent LDCs, δ is the Dirac delta function, P_n is the Legendre polynomial of harmonic degree n, and α is the colatitude. The last three terms in Eq. (5.2) represent the constant c in Eq. (5.1), where S^E is the eustatic sea level change and the overbars indicates an average over the surface of the oceans. The Eq. (5.2) is an integral equations, since the sea level change S is on both sides of (5.2), and must therefor be solved using iterative methods.

5.4 GIA predictions

There are some GIA solutions available on-line e.g Peltier's solution based on the ice history ICE-5G (VM2 L90) e.g. 1 × 1 degree grids of vertical and horizontal displacement, which are available at `http://www.atmosp.physics.utoronto.ca/~peltier/data.php`. This solution is based on a compressible, self gravitating, and spherical symmetric Earth. Another publicly available solution is Paulson's solution (Paulson et al., 2007) available at `http://grace.jpl.nasa.gov/data/pgr/`. This solution is also based on the ice history ICE-5G. It assumes an incompressible, self-gravitating, and spherically symmetric Earth. The mantle viscosity model VM2 is approximated with a four layered viscosity profile, with an upper mantle viscosity of 0.9 $\times 10^{21}$Pa s and a lower mantle viscosity of 3.6 $\times 10^{21}$Pa s.

SELEN (Spada and Stocchi, 2007) is a publicly available Fortran 90 program that solves the SLE, and outputs various GIA variables e.g. present-day rates of vertical and horizontal displacement. The program is implemented using the "pseudo-spectral" method (Mitrovica and Peltier, 1991). The Earth is assumed to be incompressible and radially stratified, where the mantle layers characterized by a viscoelastic rheology. In the version of SELEN (2.9.8) applied in this thesis the ocean function is constant, which means that the shorelines remain fixed in time. In SELEN the size of each time step is 1 kyr.

Table 5.1: Lithosphere thickness (LT) and upper and lower mantle viscosities (UMV and LMV) used in the GIA models.

Earth parameter	ICE-5G(Pe)	ICE-5G(Pa)	ANU05	Huy2
LT (km)	90	90	80	120
UMV ($\times 10^{21}$ Pa s)	VM2	0.9	0.4	0.5
LMV ($\times 10^{21}$ Pa s)	VM2	3.6	10.0	1.0

Fig 5.2 shows present-day GIA predictions of vertical displacement based on ICE-5G ((a) Peltier's solution and (b) Paulson's solution), ANU05 (c), and Huy2. The Earth model parameters are summarized in Table 5.1. These models have an overall similar structure, with uplift over the northern and eastern part of Greenland, subsidence in the central part and uplift at the southern part. However, there are differences in the magnitudes of the displacements. The predictions based on ICE-5G (Peltier) and Huy2 generally have larger displacement rates compared to the ANU05 and ICE-5G (Paulson) solutions. Though, based on the same ice history the Peltier and Paulson solutions have quite different rates. A part of this difference results naturally from the different assumptions taken. Recently some attempts have been made to benchmark different GIA codes (Spada et al., 2011).

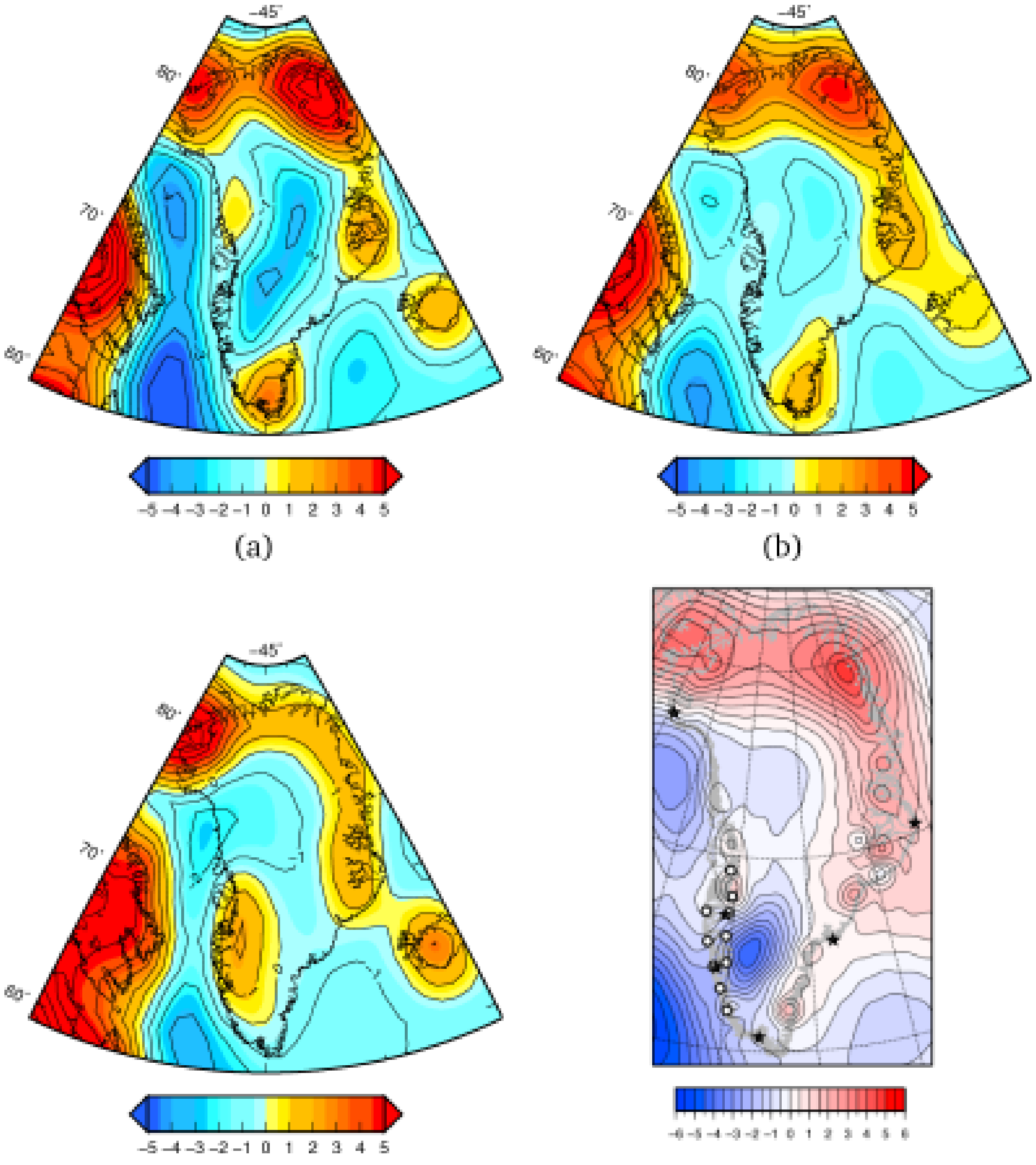

(a) (b) (c) (d)

Figure 5.2: GIA models of vertical displacement given in mm/yr. (a) Peltier's prediction based on ICE-5G, (b) Paulson's prediction based on ICE-5G, (c) predictions based on ANU05, and (d) Prediction based on Huy2, the non-Greenland part is based on ICE-5G. This plot is adapted from Simpson et al. (2011).

6

Combining observed and modeled crustal displacements

GPS measurements of crustal displacements in ice covered regions such as Greenland will contain responses from the present-day ice mass changes and ice load variations of the late-Pleistocene ice sheets. Without additional information these contributions cannot be separated. Hence, by combining observed rates of crustal displacement with modeled rates of the present-day (Chapter 4) and the GIA (Chapter 5) signals, a better understanding of these signals can be reached.

6.1 Constraining present-day glacial mass balance

The GPS sites in Greenland are grouped in pars, where one site is located near the glacier front and the other is located further towards the coast. This enables the study of displacement gradients. When considering gradients, the long wavelength signals such as the displacement from distant sources and GIA are reduced, since these tend to be of similar size at sites located relative close to one another. Hence, a displacement gradient will roughly represent the local mass changes and can therefor be used to constrain the local mass balance in the vicinity of the GPS sites.

This methodology is used in the papers Nielsen et al. (2012b) and Nielsen et al. (2012c), where relative displacements are used to constrain the mass balance of Upernavik Isstrøm and Jakobshavn Isbræ. The results are summarized in Table 6.1. It both studies the elastic response, related to the local mass changes (column 5), constitute the largest part of the observed displacement gradients, while GIA and the elastic response related to mass loss outside these glaciers represent a smaller part. The agreement between the observed and relative displacement rates are 0.6 mm/yr and 0.8 mm/yr for Upernavik Isstrøm and Jakobshavn Isbræ, respectively, which suggests that the local mass changes are well captured.

For a comparison the total modeled displacement rates have also been estimated without the local high resolution mass change grids. In these estimates the elastic response are based on the 2006-2009 ICESat-derived mass change grid. It is evident that the modeled relative rates between SRMP-UPVK (Upernavik Isstrøm) and KAGA-AASI (Jakobshavn Isbræ) are considerable higher when the local high resolution mass change grid is used, while the difference in the relative rates between ILUL-AASI and QEQE-AASI are insignificant. This indicates that the ICESat mass change grid captures the main part of the signal, but misses the shorter wavelength in the signal due to its lower resolution.

Table 6.1: Modeled and observed relative uplift rates in mm/yr. The second column displays GPS rates, third column the total modeled uplift rates, consisting of the elastic response from UI (column 5), the elastic response from outside UI (column 6), and GIA (column 7). The fourth column is the combined modeled rates, but where the elastic response is estimated only by the 2006-2009 ICESat mass change grid.

Station	GPS	Modeled total	ICSat only	Response local	Response regional	GIA	
			Upernavik Isstrøm				
SRMP-UPVK	8.6±0.8	9.2±4.2	5.5±0.4	7.0±4.2	1.7±0.3	0.5	(0.1;0.7)
			Jakobshavn Isbræ				
KAGA-AASI	12.8±0.6	12.0±2.1	8.7±0.4	11.4±2.1	1.8± 0.4	-1.2	(-0.6;1.1)
ILUL-AASI	1.9 ±0.4	2.1±0.9	1.7±0.4	1.7±0.8	0.9±0.3	-0.5	(-0.5;0.8)
QEQE-AASI	-0.1±0.4	-0.2±0.5	-0.1±0.4	-0.2±0.4	-0.1 ± 0.3	0.1	(-0.6;0.5)

6.2 Constraining glacial isostatic adjustment

The more than 50 permanent GPS sites (Fig. 3.1) located around the edge of the Greenland provide important constraints on the various GIA models available. However, to separate the GPS signal into the elastic and viscoelastic responses requires additional information. Here, the modeled elastic response is used to adjust the GPS rates to obtain constraints on the GIA estimates.

To obtain reliable constraints on the GIA estimates, using this method, require high resolution mass change grids in order to estimate the elastic response correctly. Another key point is that the GPS time series and the loading model used to derive the Earth's elastic response must cover approximately the same time span, since the spatial distribution of mass change and hence, the elastic displacement, may undergo rapid changes. In the paper, Nielsen et al. (2012a), it is demonstrated that the mass change pattern of the Greenland ice sheet varies considerably during the relative short time span 2004-2009. This is also shown on a more local scale in Nielsen et al. (2012b) and Nielsen et al. (2012c), where the mass loss pattern of Jakobshavn Isbræ and Upernavik Isstrøm undergo rapid changes. To reduce errors related to unmodeled elastic displacements it is advisable to use sites, which are located at some distance from areas with a considerable mass change, when constraining GIA.

Using the observed and modeled elastic response to constrain GIA rely solely on the assumption that the latter is estimated correctly. But without any validation of the modeled elastic response or other apriori information, this method may not provide reliable GIA constraints. Nielsen et al. (2012a) used temporal changes in observed and modeled elastic displacement rates to assess the validity of the modeled elastic response. The hypothesis in this analysis can be described as follows. Over a few decades the GIA response can be assumed constant. Hence, any temporal changes in the observed displacement rates are related to present-day changes. If the modeled elastic rates, related to these changes, show the same temporal behaviour, it indicates, that these rates are modeled correctly. However, a constant bias may be present, if the data resolution is too low to accurately represent the actual mass loss.

Fig. 6.1 shows temporal changes in the observed and modeled elastic rates, emphasized with dashed lines, at the five GPS sites KELY, SCOR, QAQ1, THU2, and KULU. The modeled elastic rates are based on ICESat-derived mass change grids, which are estimated using the M3 method presented in Sørensen et al. (2011). Based on this analysis, the modeled elastic response is assumed to be reliable at the sites KELY, SCOR, and QAQ1, due to the agreement in the temporal behaviour between the observed and modeled elastic rates. Though, the temporal behaviour agrees at the site KULU, this site is disregarded, due to a possible bias in the modeled elastic rates caused by the low resolution of ICESat data in the southern par of Greenland. The analyses is described in more detail in Nielsen et al. (2012a).

6.2.1 Preliminary evaluation of GIA models based on ICE-5G

In the following preliminary study, the observed (see Table 3.1) and modeled elastic rates that are presented in the papers Nielsen et al. (2012a), Nielsen et al. (2012b), and Nielsen et al. (2012c), plus rates at selected GNET sites, are used to put constraints on GIA models based on ICE-5G by Peltier and Paulson.

Fig. 6.2 shows Peltier's GIA model of vertical displacements for Greenland based on ICE-5G. This model is characterized by two distinct uplift centers in the northern part of Greenland, subsidence at the central part, and smaller uplift centers at

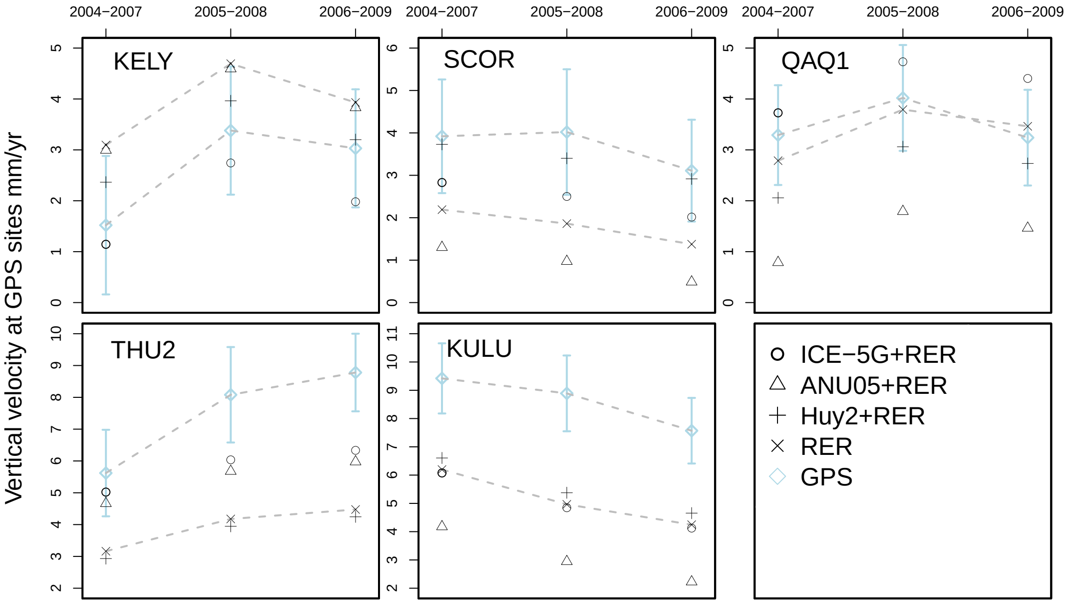

Figure 6.1: Temporal changes in observed and predicted vertical displacement rates at five permanent GPS sites (Nielsen et al., 2012a). The observed and modeled elastic rates are based on data from the three time periods 2004-2007, 2005-2008, and 2006-2009. The modeled elastic rates are derived from ICESat mass change grids, which are estimated according to the M3 method (Sørensen et al., 2011). The GIA predictions are based on the ice histories ICE-5G, ANU05, and Huy2.

the southern tip, and at the central part of the west and east coasts of Greenland. The location of the sites used in this study are also indicated in the figure.

The additional GPS sites used in this study are KMOR, KMJP, JGBL, NORD, and BLAS, located along the northern coast of Greenland. These sites are not affected too much by the present-day mass loss (see Fig. 3 in Nielsen et al. (2012a)) like the sites on the west and southeast coasts of Greenland. Hence, the elastic contribution is small. Furthermore, these sites are less affected by the 2010 melting/uplift anomaly (Bevis et al., 2012). The observed vertical displacement rates are adapted from Bevis et al. (2012). Information regarding these sites is summarized in Table 6.2.

To put constraints on the GIA estimates, the elastic response must be removed from the observed rates. Since the ICESat-derived mass change grids do not cover the entire observation period of the sites KMOR, KMJP, JGBL, NORD, and BLAS, accurate constraints cannot be estimated. However, these grids can still be used to set some bounds on the modeled elastic rates. Fig. 3 in Nielsen et al. (2012a) displays the variation in the modeled elastic displacement, derived from ICESat

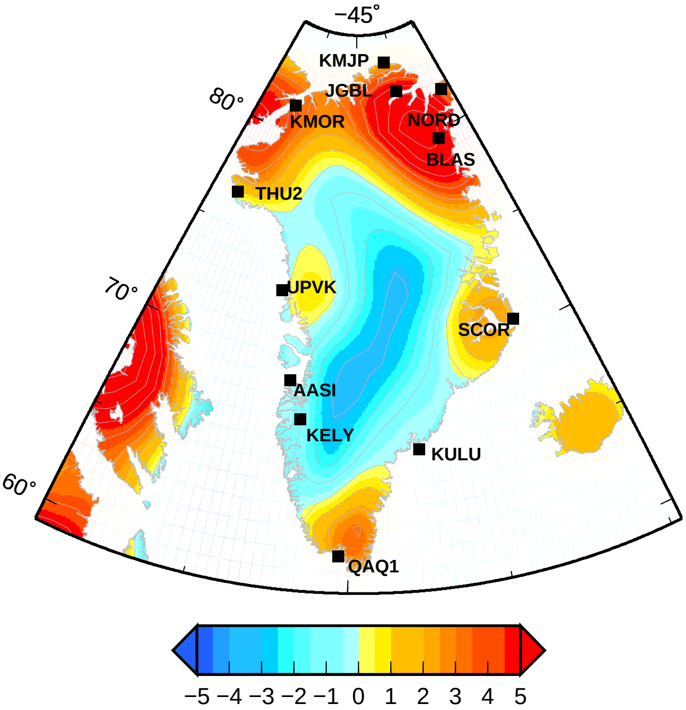

Figure 6.2: Peltier's GIA predictions of vertical displacements in mm/yr based on the ice history ICE-5G (VM2 L90). The location of selected GPS sites, that are used to constrain the GIA predictions, are indicated on top.

elevation changes, during the period 2004-2009. A minimum of elastic displacement over the northern part of Greenland is observed in the time span 2005-2008 (Fig. 3b) and a maximum in the time span 2006-2009. This trend is also observed by Kjær et al. (2012). They have estimated the mass change pattern of the Greenland ice sheet based on GRACE data in four time spans during the period 2003-2011. Their results show, that the mass loss rates in the northern part of Greenland between 2009 and 2011 do not exceed the minimum or maximum rates observed in the entire period. Hence, the elastic displacement rates based on the 2005-2008 and 2006-2009 ICESat-derived mass change grids, can be used as lower and upper bounds for the elastic displacement rates in the time span of the observed displacement rates.

The observed rates, which are corrected for the modeled elastic rates, are compared with two GIA models by Peltier and Paulson. The result of this preliminary analysis is displayed in Fig. 6.3. The gray squares represent the observed rates at the GPS sites and the black squares represent the corrected observed rates with 2σ error bars. The GIA solution span due to the possible range in the elastic displacement rates are indicated with pink color. The red and blue squares represent Peltier's and Paulsons's solutions, respectively. In the following the main focus will be on the sites, which have not been presented in Nielsen et al. (2012a). The

Table 6.2: Vertical displacement rates in mm/yr, adapted from Bevis et al. (2012).

Station	Lat	Lon	t_{start}	t_{end}	t_{span}	V_u	σ_u
KMOR	81.253	-63.527	2007.671	2011.247	3.6	7.5	0.3
KMJP	83.643	-33.377	2008.537	2011.247	2.7	4.5	0.4
JGBL	82.209	-31.004	2008.523	2011.242	2.7	4.3	0.4
NORD	81.600	-16.655	2006.717	2011.149	4.4	5.8	0.8
BLAS	79.539	-22.975	2008.515	2011.247	2.7	7.0	0.4

most striking differences in the estimates (Fig. 6.3) are seen at the sites JGBL and BLAS (Fig. 6.2). At these sites Peltier's GIA rates are considerable larger than the corrected observed rates. This suggests that Peltier's GIA model over predicts the vertical displacement rates at these sites. However, caution must be taken since the time spans of the GPS times series are only 2.7 years, and a local evaluation of the elastic displacements has not been done.

At the sites KMOR, KMJP, and NORD (Fig. 6.2) the agreement between the predicted GIA and corrected observed rates are within or almost within the error bars of the GPS rates, depending on the size of the elastic correction. At the sites UPVK and AASI (Fig. 6.2), the corrected observed rates are considerable higher that the predicted rates. In the papers Nielsen et al. (2012b) and Nielsen et al. (2012c) the modeled elastic displacement patterns near theses sites have been thoroughly studied and validated with observed rates. Hence, this might suggest, that the GIA models under predict the vertical displacement rates at these sites. The ice margin near the sites UPVK and AASI has retreated with approximately 20-30 km since the end of the LIA (Kollmeyer, 1980; Weidick, 1958). Post-LIA ice load changes are not included in ICE-5G, which might explain a part of the discrepancy between the predicted GIA rates and the corrected observed rates.

To summarize the results of this preliminary analysis it can be stated that: Peltier's modeled GIA rates of vertical displacement are most likely over predicted, in the north eastern uplift center in Greenland. The amplitude of the uplift center on the west coast of Greenland is probably under estimated. However, to make a more solid statement longer GPS time series of displacement and updated mass change grids are needed.

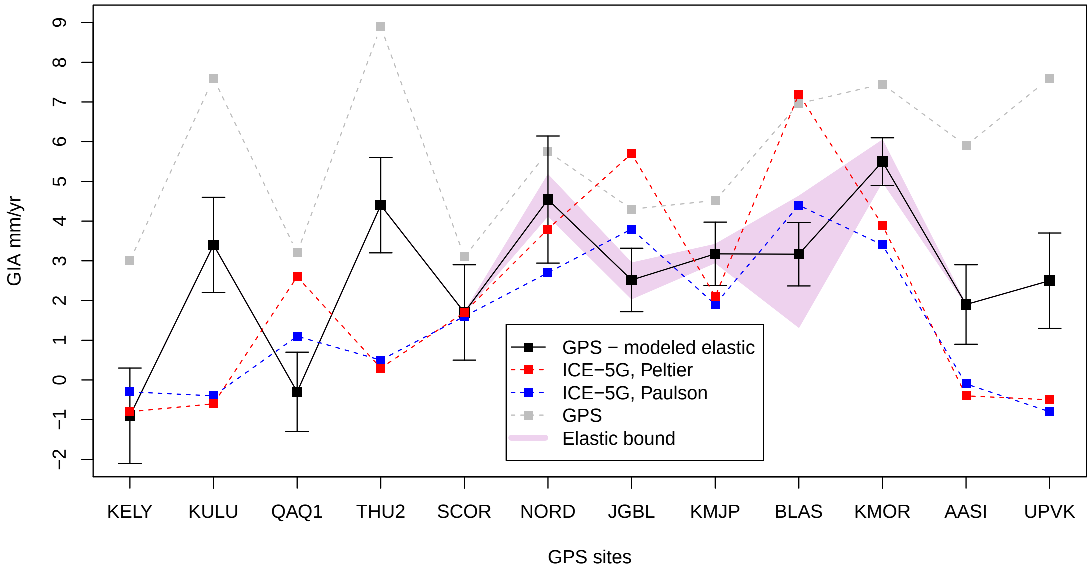

Figure 6.3: Vertical GIA displacement rates at selected GPS sites in Greenland. The observed rates (gray squares), which have been corrected for the elastic response, with 2σ error bars are indicated with black squares. These rates may vary due to the possible range in the elastic displacements, this variation is indicated with pink color. The red and blue squares represent GIA predictions, based on the ice history ICE-5G, by Peltier and Paulson, respectively.

7

Conclusions and suggestions for future work

In this PhD project modeling of elastic displacements related to the present-day ice mass variability has been a central part. Accurate models of the elastic displacement pattern are essential to separate the past and present-day contributions in the observed displacement rates.

Modeling of elastic displacements depend on the Earth model and the loading model i.e. the spatial distribution of ice loss over a time interval. Based on this study, the Earth modeled has only minor influence on the elastic displacement rates. In the vicinity of an area with a large mass loss, like Jakobshavn Isbræ, the difference in the elastic displacement rates are within a few mm based on the two Earth models PREM and JAK. However, the accuracy of the loading model, has a much higher influence on the elastic displacement rates. Especially near glaciers that experience a large ice mass loss a high resolution loading model is needed to obtain reliable elastic displacement rates.

In this PhD study, ICESat mass change grids combined with local high resolution mass change grids have been used to model elastic displacement rates near Upernavik Isstrøm (Nielsen et al., 2012b) and Jakobshavn Isbræ (Nielsen et al., 2012c). When relative rates are considered the agreement between the modeled and observed rates are 0.8 mm/yr or better. Since the relative rates roughly represent the local mass loss, this indicates, that the mass loss, and hence the modeled elastic rates, are well modeled.

Horizontal displacements have been studied near Jakobshavn Isbræ (Nielsen et al., 2012c) at the sites KAGA, ILUL, and QEQE relative to the site AASI. The displacements are directed towards west-northwest, suggesting that the main mass loss is located southeast of the GPS sites. This agrees well with the mass loss pattern obtained from ATM surface elevations (Fig 3.7b).

Elastic displacement rates can in combination with observed rates be used to constrain GIA models of vertical displacements. However, without any constraints on the modeled elastic displacements, reliable constraints may not be obtained. In

Nielsen et al. (2012a), temporal variations in the observed and modeled elastic rates at five permanent sites (KELY, THU2, SCOR, KULU and QAQ1) have been used to put some constraints on the modeled elastic rates. At sites, where the temporal variations agree, the modeled elastic displacements are considered more reliable. However, caution should be taken since a constant bias may be present, if the resolution of the loading model is to low. Based on the analysis in Nielsen et al. (2012a) the vertical displacement rates related to GIA are estimated to be approximately -1 ± 0.6 mm/yr at KELY, 2 ± 0.7 mm/yr at SCOR, and 0.5 ± 0.5 mm/yr at QAQ1. At the sites KULU and THU2 the resolution of the ICESat mass change grids is locally too low to accurately estimate the elastic displacement rates.

An interesting suggestion for future work could be to use the GNET displacement rates combined with modeled elastic displacement rates to constrain the GIA contribution. In this PhD study a preliminary analysis of this has been started, with focus on the northern part of Greenland. To obtain reliable constraints, accurate loading models are needed in the vicinity of the GNET sites. Hence, by combing the ICESat data with other measurements of surface elevation, locally improved mass changes grids can be obtained. Another approach, to put some constraints on the GIA rates, is to compare relative rates of the observed and modeled GIA displacement. By selecting sites locates far from the ice margin with approximately the same elastic response, the GIA signal can be isolated in the observed rates, and compared to the GIA rates.

This work has contributed with improved knowledge about the elastic displacements related to the present-day mass loss of the Greenland ice sheet. It has been demonstrated that with proper modeling of the elastic response it is possible to obtain rates that are accurate enough to constrain the GIA signal.

Bibliography

Alley, R., Clark, P., Huybrechts, P., Joughin, I., 2005. Ice-sheet and sea-level changes. Science 310 (5747), 456–460.

Altamimi, Z., Collilieux, X., Legrand, J., Garayt, B., Boucher, C., 2007. ITRF2005: A new release of the International Terrestrial Reference Frame based on time series of station positions and Earth Orientation Parameters. J. Geophys. Res. 112 (B9), B09401.

Augustin, L., Barbante, C., Barnes, P., Barnola, J., Bigler, M., Castellano, E., Cattani, O., Chappellaz, J., Dahl-Jensen, D., Delmonte, B., et al., 2004. Eight glacial cycles from an Antarctic ice core. Nature 429 (6992), 623–628.

Bassin, C., Laske, G., Masters, G., 2000. The current limits of resolution for surface wave tomography in North America. EOS, Trans. Am. Geophys. Un. 81, F897.

Bevis, M., Wahr, J., Khan, S., Madsen, F., Brown, A., Willis, M., Kendrick, E., Knudsen, P., Box, J., van Dam, T., et al., 2012. Bedrock displacements in Greenland manifest ice mass variations, climate cycles and climate change. P. Natl. Acad. Sci. USA.

Bjørk, A., Kjær, K., Korsgaard, N., Khan, S., Kjeldsen, K., Andresen, C., Larsen, N., Funder, S., 2012. An aerial view of 80 years of climate-related glacier fluctuations in southeast greenland. Nature Geoscience.

Böhm, J., Niell, A., Tregoning, P., Schuh, H., 2006. Global Mapping Function (GMF): A new empirical mapping function based on numerical weather model data. Geophys. Res. Lett. 33 (7), L07304.

Dahl-Jensen, D., Mosegaard, K., Gundestrup, N., Clow, G., Johnsen, S., Hansen, A., Balling, N., 1998. Past temperatures directly from the Greenland ice sheet. Science 282 (5387), 268.

De Linage, C., Hinderer, J., Rogister, Y., 2007. A search for the ratio between gravity variation and vertical displacement due to a surface load. Geophysical Journal International 171 (3), 986–994.

Dietrich, R., Ivins, E., Casassa, G., Lange, H., Wendt, J., Fritsche, M., 2010. Rapid crustal uplift in Patagonia due to enhanced ice loss. Earth Planet. Sc. Lett. 289 (1-2), 22–29.

Dietrich, R., Rülke, A., Scheinert, M., 2005. Present-day vertical crustal deformations in west greenland from repeated gps observations. Geophys. Journal International 163 (3), 865–874.

Dziewonski, A., Anderson, D., 1981. Preliminary reference Earth model. Phys. Earth Planet. In. 25 (4), 297–356.

Farrell, W., 1972. Deformation of the Earth by surface loads. Rev. Geophys. 10 (3), 761–797.

Farrell, W., Clark, J., 1976. On postglacial sea level. Geophys. J. Royal Astr. S. 46 (3), 647–667.

Fleming, K., Lambeck, K., 2004. Constraints on the Greenland Ice Sheet since the Last Glacial Maximum from sea-level observations and glacial-rebound models. Quaternary Sci. Rev. 23 (9-10), 1053–1077.

GFZ, 2012. Gfz-fig. Accesed August 2012.
URL `http://www.gfz-potsdam.de/portal/gfz/Struktur/Departments/Department+1/sec13/resources/Images/scetch3`

Helmke, J., Schulz, M., Bauch, H., 2002. Sediment-color record from the Northeast Atlantic reveals patterns of millennial-scale climate variability during the past 500,000 years. Quaternary Res. 57 (1), 49–57.

Howat, I. M., Ahn, Y., Joughin, I., van den Broeke, M. R., Lenaerts, J. T. M., Smith, B., 2011. Mass balance of Greenland's three largest outlet glaciers, 2000-2010. Geophys. Res. Lett. 38, L12501.

Jacob, T., Wahr, J., Pfeffer, W., Swenson, S., 2012. Recent contributions of glaciers and ice caps to sea level rise. Nature.

Joughin, I., Howat, I., Fahnestock, M., Smith, B., Krabill, W., Alley, R., Stern, H., Truffer, M., 2008. Continued evolution of Jakobshavn Isbrae following its rapid speedup. J Geophys Res 113 (F4), F04006.

Joughin, I., Smith, B., Howat, I., Scambos, T., Moon, T., 2010. Greenland flow variability from ice-sheet-wide velocity mapping. J. Glaciol. 56 (197), 415–430.

Khan, S., Liu, L., Wahr, J., Howat, I., Joughin, I., van Dam, T., Fleming, K., 2010b. GPS measurements of crustal uplift near Jakobshavn Isbræ due to glacial ice mass loss. J. Geophys. Res. 115 (B9), B09405.

Khan, S., Wahr, J., Leuliette, E., van Dam, T., Larson, K., Francis, O., 2008. Geodetic measurements of postglacial adjustments in Greenland. J. Geophys. Res. 113 (B2), B02402.

Khan, S., Wahr, J., Stearns, L., Hamilton, G., van Dam, T., Larson, K., Francis, O., 2007. Elastic uplift in southeast Greenland due to rapid ice mass loss. Geophys. Res. Lett. 34 (21), L21701.

Kjær, K., Khan, S., Korsgaard, N., Wahr, J., Bamber, J., Hurkmans, R., van den Broeke, M., Timm, L., Kjeldsen, K., Bjørk, A., et al., 2012. Aerial Photographs Reveal Late–20th-Century Dynamic Ice Loss in Northwestern Greenland. Science 337 (6094), 569–573.

Kollmeyer, R., 1980. West Greenland outlet glaciers: an inventory of the major iceberg producers. In: World Glacier Inventory Workshop: Proceedings of the Workshop at Riederalp, Switzerland September 1978. IAHS-AISH Publication. No. 126.

Krabill, W. B., 2011. IceBridge ATM L2 Icessn Elevation, Slope, and Roughness, [1994-2011]. Boulder, Colorado USA: NASA Distributed Active Archive Center at the National Snow and Ice Data Center. Digital media.
URL `http://nsidc.org/data/ilatm2.html`

Krabill, W. B., Thomas., R. H., 2010. Pre-icebridge atm l2 icessn elevation, slope, and roughness, [2005-2008]. Boulder, Colorado USA: NASA Distributed Active Archive Center at the National Snow and Ice Data Center. Digital media.
URL `http://nsidc.org/data/blatm2.html.`

Kustowski, B., Ekström, G., Dziewonski, A., 2008. Anisotropic shearwave velocity structure of the Earth's mantle: a global model. J. geophys. Res. 113 (10.1029).

Larsen, C., Motyka, R., Freymueller, J., Echelmeyer, K., Ivins, E., 2005. Rapid viscoelastic uplift in southeast Alaska caused by post-Little Ice Age glacial retreat. Earth Planet. Sc. Lett. 237 (3), 548–560.

Laske, G., Masters, G., Reif, C., 2012. Crust2.0. Web, accessed June, 2012.
URL `http://igppweb.ucsd.edu/~gabi/crust2.html`

Lidberg, M., Johansson, J. M., Scherneck, H.-G., Milne, G. A., 2010. Recent results based on continuous gps observations of the gia process in fennoscandia from bifrost. Journal of Geodynamics 50 (1), 8 – 18, <ce:title>Upper Mantle Dynamics and Quaternary Climate in Cratonic Areas (DynaQlim) &mdash; Understanding the Glacial Isostatic Adjustment</ce:title>.
URL `http://www.sciencedirect.com/science/article/pii/S0264370709001665`

Longman, I., 1962. A Green's Function for determining the deformation of the Earth under surface mass loads 1. Theory. J Geophys Res 67 (2), 845–850.

McFadden, E., Howat, I., Joughin, I., Smith, B., Ahn, Y., 2011. Changes in the dynamics of marine terminating outlet glaciers in west Greenland (2000–2009). J. Geophys. Res. 116 (F2), F02022.

Mémin, A., Hinderer, J., Rogister, Y., 2011. Separation of the geodetic consequences of past and present ice-mass change: Influence of topography with application to Svalbard (Norway). Pure and Applied Geophysics, 1–16.

Milne, G., Mitrovica, J., Schrag, D., 2002. Estimating past continental ice volume from sea-level data. Quaternary Sci. Rev. 21 (1-3), 361–376.

Mitrovica, J., Milne, G., Davis, J., 2001. Glacial isostatic adjustment on a rotating Earth. Geophys. J. Int. 147 (3), 562–578.

Mitrovica, J., Peltier, W., 1991. On postglacial geoid subsidence over the equatorial oceans. J. Geophys. Res. 96 (B12), 20053–20071.

NASA-GLAS, 2012. Glas instrument. Accessed June, 2012.
URL `http://icesat.gsfc.nasa.gov/icesat/glas.php`

NASA-IceBridge, 2012. Icebridge home. Accessed June 2012.
URL `http://www.nasa.gov/mission\_pages/icebridge/index.html`

NASA-ICESat, 2012. Icesat home. Accessed June, 2012.
URL `http://icesat.gsfc.nasa.gov/icesat/`

Nielsen, K., Sørensen, L. S., Khan, S. A., Spada, G., Simonsen, S. B., Forsberg, R., 2012a. Towards constraining glacial isostatic adjustment in Greenland using ICESat and GPS observations. International Association of Geodesy Symposia XX, XXXX, accepted.

Nielsen, K., Khan, S. A., Korsgaard, N. J., Kjær, K. H., Wahr, J., Bevis, M., Stearns, L. A., Timm, L. H., 2012b. Crustal uplift due to ice mass variability on Upernavik Isstrøm, west Greenland. Earth Planet. Sc. Lett. XX, XXXX, accepted.

Nielsen, K., Khan, S. A., Spada, G., Wahr, J., Bevis, M., Liu, L., van Dam, T., 2012c. Vertical and horizontal surface displacements near Jakobshavn Isbræ driven by melt-induced and dynamic ice loss. J. Geophys. Res. XX, XXXX, submitted.

NSIDC-IceBridge, 2012. Icebridge data. web, accessed, June 2012.
URL `http://nsidc.org/data/icebridge/index.html`

NSIDC-ICESat, 2012. Icesat data. web, accessed, July 2012.
URL `http://nsidc.org/data/icesat/order.html`

Paulson, A., Zhong, S., Wahr, J., 2007. Inference of mantle viscosity from GRACE and relative sea level data. Geophys. J. Int. 171 (2), 497–508.

Peltier, W., 1974. The impulse response of a Maxwell Earth. Rev. Geophys. Space Phys 12 (4), 649–669.

Peltier, W., 2004. Global glacial isostasy and the surface of the ice-age Earth: the ICE-5G (VM2) model and GRACE. Annu. Rev. Earth Planet. Sci. 32, 111–149.

Pritchard, H., Arthern, R., Vaughan, D., Edwards, L., 2009. Extensive dynamic thinning on the margins of the Greenland and Antarctic ice sheets. Nature 461 (7266), 971–975.

Rignot, E., Kanagaratnam, P., 2006. Changes in the velocity structure of the Greenland Ice Sheet. Science 311 (5763), 986.

Rignot, E., Velicogna, I., Van den Broeke, M., Monaghan, A., Lenaerts, J., 2011. Acceleration of the contribution of the greenland and antarctic ice sheets to sea level rise. Geophysical Research Letters 38 (5), L05503.

Sasgen, I., van den Broeke, M., Bamber, J., Rignot, E., Sørensen, L., Wouters, B., Martinec, Z., Velicogna, I., Simonsen, S., 2012. Timing and origin of recent regional ice-mass loss in Greenland. Earth Planet. Sc. Lett. 333, 293–303.

Sato, T., Okuno, J., Hinderer, J., MacMillan, D., Plag, H., Francis, O., Falk, R., Fukuda, Y., 2006. A geophysical interpretation of the secular displacement and gravity rates observed at Ny-ålesund, Svalbard in the Arctic-effects of postglacial rebound and present-day ice melting. Geophys. J. Int. 165 (3), 729–743.

Scherneck, H., Bos, M., 2002. Ocean Tide and Atmospheric Loading. In: Vandenberg, N. R., Baver, K. D. (Eds.), IVS 2002 General Meeting Proceedings, Tsukuba, Feb. 4-7, 2002. NASA Goddard Space Flight Center, pp. 205–214.
URL `ftp://ivscc.gsfc.nasa.gov/pub/general-meeting/2002/pdf/scherneck.pdf`

Schrama, E., Wouters, B., Vermeersen, B., 2011. Present day regional mass loss of Greenland observed with satellite gravimetry. Surv. Geophys., 1–9.

Sella, G., Stein, S., Dixon, T., Craymer, M., James, T., Mazzotti, S., Dokka, R., 2007. Observation of glacial isostatic adjustment in" stable" north america with gps. Geophys. Res. Lett. 34 (2), 2306.

Simpson, M., Milne, G., Huybrechts, P., Long, A., 2009. Calibrating a glaciological model of the Greenland ice sheet from the last Glacial Maximum to present-day using field observations of relative sea level and ice extent. Quaternary Sci. Rev. 28 (17), 1631–1657.

Simpson, M., Wake, L., Milne, G., Huybrechts, P., 2011. The influence of decadal- to millennial-scale ice mass changes on present-day vertical land motion in Greenland: Implications for the interpretation of GPS observations. J. Geophys. Res. 116 (B2), B02406.

Slobbe, D., Ditmar, P., Lindenbergh, R., 2009. Estimating the rates of mass change, ice volume change and snow volume change in Greenland from ICESat and GRACE data. Geophys J Int 176 (1), 95–106.

Solomon, S., 2007. Climate change 2007: the physical science basis: contribution of Working Group I to the Fourth Assessment Report of the Intergovernmental Panel on Climate Change. Cambridge Univ Pr.

Sørensen, L., Forsberg, R., 2010. Greenland ice sheet mass loss from grace monthly models. Gravity, Geoid and Earth Observation, 527–532.

Sørensen, L. S., 2011. Changes of the greenland ice sheet - derived from icesat and grace data. Ph.D. thesis, The PhD School of Science, Faculty of Science, University of Copenhagen.

Sørensen, L. S., Simonsen, S. B., Nielsen, K., Lucas-Picher, P., Spada, G., Adalgeirsdottir, G., Forsberg, R., Hvidberg, C. S., 2011. Mass balance of the Greenland ice sheet (2003–2008) from ICESat data - the impact of interpolation, sampling and firn density. The Cryosphere 5 (1), 173–186.

Spada, G., 2003. The theory behind TABOO. Samizdat Press, Golden-White River Junction.
URL `http://samizdat.mines.edu/taboo/`

Spada, G., Barletta, V., Klemann, V., Riva, R., Martinec, Z., Gasperini, P., Lund, B., Wolf, D., Vermeersen, L., King, M., 2011. A benchmark study for glacial isostatic adjustment codes. Geophys J Int 185, 106–132.

Spada, G., Ruggieri, G., Sørensen, L., Nielsen, K., Melini, D., Colleoni, F., 2012. Greenland uplift and regional sea level changes from ICESat observations and GIA modelling. Geophys. J. Int. 189, 1457–1474.
URL `http://onlinelibrary.wiley.com/doi/10.1111/j.1365-246X.2012.05443.x/abstract`

Spada, G., Stocchi, P., 2007. SELEN: A Fortran 90 program for solving the“sea-level equation”. Comput. Geosci. 33, 538–562.

Tanaka, Y., Klemann, V., Martinec, Z., Riva, R., 2011. Spectral-finite element approach to viscoelastic relaxation in a spherical compressible Earth: application to GIA modelling. Geophys. J. Int. 184 (1), 220–234.

Tarasov, L., Richard Peltier, W., 2002. Greenland glacial history and local geodynamic consequences. Geophysical Journal International 150 (1), 198–229.

Tedesco, M., Fettweis, X., Van den Broeke, M., Van de Wal, R., Smeets, C., van de Berg, W., Serreze, M., Box, J., 2011. The role of albedo and accumulation in the 2010 melting record in Greenland. Environ. Res. Lett. 6, 014005.

Thomas, I., King, M., Bentley, M., Whitehouse, P., Penna, N., Williams, S., Riva, R., Lavallee, D., Clarke, P., King, E., et al., 2011. Widespread low rates of Antarctic glacial isostatic adjustment revealed by GPS observations. Geophys. Res. Lett. 38 (22), L22302.

Tushingham, A., Peltier, W., 1991. Ice-3 g- a new global model of late Pleistocene deglaciation based upon geophysical predictions of post-glacial relative sea level change. J. Geophys. Res. 96 (B3), 4497–4523.

Van Den Broeke, M., Bamber, J., Ettema, J., Rignot, E., Schrama, E., Van de Berg, W., Van Meijgaard, E., Velicogna, I., Wouters, B., 2009. Partitioning recent Greenland mass loss. Science 326 (5955), 984–986.

Velicogna, I., 2009. Increasing rates of ice mass loss from the Greenland and Antarctic ice sheets revealed by GRACE. Geophys Res Lett 36 (19), L19503.

Velicogna, I., Wahr, J., 2005. Greenland mass balance from grace. Geophys. Res. Lett 32 (18), L18505.

Wahr, J., DaZhong, H., Trupin, A., 1995. Predictions of vertical uplift caused by changing polar ice volumes on a viscoelastic Earth. Geophys. Res. Lett. 22 (8), 977–980.

Wahr, J., van Dam, T., Larson, K., Francis, O., 2001a. Geodetic measurements in Greenland and their implications. J Geophys Res 106 (16), 567–581.

Wahr, J., van Dam, T., Larson, K., Francis, O., 2001b. GPS measurements of vertical crustal motion in Greenland. J Geophys Res 106 (D24), 33755–33.

Weidick, A., 1958. Frontal variations at Upernaviks Isstrom in the last 100 years. Gronland Geologiske Undersogelse. Misc. Papers no. 21, Geological Survey of Greenland, Copenhagen.

Zumberge, J., Heflin, M., Jefferson, D., Watkins, M., Webb, F., 1997. Precise point positioning for the efficient and robust analysis of GPS data from large networks. J. Geophys. Res. 102 (B3), 5005–5017.

I

Mass balance of the Greenland ice sheet (2003–2008) from ICESat data - the impact of interpolation, sampling and firn density

By

Sørensen, L. S., Simonsen, S. B., Nielsen, K., Lucas-Picher, P., Spada, G.,
Adalgeirsdottir, G., Forsberg, R. and Hvidberg, C. S.

Publication details

Published in *The Cryosphere* **5**:173–186.

The Cryosphere, 5, 173–186, 2011
www.the-cryosphere.net/5/173/2011/
doi:10.5194/tc-5-173-2011

The Cryosphere

Mass balance of the Greenland ice sheet (2003–2008) from ICESat data – the impact of interpolation, sampling and firn density

L. S. Sørensen[1,2,*], **S. B. Simonsen**[3,4,*], **K. Nielsen**[5], **P. Lucas-Picher**[4], **G. Spada**[6], **G. Adalgeirsdottir**[4], **R. Forsberg**[1], **and C. S. Hvidberg**[3]

[1]Geodynamics Department, DTU Space, Juliane Maries vej 30, 2100 Copenhagen, Denmark
[2]Planet and Geophysics, NBI, University of Copenhagen, Juliane Maries Vej 30, 2100 Copenhagen, Denmark
[3]Centre for Ice and Climate, NBI, University of Copenhagen, Juliane Maries Vej 30, 2100 Copenhagen, Denmark
[4]Danish Climate Centre, DMI, Lyngbyvej 100, 2100 Copenhagen, Denmark
[5]Geodesy Department, DTU Space, Juliane Maries vej 30, 2100 Copenhagen, Denmark
[6]Dipartimento di Scienze di Base e Fondamenti, Urbino University “Carlo Bo”, Via Santa Chiara, 27,
61029 Urbino (PU), Italy
[*]These authors contributed equally to this work.

Received: 20 September 2010 – Published in The Cryosphere Discuss.: 15 October 2010
Revised: 1 February 2011 – Accepted: 10 February 2011 – Published: 9 March 2011

Abstract. ICESat has provided surface elevation measurements of the ice sheets since the launch in January 2003, resulting in a unique dataset for monitoring the changes of the cryosphere. Here, we present a novel method for determining the mass balance of the Greenland ice sheet, derived from ICESat altimetry data.

Three different methods for deriving elevation changes from the ICESat altimetry dataset are used. This multi-method approach provides a method to assess the complexity of deriving elevation changes from this dataset.

The altimetry alone can not provide an estimate of the mass balance of the Greenland ice sheet. Firn dynamics and surface densities are important factors that contribute to the mass change derived from remote-sensing altimetry. The volume change derived from ICESat data is corrected for changes in firn compaction over the observation period, vertical bedrock movement and an intercampaign elevation bias in the ICESat data. Subsequently, the corrected volume change is converted into mass change by the application of a simple surface density model, in which some of the ice dynamics are accounted for. The firn compaction and density models are driven by the HIRHAM5 regional climate model, forced by the ERA-Interim re-analysis product, at the lateral boundaries.

We find annual mass loss estimates of the Greenland ice sheet in the range of $191 \pm 23\,\mathrm{Gt\,yr^{-1}}$ to $240 \pm 28\,\mathrm{Gt\,yr^{-1}}$ for the period October 2003 to March 2008. These results are in good agreement with several other studies of the Greenland ice sheet mass balance, based on different remote-sensing techniques.

1 Introduction

Different satellite based measuring techniques have been used to observe the present-day changes of the Greenland ice sheet (GrIS). Synthetic Aperture Radar (SAR) imaging reveals an acceleration of a large number of outlet glaciers in Greenland (Abdalati et al., 2001; Rignot et al., 2004; Rignot and Kanagaratnam, 2006; Joughin et al., 2010). Gravity changes observed by the Gravity Recovery And Climate Experiment (GRACE) show a significant mass loss (Velicogna and Wahr, 2005; Luthcke et al., 2006; Wouters et al., 2008; Sørensen and Forsberg, 2010; Wu et al., 2010). The local elevation changes of the GrIS with significant thinning along the ice margin are revealed by laser altimetry (Slobbe et al., 2008; Howat et al., 2008; Pritchard et al., 2009).

In this study, a novel mass balance estimate of the GrIS for the period 2003–2008 is presented, derived from elevation measurements from NASA’s Ice, Cloud and land Elevation Satellite (ICESat), firn compaction and surface density modelling.

Correspondence to: L. S. Sørensen
(slss@space.dtu.dk)

Published by Copernicus Publications on behalf of the European Geosciences Union.

Different methods have been used to derive secular surface elevation change estimates $\left(\frac{dH}{dt}\right)$ of snow- or ice-covered areas from ICESat data (Fricker and Padman, 2006; Howat et al., 2008; Slobbe et al., 2008; Pritchard et al., 2009). Here we use three different methods to derive $\frac{dH}{dt}$ and the differences are investigated.

The total volume change of the GrIS is found by fitting a smooth surface, which covers the entire ice sheet, to the ICESat derived $\frac{dH}{dt}$ estimates. The conversion of the derived $\frac{dH}{dt}$ values to a mass change is based on various elevation change correction terms and a simple surface density model. The firn correction and the surface density models are forced by climate parameters from a regional climate model (RCM). Other studies have linked climate models and surface mass balance models in order to estimate the mass balance of the GrIS (Li et al., 2007; van den Broeke et al., 2009; Zwally et al., 2011), but in our approach, we directly use the estimated $\frac{dH}{dt}$ values from ICESat to derive the total mass balance including firn dynamics, driven by the HIRHAM5 high resolution RCM (Sect. 5.2).

The first part of this paper is dedicated to the description of the ICESat data and the methods used for deriving elevation and volume changes of the GrIS (Sects. 2 to 3). The volume change estimates and their associated uncertainties are presented in Sect. 4.

In the second part of this paper, the conversion from volume to mass is described (Sects. 5 to 7). This includes the changes in the firn compaction and surface density of the GrIS. The theoretical treatment of the firn processes is presented in Sect. 5. In Sect. 6, additional elevation changes, that do not contribute to the mass balance of the ice sheet, are described and quantified. The findings from both observations and model treatment are combined to derive the total mass balance of the GrIS, which is presented in Sect. 7, along with an error analysis of the mass balance.

2 ICESat data

ICESat carries the Geoscience Laser Altimeter System (GLAS) instrument (Abshire et al., 2005). Technical problems with the GLAS instrument early in the mission have resulted in a significant reduction in repeated tracks and, hence, in spatial resolution. As a consequence of this and due to the inclination of the satellite, the tracks are separated by approximately 30 km in the southern part of Greenland.

The GLAS/ICESat Antarctic and Greenland Ice Sheet Altimetry Data product (GLA12) (Zwally et al., 2010) was downloaded from the National Snow and Ice Data Center. This level-2 altimetry product provides geolocated and time tagged ice sheet surface elevation estimates, with respect to the TOPEX/Poseidon reference ellipsoid. The satellite laser footprint size is 30–70 m and the distance between the footprint centres is approximately 170 m. This study is based on the 91-day repeat cycle ICESat data (release 31) from October 2003 to March 2008. The time span and release number of the laser campaigns in the dataset are listed in Table 1.

Table 1. ICESat data description. Shown is the laser campaign identifier (ID), data release number (RL), and time span of the campaigns. N and M are the number of measurements from the GrIS before and after the data culling, respectively.

ID	RL	Time span	N	M
L2A	531	4 Oct 2003–18 Nov 2003	1 095 647	941 052
L2B	531	17 Feb 2004–20 Mar 2004	815 998	695 242
L2C	531	18 May 2004–20 Jun 2004	739 672	680 031
L3A	531	3 Oct 2004–8 Nov 2004	851 789	727 425
L3B	531	17 Feb 2005–24 Mar 2005	829 689	704 680
L3C	531	20 May 2005–22 Jun 2005	800 876	679 827
L3D	531	21 Oct 2005–23 Nov 2005	821 825	695 949
L3E	531	22 Feb 2006–27 Mar 2006	883 492	752 123
L3F	531	24 May 2006–25 Jun 2006	743 702	626 463
L3G	531	25 Oct 2006–27 Nov 2006	809 655	698 710
L3H	531	12 Mar 2007–14 Apr 2007	838 647	778 350
L3I	531	2 Oct 2007–4 Nov 2007	761 576	705 639
L3J	531	17 Feb 2008–21 Mar 2008	375 239	368 148
Total			10 367 807	9 053 639

ICESat data pre-processing

A procedure of data culling and the application of corrections is necessary to reduce some of the systematic errors in the ICESat dataset and to remove problematic measurements (Smith et al., 2005). Saturation of the waveform can induce errors in surface elevation estimates (Fricker et al., 2005). Applying the saturation correction to the relevant measurements, which are flagged in the data files, reduces these errors (NSIDC, 2010). We have also used the standard deviation of the difference between the shape of the return signal and a Gaussian functional fit (the IceSvar parameter), to evaluate the data. Large standard deviations indicate less reliable surface elevation estimates (Smith et al., 2009), and measurements for which the misfit is large (IceSvar ≥ 0.04 V) are rejected from the further analysis. Multiple peaks can be caused by reflections from clouds and by topography in the illuminated footprint. All measurements that contain more than one peak in the return signal are rejected from the analysis. Besides these two criteria, we have also used data quality flags and warnings given with the data to reject problematic measurements. We find that these thresholds result in an overall reduction of crossover errors, see Supplement.

Only measurements from the GrIS and the surrounding glaciers and ice caps are considered in the elevation change analysis (Csatho et al., 2009). The total number of ICESat measurements from the ice covered areas is 10 367 807. After rejecting problematic measurements in the data culling procedure, the number is reduced by approximately 13% to 9 053 639, see Table 1. In the data culling, 78.4% of the rejected data are rejected by various quality and warning flags, 21.1% by the IceSVar parameter and only 0.5% are rejected by the number of peaks criterion.

3 Methods for deriving surface elevation changes

An observed surface elevation difference may include a seasonal signal and a secular trend, but also components which are not related to the ice sheet mass balance. The seasonal variations are caused by variations in accumulation, flow, melt and a temperature dependent firn compaction rate. The compaction of the firn, the vertical bedrock movement caused by glacial isostatic adjustment (GIA), and present-day mass changes all cause elevation changes which are part of the observed elevation difference, but do not contribute to the ice sheet mass balance. Furthermore, a potential elevation bias between the ICESat laser campaigns must be considered, since this would also be interpreted as elevation changes.

The individual ICESat tracks are not precisely repeated but can be up to several hundred metres apart. Thus, besides the previously described signals, an observed elevation difference between tracks contains a contribution from the terrain.

The fact that the ICESat measurements are not exactly repeated, complicates the methods for deriving $\frac{dH}{dt}$, since any separation between two measurements introduces a surface slope component, which can be decomposed into an along-track and a cross-track component. Several methods for deriving $\frac{dH}{dt}$ from ICESat data have previously been published (Fricker and Padman, 2006; Howat et al., 2008; Slobbe et al., 2008; Pritchard et al., 2009). We present $\frac{dH}{dt}$ results obtained by using three different methods (M1–M3). The methods have different strengths and weaknesses, which will be discussed in the following. M1–M3 are all set up to estimate $\frac{dH}{dt}$ at a 500 m along-track resolution. At track crossover locations, measurements from both tracks are used to derive the $\frac{dH}{dt}$ values. In all three approaches, we solve for both a secular trend, $\frac{dH}{dt}$ and a seasonal signal, $s(t)$. Hence, the time dependent surface elevation, $\tilde{H}(t)$, is parameterized as

$$\tilde{H}(t) = \left(\frac{dH}{dt}\right) t + s(t), \tag{1}$$

where the seasonal signal is given by:

$$s(t) = D\cos\left(\frac{2\pi}{T}t + \phi\right) = \alpha\cos(\omega t) + \beta\sin(\omega t), \tag{2}$$

with amplitude $D = \sqrt{\alpha^2 + \beta^2}$, period T (365 days), and phase ϕ.

Each of the $\frac{dH}{dt}$ estimates from the three methods are associated with a variance from the regression procedure applied. We do not perform a full analytical error propagation through the $\frac{dH}{dt}$ calculation. We assume that the segment size of 500 m is small enough so that the error on the measurements (and on the DEM in M1) can be assumed constant within each segment and the variances are estimated from the regression analysis. Hence, the variances reflect both the measurement error and the goodness of the fit.

3.1 Method 1

A Digital Elevation Model (DEM) can be used to correct for the surface slope and this approach is used in the first method (M1). Unfortunately there are no independent, sufficiently accurate high resolution DEMs available which cover the entire GrIS. Following Slobbe et al. (2008), we choose the DEM generated from the first seven campaigns of ICESat data (DiMarzio et al., 2007). The grid spacing of this DEM is 1 km and the elevations are given relative to the WGS84 ellipsoid.

In order to subtract the DEM from the ICESat data, the DEM is linearly interpolated to estimate the value at each data location. The height of each ICESat measurement above the reference DEM is given by:

$$\Delta H^{\mathrm{M1}} = H^{\mathrm{ICESat}} - H^{\mathrm{DEM}}, \tag{3}$$

where H^{ICESat} is translated into elevations above the WGS84 ellipsoid, to be comparable with the DEM elevations (H^{DEM}).

The measurements are categorized according to the ICESat track (i) and 500 m along-track segment denoted j. The mean of the ΔH^{M1} values of each ICESat campaign is calculated in each segment, creating time series of $\Delta\bar{H}^{\mathrm{M1}}$ values along-track.

$$\Delta\bar{H}_{ij}^{\mathrm{M1}} = \begin{pmatrix} A_{ij} \\ B_{ij} \\ \alpha_{ij} \\ \beta_{ij} \end{pmatrix} \left(\bar{t}, 1, \cos\omega t, \sin\omega t\right), \tag{4}$$

where $A_{ij} = \left(\frac{dH}{dt}\right)_{ij}$, B_{ij} is the offset between the DEM and the ICESat elevations in the segment, and $\bar{t}$ is the mean time of a campaign in a given segment. The governing equation, Eq. (4) is solved using ordinary least squares regression.

Only the long wavelength component of the terrain slope is removed, due to the relative low resolution of the DEM, compared to the spacing of the ICESat along-track measurements. The 1 km resolution is too low to capture the true topography in some areas and this will most likely be reflected in the elevation changes calculated using this method. Furthermore, since the DEM used here is based on the first seven ICESat campaigns, the reference epoch will not be the same in each segment.

3.2 Method 2

In the second method (M2), data from two ICESat campaigns are used to create a reference surface, which is assumed to represent the topography in each segment. The reference surface is represented by a centroid point (x_0, y_0, H_0) and slopes

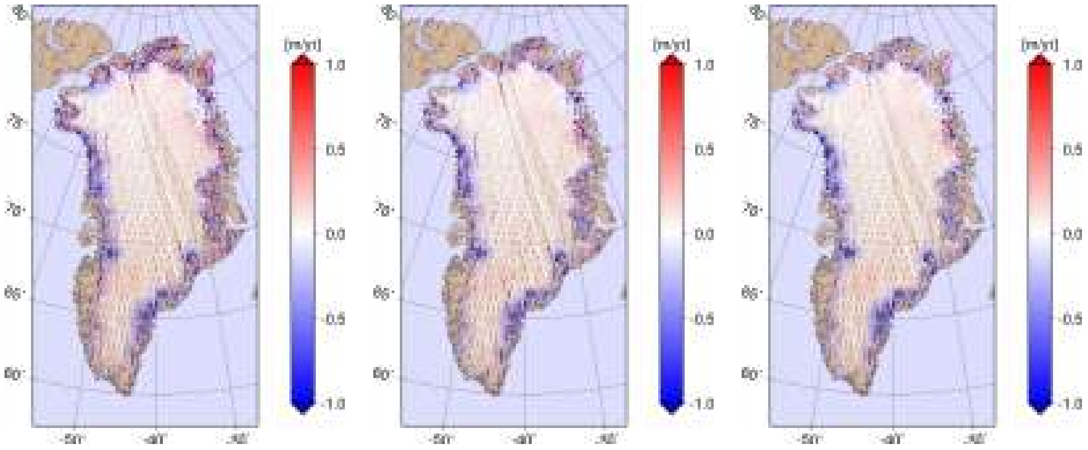

(a) (b) (c)

Fig. 1. Elevation changes derived from ICESat data using the three different methods. **(a)** M1, **(b)** M2 and **(c)** M3.

$\left(\frac{dH}{dx},\frac{dH}{dy}\right)$ and it is found by a least squares fit of these surface parameters to the measurements from two campaigns. The choice of the two campaigns, which are used to generate the reference surface, is based on two criteria. The first criterion is that the two campaigns are separated by one year in time. This ensures that both the seasonal signal and the actual change in elevation between the two campaigns are minimized. The second criterion is that the ICESat tracks, used to generate the reference surface, are the ones that span the largest area. These criteria help to ensure that the reference surface is representative of the surface slope. Hence, this reference surface is considered the reference for all other ICESat measurements in a given along-track segment, similar to the use of a DEM in M1:

$$\Delta H^{\mathrm{M2}} = H^{\mathrm{ICESat}} - H^{\mathrm{ref}}, \tag{5}$$

The height of the reference surface at a point (x,y) is given by:

$$H_{ij}^{\mathrm{ref}} = \left(\frac{dH}{dx}\right)_{ij}(x-x_0) + \left(\frac{dH}{dy}\right)_{ij}(y-y_0) + H_0. \tag{6}$$

The approach of solving for $\frac{dH}{dt}$ is similar to Eq. (4).

In spite of the criteria used to select the ICESat campaigns from which the reference surface is generated, method M2 is sensitive to seasonal variations and actual elevation changes between the two campaigns chosen. The $\frac{dH}{dt}$ estimates will, therefore, be biased. If the surface elevation has changed significantly, due to a change in mass balance in the time between the two tracks used, this method will underestimate the $\frac{dH}{dt}$ values, since some of the elevation change signal is removed.

3.3 Method 3

The third method (M3) is similar to the one presented in Howat et al. (2008) and Smith et al. (2009). In each along-track segment, the surface elevation H^{M3} is assumed to vary linearly with position (x,y), time (t) and a sine and cosine term, describing the seasonal signal:

$$H_{ij}^{\mathrm{M3}} = \begin{pmatrix} A_{ij} \\ B_{ij} \\ \alpha_{ij} \\ \beta_{ij} \\ \left(\frac{dH}{dx}\right)_{ij} \\ \left(\frac{dH}{dy}\right)_{ij} \end{pmatrix} (t, 1, \cos\omega t, \sin\omega t, (x-x_0), (y-y_0)) \tag{7}$$

where $A_{ij} = \left(\frac{dH}{dt}\right)_{ij}$, $\left(\frac{dH}{dx}\right)$ is the along-track slope, $\left(\frac{dH}{dy}\right)$ is the cross-track slope, and B_{ij} is an estimate of the topography underlying the elevation changes. (x_0,y_0) is the centroid point of the area spanned by all the measurements in the track segment. In each segment, a least squares linear regression is performed to estimate all these parameters.

This method is sensitive to the track constellation in a segment. If the change in time $\left(\frac{dH}{dt}\right)$ is strongly correlated with the change in position (e.g. $\left(\frac{dH}{dx}\right)$), this method will not be able to separate the two components.

3.4 Elevation change results

The elevation changes obtained by the three methods show that there is good agreement between the patterns of elevation changes (see Fig. 1a–c). A distinct thinning of the ice sheet is generally found along the southeast and west coast, while a smaller but consistent thickening is found in the interior part of the ice sheet, which is in agreement with other altimetry studies (Abdalati et al., 2001; Thomas et al.,

Table 2. The total mass balance of the GrIS estimated from three different methods for deriving $\frac{dH}{dt}$, and different assumptions in the firn compaction model. The contributions to the total mass balance from above and below the ELA are specified, along with the mass balance above an altitude of 2000 m. Note that the mass balance below the ELA is unaffected by firn model processes and is, therefore, the same for with and without firn compaction correction firn assumptions.

	ICESat Volume [km^3 yr^{-1}]	Applying $\tilde{\rho}$ Total [Gt yr^{-1}]	Above ELA [Gt yr^{-1}]	Above 2000 m [Gt yr^{-1}]	Below ELA [Gt yr^{-1}]	Applying $\hat{\rho}$ Total [Gt yr^{-1}]	Above ELA [Gt yr^{-1}]	Above 2000 m [Gt yr^{-1}]
With firn correction								
M1	-231 ± 24	-233 ± 27	-101	-8	-132	-174	-30	$+7$
M2	-187 ± 21	-191 ± 23	-80	-7	-111	-141	-30	$+6$
M3	-239 ± 26	-240 ± 28	-105	-9	-136	-179	-44	$+6$
Without firn correction								
M1	-231	-268	-136	-29	-132	-192	-60	-4
M2	-187	-226	-116	-28	-111	-160	-49	-4
M3	-236	-276	-141	-30	-136	-198	-62	-5

2008, 2009; Slobbe et al., 2008; Pritchard et al., 2009). On a more local scale, the thickening of Flade Isblink (81.4° N, 15.1° W) and Storstrømmen (77.1° N, 22.6° W) are identified by all three methods.

4 Deriving volume changes

In order to estimate the total annual volume change, a smooth surface that covers the entire ice sheet is fitted through the $\frac{dH}{dt}$ estimates. The uncertainty of the total volume change is quantified using a bootstrap method.

4.1 Interpolation of volume changes

The $\frac{dH}{dt}$ estimates are interpolated onto a 5×5 km grid, using ordinary kriging. For all three method results, an exponential variogram model with a range of 50 km is used. The variogram model is based on all data and, for simplicity, it is assumed to be isotropic, see Supplement. The range and the choice of model are based on the experimental variogram. Due to the large number of $\frac{dH}{dt}$ estimates, only a local subset of points is used in the kriging procedure. Cross-validation analysis is applied to determine the sufficient number of the closest points to be used in the interpolation. In order to pass on the variances from the regression analysis, these are added to the variogram model (Pebesma, 1996). The R package gstat is used for the kriging procedure (Pebesma, 2004).

The estimated volume changes are summarised in Table 2. The estimates are of little significance without knowing their associated uncertainties. It is often difficult analytically to keep track of the error when different calculations have been performed on data and, therefore, a bootstrap method (Davison and Hinkley, 2006) is used here to quantify the uncertainty.

4.2 Bootstrapping

In the bootstrap method, data is repeatedly re-sampled to create numerous artificial datasets (Davison and Hinkley, 2006). The original dataset consists of m tracks of $\frac{dH}{dt}$ estimates. For each method, 1000 new bootstrapped datasets are created by randomly drawing m tracks with replacements from the tracks in the original dataset. Hence, the bootstrapped dataset will most likely contain multiple copies of some of the original tracks. Each bootstrapped dataset contains the same number of tracks as the original dataset. From each of these bootstrapped datasets a new estimate of the volume change is calculated in the same way as for the original dataset. Finally, the standard deviation of these 1000 bootstrapped volume estimates is used as an estimate of the standard deviation of the original volume change estimate (in a frequentist sense).

4.3 Volume change results

The 1000 bootstrap re-samples make up the distributions of the volume changes. For all methods, these distributions are approximately Gaussian and centred around the volume change estimate based on the original dataset (see Fig. 2). Hence, the 95% confidence interval of the volume change will be $\pm 2\sigma$, where σ is the standard deviation. The error estimates of the volume changes are summarized in Table 2.

There is a relatively large spread in the resulting volume changes. We believe that the volume estimate found from M2 of -187 ± 21 km^3 yr^{-1} is probably an under-estimation. It is likely that the reference surface, which is created in M2, contains an actual elevation change and this will result in biased $\frac{dH}{dt}$ values. The volume change results from methods

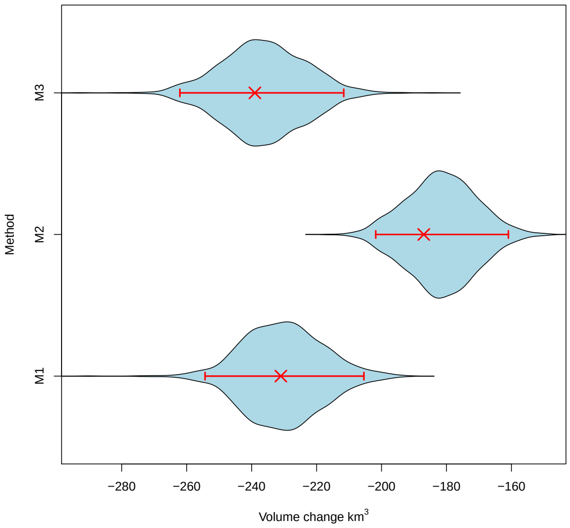

Fig. 2. Violin plot of the three method results. The blue area indicates the distribution of 1000 bootstrap samples. The red crosses are the volume estimates based on the original datasets and the red bars indicate the 95% confidence interval.

M1 and M3 are similar, with volume change estimates of $-231\pm24\,\mathrm{km^3\,yr^{-1}}$ and $-239\pm26\,\mathrm{km^3\,yr^{-1}}$, respectively.

5 Volume to mass conversion

In order to convert the derived elevation changes for the GrIS to mass change, the involved physical processes have to be known. Generally, the change in surface elevation can be written as

$$\frac{dH}{dt}=\frac{\dot{b}}{\rho}+w_\mathrm{c}+w_\mathrm{ice}+\frac{\dot{b}_\mathrm{m}}{\rho}+w_\mathrm{br}-u_\mathrm{s}\frac{dS}{dx}-u_\mathrm{b}\frac{dB}{dx}, \qquad (8)$$

where $\dot{b}$ is the surface mass balance, ρ is the density of the snow or ice and w_c is the vertical velocity of the surface due to change in firn compaction, in the following referred to as the firn compaction velocity. w_ice is the vertical velocity of the ice matrix, $\dot{b}_\mathrm{m}$ is the basal mass balance, w_br is the vertical velocity of the underlying bedrock associated with glacio-isostatic adjustment, u_s is the horizontal ice velocity of the surface, S and u_b is the horizontal velocity of the ice at the bed B (Paterson, 2002; Zwally and Li, 2002; Helsen et al., 2008; Zwally et al., 2011). A Cartesian coordinate system with a vertical axis pointing upwards is used, and we define accumulation positive and ablation negative.

As seen from Eq. (8), firn compaction and surface densities must be taken into account in order to convert the ICESat volume change to mass change. The firn responds to changes in surface temperature and precipitation and this response will not contribute to the mass balance. The firn response, the intercampaign bias and the glacio-isostatic adjustment are corrected for, before converting elevation change into mass change estimates. Based on Eq. (8), we then write the mass change as

$$\frac{dM}{dt}=\frac{dH^\mathrm{ICESat}_\mathrm{corrected}}{dt}\tilde{\rho}, \qquad (9)$$

where $H^\mathrm{ICESat}_\mathrm{corrected}$ is the elevation change from ICESat corrected for non-ice mass related processes. A distinction is made between the elevation changes caused by snow accumulation, surface melt or dynamical changes. Therefore, the density $\tilde{\rho}$ value is chosen based on the physical process involved in the mass change (Thomas et al., 2006; Zwally et al., 2011). In the ablation zone, defined here as the area below the equilibrium line altitude (ELA), all elevation changes are assumed to be caused by either surface melt or dynamical changes. In the accumulation zone above the ELA, an elevation increase is assumed to be caused by an addition of snow/firn, while an elevation decrease is assumed to be caused by ice dynamics. Therefore, we define the density $\tilde{\rho}$ to be

$$\tilde{\rho}=\begin{cases}\rho_\mathrm{s}\ \text{, if } \frac{dH^\mathrm{ICESat}_\mathrm{corrected}}{dt}\geq 0 \text{ and H } \geq \text{ELA}\\ \rho_\mathrm{i}\ \text{, elsewhere}\end{cases}, \qquad (10)$$

where ρ_s is the surface density of firn including ice lenses, written as

$$\rho_\mathrm{s}=\frac{\rho_0}{1-\frac{r}{b}\left(1-\frac{\rho_0}{\rho_\mathrm{i}}\right)}. \qquad (11)$$

Here, r is the amount of refrozen melt water inside an annual firn layer, ρ_i is the ice density ($917\ \mathrm{kg\,m^{-3}}$) and $\rho_0=625+18.7T+0.293T^2$ is the temperature dependent density of new firn before formation of ice lenses (Reeh et al., 2005), T is in °C. The assumptions that define the applied density in the volume to mass conversion is adding to the uncertainty of the mass estimate, and this will be discussed in detail in Sect. 5.5. Comparing with other studies (e.g. Thomas et al., 2006) we also perform mass change calculations, using an alternative density $\hat{\rho}$ which replaces $\tilde{\rho}$ in Eq. (9), and which is defined as

$$\hat{\rho}=\begin{cases}\rho_\mathrm{s}\ \text{, if H } \geq \text{ELA}\\ \rho_\mathrm{i}\ \text{, elsewhere}\end{cases}. \qquad (12)$$

If $\hat{\rho}$ is applied, the elevation changes above the ELA, caused by dynamic mass losses, are not accounted for.

5.1 Firn compaction modelling

In order to estimate the effect of firn compaction on short time scales, a time-dependent densification model is needed. Following Reeh (2008), the time-dependent contribution to the elevation change from changes in firn compaction, is the sum of firn layer anomalies with respect to a steady state reference. The steady state reference is defined as the youngest layer in the firn column, which is unaffected by the inter-annual variability in the surface temperature and surface mass balance. The firn compaction velocity is then defined as

$$w_\mathrm{c} = \frac{1}{\Delta t} \sum_{t_2=0}^{t-t_0} \sum_{t_i=0}^{t-t_0-t_2} \left(\lambda(t_0+t_2, t_0+t_i) - \lambda_\mathrm{ref}(t_0+t_i)\right), \quad (13)$$

where t_0 is the time of deposition, t_2 is the time of the addition of a new surface layer, $\lambda(t_0,t)$ is the annual layer thickness at a time $t = t_0+t_i$ after deposition and λ_ref is the steady state reference. $\lambda(t_0,t)$ depends on the local mass balance and is given by

$$\lambda(t_0,t) = \begin{cases} \left(\frac{(b(t_0)-r(t_0))\rho_\mathrm{i}}{\rho_\mathrm{f}(t_0,t)} + r(t_0)\right)\tau & \text{, if } b(t_0) \geq 0 \\ b(t_0)\delta(t-t_0)\tau & \text{, if } b(t_0) < 0 \end{cases}, \quad (14)$$

where τ is a time constant which, for the present study, is one month and δ is the Kronecker delta (Reeh et al., 2005). The firn density $\rho_\mathrm{f}(t_0,t)$ can be derived from the Zwally and Li (2002) parametrization of the Herron and Langway (1980) densification model

$$\rho_\mathrm{f}(t_0,t) = \begin{cases} \rho_\mathrm{i} - (\rho_\mathrm{i} - \rho_\mathrm{s}(t_0))\exp(-ct_i) & \text{, if } \rho_\mathrm{f}(t_0,t) \leq \rho_\mathrm{c} \\ \rho_\mathrm{i} - (\rho_\mathrm{i} - \rho_\mathrm{c})\exp(-c(t_i - t_c)) & \text{, if } \rho_\mathrm{f}(t_0,t) > \rho_\mathrm{c} \end{cases} \quad (15)$$

where ρ_c is the critical firn density of 550 kg m^{-3} defined by Herron and Langway (1980), t_c is the time it takes for the firn to reach the critical density and c is the densification constant describing the linear change in air volume in the firn, caused by the overlaying pressure (Reeh, 2008). Following Arthern et al. (2010), the densification constant c is given by a Nabarro-Herring type creep:

$$c = \begin{cases} 0.07b(t)g\exp\left(-\frac{E_\mathrm{c}}{RT} + \frac{E_\mathrm{g}}{RT_\mathrm{av}}\right) & \text{for} \rho \leq \rho_\mathrm{c} \\ 0.03b(t)g\exp\left(-\frac{E_\mathrm{c}}{RT} + \frac{E_\mathrm{g}}{RT_\mathrm{av}}\right) & \text{for} \rho_\mathrm{c} < \rho \end{cases} \quad (16)$$

where g is the gravity, E_c and E_g are the activation energies (60 kJmol^{-1} and 42.4 kJmol^{-1}, respectively), and T_av is the average temperature. T is the seasonal temperature at depth z derived by surface temperature fluctuations, described by the general heat equation,

$$\rho C \frac{\partial T}{\partial t} = K\nabla^2 T - \rho C\left(u\frac{\partial T}{\partial x} + v\frac{\partial T}{\partial y}\right) + \left(\frac{dK}{dz} - \rho C w\right)\frac{\partial T}{\partial z} \quad (17)$$

where C is the specific heat capacity, K is the thermal conductivity and u,v,w are the velocities at the spatial coordinates x,y,z (Paterson, 2002). Equation (17) is solved following Schwander et al. (1997).

5.2 HIRHAM5 – forcing of the firn compaction model

The monthly mean surface temperature, runoff, snowfall and precipitation variables, that are required for the firn compaction model, are produced by the HIRHAM5 RCM (Christensen et al., 2006). The HIRHAM5 RCM is a hydrostatic RCM developed at the Danish Meteorological Institute (DMI) and is based on the HIRLAM7 dynamics (Eerola, 2006) and ECHAM5 physics (Roeckner et al., 2003). The HIRHAM5 RCM used here is an upgraded version of the HIRHAM model that has been used in several studies of accumulation and climate over Greenland. This model has been validated both with ice core data and automatic weather station data and is shown to perform well over Greenland (Dethloff et al., 2002; Kiilsholm et al., 2003; Box and Rinke, 2003; Stendel et al., 2008; Lucas-Picher, 2011). The lateral boundary condition for HIRHAM5 are taken from the European Centre for Medium Range Weather Forecast (ECMWF) ERA-Interim re-analysis (Simmons, 2007) at T255 (∼0.7° or ∼77 km), which is a comprehensive re-analysis of the state of the atmosphere, using measurements from satellites, weather balloons and ground stations. A continuous simulation with HIRHAM5 at 0.05° (∼5.55 km) resolution on a rotated grid is realised. The sea-surface temperature and sea-ice distribution, taken from ERA-Interim, are interpolated to the HIRHAM5 grid and prescribed to the model. The wind components, atmospheric temperature, specific humidity and surface pressure from ERA-Interim are transmitted to HIRHAM5 every six hours for each atmospheric model level of the HIRHAM5 RCM. At the lateral boundaries of the model domain, a relaxation scheme according to Davies (1976) is applied with a buffer zone of ten grid cells. The high 5.5 km horizontal resolution data are appropriate to determine the precipitation distribution over the sharp edge of the ice sheet, prominent in the ablation zone.

A comparison of the publicly available 1.5° × 1.5° ERA-Interim dataset and the output from the HIRHAM5 of 0.05°, that has been forced with the same dataset, is shown in Fig. 3. It is clear that the high resolution HIRHAM5 RCM output captures the complex coastal topography of Greenland, which the low resolution forcing field cannot. The high resolution precipitation pattern impacts on the area above the ELA, where the firn compaction correction is applied and, therefore, the benefit of the high resolution forcing field is clear (see Fig. 3).

5.3 Interpolated metric grid

In order to derive the mass change of the GrIS, the area of each grid cell must be known. To ensure the equal area of each grid box, the high resolution data from the HIRHAM5 RCM is interpolated onto the equal distance 5 × 5 km grid by a nearest neighbour interpolation. The snowfall of 2008 in two different map projections is shown in Fig. 3. The interpolation onto an equal distance grid preserves the pattern of snowfall, but introduces a latitude dependent noise which is, however, only significant over the northernmost part of Greenland (e.g., at Station Nord). Despite this noise, the interpolation of the HIRHAM5 climate output on an equal-distance grid provides a good representation of the fields and it is used here to force the surface density and firn compaction models.

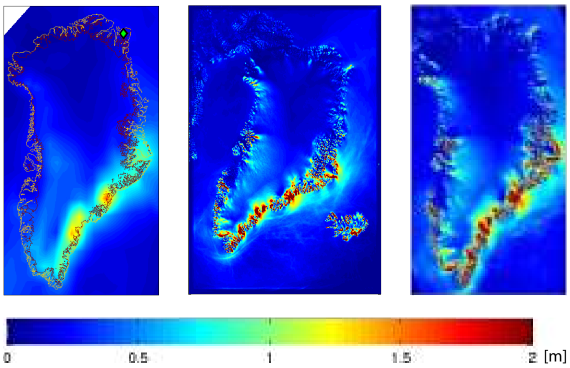

Fig. 3. The 2008 snowfall on a scale at 0 to 2 m of water equivalent (from blue to red). (Left) Precipitation field from the ERA-Interim re-analysis, linearly interpolated from the 1.5° × 1.5° resolution onto an equal distance 5 km × 5 km grid. The Greenland coastline is marked in yellow, the ice boundary in red and the green diamond marks the location of Station Nord. (Middle) The precipitation field from the HIRHAM5 RCM on its original map projection, with a grid spacing of 0.05° × 0.05°. This projection gives a metric resolution of ~5.5 km × 5.5 km. (Right) Nearest neighbour interpolation of the precipitation field from the HIRHAM5 RCM onto an equal distance 5 km × 5 km grid. The highly dynamic behaviour of the precipitation from the HIRHAM5 model is preserved in the transformation of the map projections.

5.4 Refreezing of melt water and formation of ice lenses

On the GrIS, 60% of the run-off given by the HIRHAM5 RCM is assumed to refreeze in the snowpack (Reeh, 1991). The accumulation is calculated as the sum of snowfall and the refrozen run-off. To simplify the following derivation of a time dependent densification model, the refrozen run-off is assumed to refreeze inside the firn layer, from which it originates, and the water is not allowed to penetrate deeper into the firn column. This assumption is a simplification. Observations from the Arctic snowpack show that melt water often penetrates through the snowpack until it reaches a hard layer, where it flows along until it refreezes or finds a crack to propagate downwards into the deeper firn (Benson, 1962; Bøggild, 2000). In order to model this behaviour (Jansson et al., 2003), the percolation depth has to be accounted for and knowledge of grain growth in water-saturated firn is required. Development of such models is outside the scope of the present study of firn compaction, where the overburden pressure is believed to be the driving force, despite the fact that melt water percolation may redistribute the load on a layer.

5.5 Results of firn compaction and density modelling

The monthly firn layer thickness is computed from Eq. (14), using the output from the HIRHAM5 RCM as forcing. To derive the firn compaction velocity (Eq. 13), a steady state reference (λ_{ref}) must be defined. The time span of the climate record is too short to define a robust steady state reference for the firn compaction model. Moreover, the inter-annual variation in temperature and precipitation will bias a chosen reference to the climate pattern which is dominating in the time span of the reference period. To avoid defining a steady state reference layer thickness, the thickness of the top firn layers is compared over the period from 2003 to 2008. The maximum number of layers, that can be evaluated at the beginning of 2003 is 169. Hence, the thickness of the top 169 layers is compared from month to month during the period 2003 to 2008 at each grid point above the ELA. The change in thickness is shown in Fig. 4a, along with the error in the linear fit in Fig. 4d. The change in the thickness of the 169 layers is a combination of changes in accumulation/surface melt and changes in the firn compaction. The change in accumulation, given in ice equivalent, for the top 169 layer thickness, is shown in Fig. 4b. By subtracting the change in the thickness of the 169 layers, in ice equivalent, from the 169 layer firn thickness, the change in air volume of the top firn is found. The rate of change in this air volume in the firn, is equivalent to the firn compaction velocity defined in Eq. (13). The approach of evaluating the relative change in air volume in each grid point above the ELA, avoids the definition of a steady state reference for the firn compaction. The resulting firn compaction velocity is the linear trend in air volume of the top 169 layers for the period from 2003 to 2008 (Fig. 4c). Figure 4c shows how the firn compaction velocity is mainly increasing in the central area of the GrIS, whereas it is decreasing in the coastal areas. This pattern shows the importance of taking the firn compaction into account, when converting the ICESat derived volume change to a change in the total mass balance of the GrIS. Depending on the assumed density of the volume changes, the firn correction corresponds to a mass loss of 18 or 36 Gt yr^{-1}. This corresponds to a reduction of up to 13% in the mass loss estimates when compared to the estimate from the ICESat measurements, without applying any firn compaction correction.

It is difficult to quantify the error in the firn compaction model. Further studies have to be carried out in which the modelled firn densities are compared with in situ measurements, in order to determine the error in the firn compaction velocity. The error estimate of the firn compaction correction is found here from the error in the linear fit of the inter-annual variability of the firn column. The 95% confidence interval is shown in the lower panel of Fig. 4. The error associated with the firn compaction velocity is most pronounced in the coastal areas near large outlet glaciers, where the forcing field from HIRHAM5 shows the largest variability. The error in the fitted firn compaction velocities will result in an error in the estimate of the total mass loss of the GrIS. The error shown in Fig. 4f is summed over each of the 5 × 5 km grid cells above the ELA, to estimate the resulting volume error. This volume is then converted into mass, using

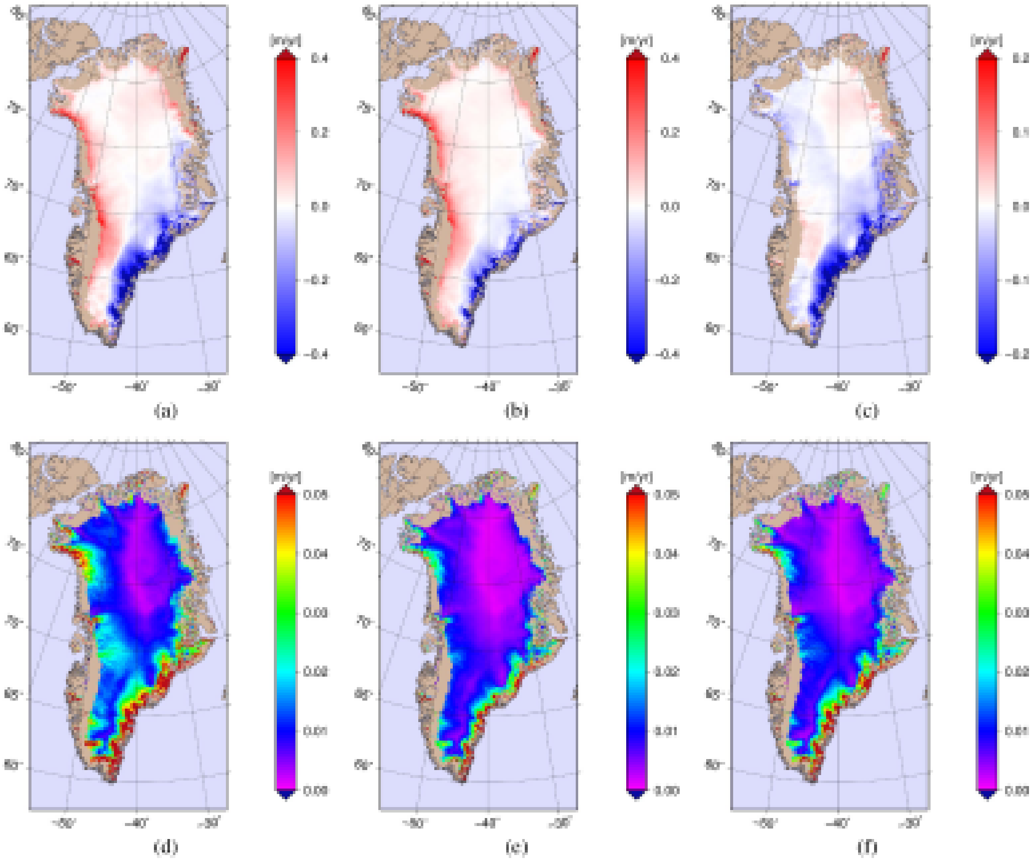

Fig. 4. The different contributions to the firn compaction model for the period from 2003 to 2008, forced by the HIRHAM5 RCM temperature and precipitation fields. Only the area above the ELA is shown in the figures. The upper panels show the modelled firn process, estimated from a linear fit for the period 2003 to 2008. **(a)** The modelled change in the thickness of the top 169 monthly firn layers. **(b)** The change of ice equivalent thickness of the top 169 monthly firn layers. **(c)** The change in air volume in the top firn, which is equivalent to the firn compaction velocity defined in Eq. (13). The work flow of the computations is **(c)** = **(a)** − **(b)**. **(d)**, **(e)** and **(f)** show the 95% confidence interval of the linear trend in **(a)**, **(b)** and **(c)**, respectively.

the surface density model, and the result is firn compaction induced errors between 7–15 $\mathrm{Gt\,yr^{-1}}$, depending on which ice or firn density is assumed. With the possible underestimation of the firn compaction, caused by only deriving the change in compaction of the top 169 layers, the higher error estimate is probably the more realistic.

The surface density $\bar{\rho}$, as defined by Eq. (10), takes both changes into account due to ice dynamics and surface mass balance, based on a simplified assumption of the processes causing the elevation changes. Any elevation increase, above the ELA, is assumed to be caused by surface mass imbalance, while an elevation decrease is assumed to be caused by ice dynamics. Using this assumption, two processes are neglected: basal melting and the possibility that an elevation increase is caused by ice dynamics. A maximum basal melt rate of 15–20 $\mathrm{mm\,yr^{-1}}$ has been reported by Fahnestock et al. (2001) and Buchardt and Dahl-Jensen (2007). Assuming a more realistic basal melt rate of 1 $\mathrm{mm\,yr^{-1}}$ everywhere above the ELA, the error of neglecting basal melt corresponds to 0.9 $\mathrm{Gt\,yr^{-1}}$. Acceleration of outlet glaciers is known to cause thinning of the ice sheet further inland, and conversely, a slow down of outlet glaciers could result in a build up of ice further inland. The assumptions neglect the latter possibility above the ELA. This is reasonable, because the GrIS is generally experiencing retreat and acceleration along the margins (Abdalati et al., 2001), and any changes would be most significant below the ELA. If all elevation increases above the ELA are assumed to be caused by ice instead of firn, the corresponding error is 37 $\mathrm{Gt\,yr^{-1}}$. An elevation increase caused by pure ice is, however, unlikely. The Parallel Ice Sheet Model (Bueler and Brown, 2009; Aschwanden and Khroulev, 2009) has been used to identify regions where thickening caused by ice dynamics can occur, which reduces the error of neglecting build up of ice inland to 14 Gt yr^{-1}.

6 Additional elevation change corrections

The elevation changes observed by ICESat include signals from processes which do not contribute to the mass balance of the GrIS. The most significant contribution is the firn compaction, but it is also necessary to correct for GIA, elastic uplift caused by the present-day mass changes and the ICESat intercampaign elevation biases.

6.1 Vertical bedrock movement

Elevation changes which are not related to ice volume changes are also detected by ICESat, and the estimated $\frac{dH}{dt}$ values must be corrected for these changes in order to determine the mass balance of the ice sheet. A bedrock movement (w_{br}), caused by GIA and elastic uplift from present-day mass changes, is part of the elevation changes observed by ICESat.

The GIA contribution, according to Peltier (2004), is used. It is based on the ice history model ICE-5G and the VM2 Earth model (http://pmip2.lsce.ipsl.fr/design/ice5g/). The rate of vertical motion caused by GIA is subtracted from the ICESat $\frac{dH}{dt}$ estimates. This correction contributes to the mass balance of the GrIS with an amount of approximately 1 Gt yr^{-1}.

The present-day ice sheet mass changes cause an elastic response of the bedrock (e.g., Khan et al., 2010). These vertical displacements are estimated by solving the Sea Level Equation, the fundamental equation that governs the sea level changes associated with glacial isostatic adjustment (Farrell and Clark, 1976). Since the time scale of the mass changes considered here is extremely short compared to the Maxwell relaxation time of the mantle (Spada et al., 2010), any viscoelastic effect is neglected and the ice thickness variations deduced by ICESat are spatially convolved with purely elastic loading "h" Love numbers. Sea level variations associated with melting are computed first, taking into account the elastic response of the Earth and the gravitational interaction between the ice sheets, the oceans and the mantle. Then, vertical displacements are retrieved by the surface load history over the entire surface of the Earth, associated with ice thickness variations and sea level changes. The result in Fig. 5 is obtained from a suitably modified version of the code SELEN 2.9 (Spada and Stocchi, 2007), which solves the Sea Level Equation iteratively, essentially following a variant of the pseudo-spectral method introduced by Mitrovica and Peltier (1991). A maximum harmonic degree $l_{\max} = 128$ is used here. Vertical displacement is computed in the reference frame with the origin in the centre of mass of the system (Earth + Load), and includes the harmonic component of degree one (Greff-Lefftz and Legros, 1997). The elastic uplift correction correspond to -4 to -2 Gt yr^{-1}, dependent on the mass loss. The elastic vertical displacement based on the results from method M3 (Sect. 3.3) is shown in Fig. 5.

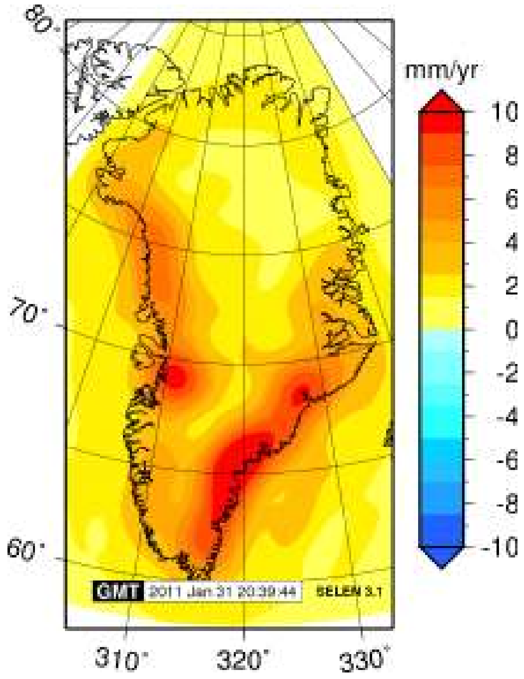

Fig. 5. Rate of elastic vertical displacement, caused by present-day mass changes in Greenland, referred to the period of one year, computed according to mass changes obtained by M3.

6.2 ICESat intercampaign bias correction

It has been documented that there are elevation biases between the different ICESat laser campaigns. Following the method described in Gunter et al. (2009), the trend in the ICESat intercampaign bias is estimated by O. B. Andersen and T. Bondo (personal communication, 2010). The GLA15 release 31 ocean altimetry elevations are compared to a mean sea surface topography model (DNSC08). The trend is found to be 1.29 ± 0.4 cm yr^{-1}, when corrected for an assumed actual sea level rise of 0.3 cm yr^{-1} (Leuliette et al., 2004). This trend in intercampaign biases contributes with approximately 14 ± 0.4 Gt yr^{-1} to the mass balance.

7 Mass balance of the GrIS

Determining the mass change of the GrIS is a complex problem and the result depends on the type of observation and on the level of complexity of the volume to mass conversion. This may explain differences in the estimates of the total

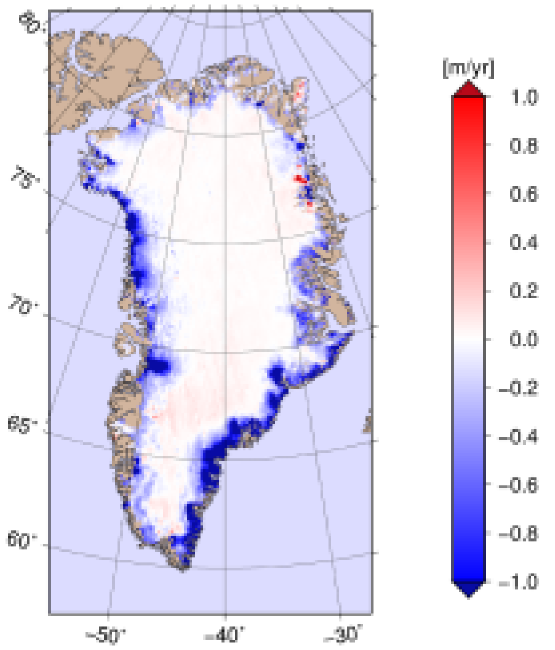

Fig. 6. The spatial distribution of the mass change of the GrIS, given in metres of ice equivalent. The result is based on the estimate derived by M3. The pattern of coastal thinning seen in Fig. 1 is also found in the mass change of the GrIS.

mass balance of the GrIS, which appear in the literature. To summarise the results of this study, the total mass balance estimates of the GrIS, are listed in Table 2. We have chosen to derive the mass change both with and without applying the firn compaction correction, to highlight the importance of this correction. The second key assumption of the mass loss derivation is the density $\tilde{\rho}$, from which the volume change is related to mass. The assumption, that an elevation decrease above the ELA is caused by a loss of glacial ice somewhere in the ablation area due to ice dynamics, increases the estimated mass loss of the GrIS. The total mass balances estimates (Table 2) are derived both with $\tilde{\rho}$ and $\hat{\rho}$.

The total error of the mass balance estimate, $\delta_{\frac{dM}{dt}}$, is a function of the many different contributing components to the mass balance calculation. The error of the combined volume to mass conversion is given by the following contributors. (1) The error of the ICESat derived volume change given by the bootstrap method. The methodology of volume error determination, has also been applied on the mass change estimate, resulting in an estimated error, δ_{ICESat}, of 18–23 Gt yr^{-1}. (2) The error of change in firn compaction, δ_{Firn}. (3) The error of bedrock movement, δ_{br}. (4) The error of the intercampaign bias correction, $\delta_{\mathrm{IntCamp}}$. (5) The error from neglecting basal melt in areas of corrected elevation increase, δ_{Melt}. (6) Error of the neglecting ice build up above the ELA, $\delta_{\mathrm{ELABuildUp}}$. If the errors are assumed to be independent, the sum of errors is written

$$\delta_{\frac{dM}{dt}} = \sqrt{\delta^2_{\mathrm{ICESat}} + \delta^2_{\mathrm{Firn}} + \delta^2_{\mathrm{br}} + \delta^2_{\mathrm{IntCamp}} + \delta^2_{\mathrm{Melt}} + \delta^2_{\mathrm{ELABuildup}}} \quad (18)$$

Our estimates of the total mass balance of the GrIS are in the range -191 ± 23 to -240 ± 28 Gt yr^{-1}, based on the comprehensive error analysis of the ICESat derive volume changes and the theoretical treatment of the surface density and firn compaction modelling. The spatial distribution of the mass balance is seen in Fig. 6. The total mass loss, based on M3, is equivalent to a global sea level rise of 0.66 ± 0.08 mm yr^{-1}.

The mass loss of the major outlet glaciers is evident in Fig. 6 and the interior part of the GrIS shows little changes over the period. West of the South Greenland ice divide, the ice sheet is gaining mass, which may be caused by an increase in precipitation (cf. Fig. 4c). The most prominent area of mass increase is found in the upper area of the Storstrømmen (Bøggild et al., 1994) outlet glacier in Northeast Greenland. The ice sheet drainage basin ending in Storstrømmen is believed to originate in the central part of the GrIS near the summit area (Rignot and Kanagaratnam, 2006). Therefore, changes in Storstrømmen glacier may be caused by effects inland, or the dynamical response of the GrIS due to changes in climate. However, this has to be verified by additional studies of this area.

8 Discussion and conclusions

Using three different methods to derive elevation changes of the GrIS from ICESat data during the period October 2003–March 2008 reveals a consistent picture of massive ice thinning along the margin of the GrIS and a smaller elevation increase in the interior parts. The thinning is most evident along the southeast and the west coasts. An interpolation and bootstrap approach is applied, to derive a total annual volume change of snow/ice together with the corresponding uncertainties for all three methods. Volume changes of -231 ± 24 km^3 yr^{-1}, -187 ± 21 km^3 yr^{-1} and -239 ± 26 km^3 yr^{-1} are computed, depending on the method used. The difference in volumes obtained, confirms that mass balance studies from satellite altimetry are sensitive to the approach chosen for deriving elevation changes. From this analysis it is concluded that the volume estimate based on M2 probably is an underestimation of the volume change. Method M1 and M3 results in similar volume change estimates. Based on the uncertainty estimate alone, it is not possible to conclude which method performs the best.

In order to correct the observed elevation changes for processes not contributing to the ice sheet mass balance, we have estimated the change in firn compaction, the vertical bedrock movement caused by GIA and elastic uplift and the trend in the ICESat intercampaign elevation bias.

The largest elevation change correction, corresponding to $36 \pm 7\,\mathrm{Gt\,yr^{-1}}$ is the firn compaction correction. The trend in the ICESat intercampaign bias is found to be $-1.29 \pm 0.4\,\mathrm{cm\,yr^{-1}}$ which corresponds to a mass gain of approximately $14 \pm 0.4\,\mathrm{Gt\,yr^{-1}}$. The elastic uplift of the bedrock, caused by the present-day mass changes are found to contribute with -4 to $-2\,\mathrm{Gt\,yr^{-1}}$ to the total mass balance and the GIA correction is $1\,\mathrm{Gt\,yr^{-1}}$.

The firn compaction model, besides its application shown here, can also be used to validate the RCM forcing by comparing the modelled density of the firn with in situ observations from the GrIS. However, a model comparison study for the GrIS is not within the scope of the presented work, but might be elaborated on in the future.

Modelled surface densities are used to convert the volume change into mass balance. Based on the different methods, for deriving elevation changes, we obtain mass balance estimates of the GrIS for 2003–2008 of $-233 \pm 27\,\mathrm{Gt\,yr^{-1}}$, $-191 \pm 23\,\mathrm{Gt\,yr^{-1}}$ and $-240 \pm 28\,\mathrm{Gt\,yr^{-1}}$, respectively.

These mass balance estimates, are in good agreement with results obtained by others. Based on GRACE data, Velicogna (2009) has estimated the mass loss to be $230 \pm 33\,\mathrm{Gt\,yr^{-1}}$ during the period 2002–2009, and Wouters et al. (2008) find a mass loss of $179 \pm 25\,\mathrm{Gt\,yr^{-1}}$ for the years 2003–2008. van den Broeke et al. (2009) find a total mass balance of $-237 \pm 20\,\mathrm{Gt\,yr^{-1}}$ for 2003–2008, from modelled surface mass balance and observed discharge. Finally, all mass balance results presented here, are large compared to the ICESat derived mass loss of $139 \pm 68\,\mathrm{Gt\,yr^{-1}}$ found by Slobbe et al. (2009), based on data from 2003 to 2007, and that does not take into account firn compaction, elastic uplift and intercampaign bias corrections.

Supplementary material related to this article is available online at: http://www.the-cryosphere.net/5/173/2011/tc-5-173-2011-supplement.zip.

Acknowledgements. We acknowledge the Danish National Research Foundation for funding the CIC. This work was supported by funding to the ice2sea programme from the European Union 7th Framework Programme, grant number 226375 (ice2sea contribution number 014). Code SELEN is available from GS or it can be downloaded from http://www.fis.uniurb.it/spada/SELEN_minipage.html. Part of this work was supported by COST Action ES0701 "Improved constraints on models of Glacial Isostatic Adjustment". ECMWF ERA-interim data have been provided by ECMWF from the ECMWF Data Server. ICESat data was downloaded from the NSIDC web site. We thank the two anonymous reviewers for many constructive comments.

Edited by: M. Van den Broeke

References

Abdalati, W., Krabill, W., Frederick, E., Manizade, S., Martin, C., Sonntag, J., Swift, R., Thomas, R., Wright, W., and Yungel, J.: Outlet glacier and margin elevation changes: near-coastal thinning of the Greenland ice sheet, J. Geophys. Res., 106, 33729–33741, doi:10.1029/2001JD900192, 2001.

Abshire, J. B., Sun, X., Riris, H., Sirota, J. M., McGarry, J. F., Palm, S., Yi, D., and Liiva, P.: Geoscience Laser Altimeter System (GLAS) on the ICESat mission: on-orbit measurement performance, Geophys. Res. Lett., 32, L21S02, doi:10.1029/2005GL024028, 2005.

Arthern, R. J., Vaughan, D. G., Rankin, A. M., Mulvaney, R., and Thomas, E. R.: In situ measurements of Antarctic snow compaction compared with predictions of models, J. Geophys. Res., 115, F03011, doi:10.1029/2009JF001306, 2010.

Aschwanden, A. and Khroulev, C.: SeaRISE Greenland: On "spin-up" procedures using InSAR surface velocities, AGU Fall Meeting Abstracts, 2009.

Benson, C. S.: Stratigraphic Studies in the Snow and Firn of the Greenland Ice Sheet, Tech. Rep. 70, SIPRE (Snow Ice and Permafrost Research Establishment) Research Report, US army corps of engineers, Hanover, New Hampshire, 1962.

Bøggild, C. E.: Preferential flow and melt water retention in cold snow packs in West-Greenland, Nord. Hydrol., 31, 287–300, 2000.

Bøggild, C. E., Reeh, N., and Oerter, H.: Modelling ablation and mass-balance sensitivity to climate change of Storstrømmen, Northeast Greenland, Global Planet. Change, 9, 79–90, doi:10.1016/0921-8181(94)90009-4, 1994.

Box, J. E. and Rinke, A.: Evaluation of Greenland Ice Sheet Surface Climate in the HIRHAM Regional Climate Model Using Automatic Weather Station Data, J. Climate, 16, 1302–1319, http://journals.ametsoc.org/doi/abs/10.1175/1520-0442%282003%2916%3C1302%3AEOGISS%3E2.0.CO%3B2, 2003.

Buchardt, S. L. and Dahl-Jensen, D.: Estimating the basal melt rate at NorthGRIP using a Monte Carlotechnique, Ann. Glaciol., 45, 137–142, 2007.

Bueler, E. and Brown, J.: Shallow shelf approximation as a sliding law in a thermomechanically coupled ice sheet model, J. Geophys. Res., 114, F03008, doi:10.1029/2008JF001179, 2009.

Christensen, O. B., Drews, M., Christensen, J., Dethloff, K., Ketelsen, K., Hebestadt, I., and Rinke, A.: The HIRHAM regional climate model. Version 5, Tech. Rep. 06-17, DMI technical report, Cambridge University Press, Cambridge, available at: http://www.dmi.dk/dmi/tr06-17.pdf, 2006.

Csatho, B. M., Schenk, A. F., van der Veen, C. J., and Krabill, W. B.: Reconstruction of Greenland Ice Sheet Changes from Laser Altimetry Measurements, AGU Fall Meeting Abstracts, http://websrv.cs.umt.edu/isis/index.php/Present_Day_Greenland, 2009.

Davies, H. C.: A laterul boundary formulation for multi-level prediction models, Q. J. Roy. Meteor. Soc., 102, 405–418, doi:10.1002/qj.49710243210, 1976.

Davison, A. C. and Hinkley, D.: Bootstrap Methods and their Application, 8th edn., Cambridge Series in Statistical and Probabilistic Mathematics, Meteorological Institute, University of Bonn, Bonn, 2006.

Dethloff, K., Schwager, M., Christensen, J. H., Kiilsholm, S., Rinke, A., Dorn, W., Jung-Rothenhäusler, F., Fischer, H., Kipfstuhl, S., and Miller, H.: Recent Greenland Accumulation

Estimated from Regional Climate Model Simulations and Ice Core Analysis, J. Climate, 15, 2821–2832, doi:10.1175/1520-0442(2002)015<2821:RGAEFR>2.0.CO;2, 2002.

DiMarzio, J., Brenner, A., Schutz, R., Shuman, C., and Zwally, H.: GLAS/ICESat 1 km laser altimetry digital elevation model of Greenland, Digital media, National Snow and Ice Data Center, Boulder, CO, 2007.

Eerola, K.: About the performance of HIRLAM version 7.0, Tech. Rep. 51, Article 14, HIRLAM Newsletter, Danish Meteorological Institute, Copenhagen, available at: http://hirlam.org/, 2006.

Fahnestock, M., Abdalati, W., Joughin, I., Brozena, J., and Gogineni, P.: High Geothermal Heat Flow, Basal Melt, and the Origin of Rapid Ice Flow in Central Greenland, Science, 294, 2338–2342, doi:10.1126/science.1065370, 2001.

Farrell, W. E. and Clark, J. A.: On postglacial sea level, Geophys. J. Roy. Astr. S., 46, 647–667, doi:10.1111/j.1365-246X.1976.tb01252.x, 1976.

Fricker, H. A. and Padman, L.: Ice shelf grounding zone structure from ICESat laser altimetry, Geophys. Res. Lett., 33, L15502, doi:10.1029/2006GL026907, 2006.

Fricker, H. A., Borsa, A., Minster, B., Carabajal, C., Quinn, K., and Bills, B.: Assessment of ICESat performance at the salar de Uyuni, Bolivia, Geophys. Res. Lett., 32, L21S06, doi:10.1029/2005GL023423, 2005.

Greff-Lefftz, M. and Legros, H.: Some remarks about the degree one deformations of the Earth, Geophys. J. Int., 131, 699–723, doi:10.1111/j.1365-246X.1997.tb06607.x, 1997.

Gunter, B., Urban, T., Riva, R., Helsen, M., Harpold, R., Poole, S., Nagel, P., Schutz, B., and Tapley, B.: A comparison of coincident GRACE and ICESat data over Antarctica, J. Geodesy, 83, 1051–1060, doi:10.1007/s00190-009-0323-4, 2009.

Helsen, M. M., van den Broeke, M. R., van de Wal, R. S. W., van de Berg, W. J., van Meijgaard, E., Davis, C. H., Li, Y., and Goodwin, I.: Elevation changes in Antarctica mainly determined by accumulation variability, Science, 320, 1626–1629, doi:10.1126/science.1153894, 2008.

Herron, M. and Langway, C.: Firn densification: an empirical model, J. Glaciol., 25, 373–385, 1980.

Howat, I. M., Smith, B. E., Joughin, I., and Scambos, T. A.: Rates of Southeast Greenland ice volume loss from combined ICESat and ASTER observations, Geophys. Res. Lett., 35, L17505, doi:10.1029/2008GL034496, 2008.

Jansson, P., Hock, R., and Schneider, T.: The concept of glacier storage: a review, J. Hydrol., 282, 116–129, doi:10.1016/S0022-1694(03)00258-0, 2003.

Joughin, I., Smith, B. E., Howat, I. M., Scambos, T., and Moon, T.: Greenland flow variability from ice-sheet-wide velocity mapping, J. Glaciol., 56(16), 415–430, doi:10.3189/002214310792447734, 2010.

Khan, S. A., Wahr, J., Bevis, M., Velicogna, I., and Kendrick, E.: Spread of ice mass loss into Northwest Greenland observed by GRACE and GPS, Geophys. Res. Lett., 37, L06501, doi:10.1029/2010GL042460, 2010.

Kiilsholm, S., Christensen, J. H., Dethloff, K., and Rinke, A.: Net accumulation of the Greenland ice sheet: High resolution modeling of climate changes, Geophys. Res. Lett., 30, 1485, doi:10.1029/2002GL015742, 2003.

Leuliette, E. W., Nerem, R. S., and Mitchum, G. T.: Calibration of TOPEX/Poseidon and Jason altimeter data to construct a continuous record of mean sea level changes, Mar. Geod., 27, 79–94, doi:10.1080/01490410490465193, 2004.

Li, J., Zwally, H. J., and Comiso, J. C.: Ice-sheet elevation changes caused by variations of the firn compaction rate induced by satellite-observed temperature variations (1982–2003), Ann. Glaciol., 46, 8–13, doi:10.3189/172756407782871486, 2007.

Lucas-Picher, P.: Very high-resolution regional climate modeling over Greenland with HIRHAM5, in preparation, 2011.

Luthcke, S. B., Zwally, H. J., Abdalati, W., Rowlands, D. D., Ray, R. D., Nerem, R. S., Lemoine, F. G., McCarthy, J. J., and Chinn, D. S.: Recent Greenland ice mass loss by drainage system from satellite gravity observations, Science, 314, 1286–1289, doi:10.1126/science.1130776, 2006.

Mitrovica, J. X. and Peltier, W. R.: On post-glacial geoid subsidence over the equatorial ocean, J. Geophys. Res., 96, 20053–20071, 1991.

NSIDC: GLAS altimetry product usage guidance, National Snow and Ice data Center, University of Colorado, Boulder, available at: http://nsidc.org/data/docs/daac/glas_altimetry/usage.html, 2010.

Paterson, W. S. B.: Physics of Glaciers, 3rd edn., Butterworth-Heinemann, 3rd edn. 1994, reprinted with corrections 1998, 2001, 2002, Oxford, 2002.

Pebesma, E. J.: Mapping groundwater quality in The Netherlands, Netherlands Geographical studies, 199, Utrecht University, Utrecht, available at: http://www.geog.uu.nl/ngs/ngs.html, 1996.

Pebesma, E. J.: Multivariable geostatistics in S: the gstat package, Comput. Geosci., 30, 683–691, doi:10.1016/j.cageo.2004.03.012, 2004.

Peltier, W.: Global glacial isostasy and the surface of the ice-age Earth: the ICE-5G (VM2) model and GRACE, Annu. Rev. Earth Pl. Sc., 32, 111–149, doi:10.1146/annurev.earth.32.082503.144359, 2004.

Pritchard, H. D., Arthern, R. J., Vaughan, D. G., and Edwards, L. A.: Extensive dynamic thinning on the margins of the Greenland and Antarctic ice sheets, Nature, 461, 971–975, doi:10.1038/nature08471, 2009.

Reeh, N.: Parameterization of melt rate and surface temperature on the Greenland ice sheet, Polarforschung 1989, 5913, 113–128, 1991.

Reeh, N.: A nonsteady-state firn-densification model for the percolation zone of a glacier, J. Geophys. Res., 113, F03023, doi:10.1029/2007JF000746, 2008.

Reeh, N., Fisher, D. A., Koerner, R. M., and Clausen, H. B.: An empirical firn-densification model comprising ice lenses, Ann. Glaciol., 42, 101–106, doi:10.3189/172756405781812871, available at: http://www.ingentaconnect.com/content/igsoc/agl/2005/00000042/00000001/art00017, 2005.

Rignot, E. and Kanagaratnam, P.: Changes in the velocity structure of the Greenland ice sheet, Science, 311, 986–990, doi:10.1126/science.1121381, 2006.

Rignot, E., Braaten, D., Gogineni, S. P., Krabill, W. B., and McConnell, J. R.: Rapid ice discharge from Southeast Greenland glaciers, Geophys. Res. Lett., 31, L10401, doi:10.1029/2004GL019474, 2004.

Roeckner, E., Bauml, G., Bonaventura, L., Brokopf, R., Esch, M., Giorgetta, M., Hagemann, S., Kirchner, I., Kornblueh, L., Manzini, E., Rhodin, A., Schlese, U., Schulzweida, U., and

Tompkins, A.: The atmospheric general circulation model ECHAM 5. Part I: model description, Tech. Rep. 349, Max-Planck-Institute for Meteorology, Hamburg, 2003.

Schwander, J., Sowers, T., Barnola, J.-M., Blunier, T., Fuchs, A., and Malaizé, B.: Age scale of the air in the summit ice: Implication for glacial-interglacialtemperature change, J. Geophys. Res., 102, 19483–19494, doi:10.1029/97JD01309, 1997.

Simmons, A., Uppala, S., Dee, D., and Kobayashi, S.: ERA-interim: new ECMWF re-analysis products from 1989 onwards, ECMWF Newsletter, 110, 25–35, 2007.

Slobbe, D., Lindenbergh, R., and Ditmar, P.: Estimation of volume change rates of Greenland's ice sheet from ICESat data using overlapping footprints, Remote Sens. Environ., 112, 4204–4213, doi:10.1016/j.rse.2008.07.004, 2008.

Slobbe, D., Ditmar, P., and Lindenbergh, R.: Estimating the rates of mass change, ice volume change and snow volume change in Greenland from ICESat and GRACE data, Geophys. J. Int., 176, 95–106, doi:10.1111/j.1365-246X.2008.03978.x, 2009.

Smith, B. E., Bentley, C. R., and Raymond, C. F.: Recent elevation changes on the ice streams and ridges of the Ross Embayment from ICESat crossovers, Geophys. Res. Lett., 32, L21S09, doi:10.1029/2005GL024365, 2005.

Smith, B. E., Fricker, H. A., Joughin, I. R., and Tulaczyk, S.: An inventory of active subglacial lakes in Antarctica detected by ICESat (2003–2008), J. Glaciol., 55, L21S09, doi:10.3189/002214309789470879, 2009.

Sørensen, L. S. and Forsberg, R.: Greenland ice sheet mass loss from GRACE monthly models, Gravity Geoid Earth Observ., 135, 527–532, doi:10.1007/978-3-642-10634-7_70, 2010.

Spada, G. and Stocchi, P.: SELEN: a Fortran 90 program for solving the "Sea Level Equation", Comput. Geosci., 33(4), 538–562, doi:10.1016/j.cageo.2006.08.006, 2007.

Spada, G., Colleoni, F., and Ruggieri, G.: Shallow upper mantle rheology and secular ice sheets fluctuations, Tectonophysics, doi:10.1016/j.tecto.2009.12.020, in press, 2010.

Stendel, M., Christensen, J., and Petersen, D.: Ten years of monitoring and research at Zackenberg Research station, Norheast Greenland, in: High Arctic Ecosystem Dynamics in a Changing Climate, vol. 20, 13–43, Academic Press, 2008.

Thomas, R., Frederick, E., Krabill, W., Manizade, S., and Martin, C.: Progressive increase in ice loss from Greenland, Geophys. Res. Lett., 33, L10503, doi:10.1029/2006GL026075, 2006.

Thomas, R., Davis, C., Frederick, E., Krabill, W., Li, Y., Manizade, S., and Martin, C.: A comparison of Greenland ice-sheet volume changes derived from altimetry measurements, J. Glaciol., 54, 203–212, doi:10.3189/002214308784886225, 2008.

Thomas, R., Frederick, E., Krabill, W., Manizade, S., and Martin, C.: Recent changes on Greenland outlet glaciers, J. Glaciol., 55, 147–162, doi:10.3189/002214309788608958, 2009.

van den Broeke, M., Bamber, J., Ettema, J., Rignot, E., Schrama, E., van de Berg, W. J., van Meijgaard, E., Velicogna, I., and Wouters, B.: Partitioning recent greenland mass loss, Science, 326, 984–986, doi:10.1126/science.1178176, 2009.

Velicogna, I.: Increasing rates of ice mass loss from the Greenland and Antarctic ice sheets revealed by GRACE, Geophys. Res. Lett., 36, L19503, doi:10.1029/2009GL040222, 2009.

Velicogna, I. and Wahr, J.: Greenland mass balance from GRACE, Geophys. Res. Lett., 32, L18505, doi:10.1029/2005GL023955, 2005.

Wouters, B., Chambers, D., and Schrama, E. J. O.: GRACE observes small-scale mass loss in Greenland, Geophys. Res. Lett., 35, L20501, doi:10.1029/2008GL034816, 2008.

Wu, X., Heflin, M., Schotman, H., Vermeersen, B., Dong, D., Gross, R., Ivins, E., Moore, A., and Owen, S.: Simultaneous estimation of global present-day water transport and glacial isostatic adjustment, Nat. Geosci., 3, 642–646, doi:10.1038/ngeo938, 2010.

Zwally, H. J. and Li, J.: Seasonal and interannual variations of firn densification and ice-sheet surface elevation at the Greenland summit, J. Glaciol., 48, 199–207, doi:10.3189/172756502781831403, 2002.

Zwally, H., Schutz, R., Bentley, C., Bufton, J., Herring, T., Minster, J., Spinhirne, J., and Thomas, R.: GLAS/ICESat L2 Antarctic and Greenland ice sheet altimetry data V031, National Snow and Ice Data Center, Boulder, CO, avilable at: http://nsidc.org/data/gla12.html, 2010.

Zwally, H. J., Li, J., Brenner, A. C., Beckley, M., Cornejo, H. G., DiMarzio, J., Giovinetto, M. B., Neumann, T., Robbins, J., Saba, J. L., Yi, D., and Wang, W.: Greenland ice sheet mass balance: distribution of increased mass loss with climate warming; 2003-07 versus 1992–2002, J. Glaciol., 57(201), 88–102, 2011.

II

Towards constraining glacial isostatic adjustment in Greenland using ICESat and GPS observations

By

Nielsen, K., Sørensen, L. S., Khan, S. A., Spada, G., Simonsen, S. B.,
and Forsberg, R.

Publication details

Accepted for published in *International Association of Geodesy Symposia*.

Abstract

Constraining glacial isostatic adjustment (GIA) i.e. the Earth's viscoelastic response to past ice changes, is an important task, because GIA is a significant correction in gravity-based ice sheet mass balance estimates. Here, we investigate how temporal variations in the observed and modeled crustal displacements due to the Earth's response to ongoing ice mass changes can contribute to the process of constraining GIA. We use mass change grids of the Greenland ice sheet (GrIS) derived from NASA's high resolution Ice, Cloud and land Elevation Satellite (ICESat) data in three overlapping time spans covering the period 2004-2009 to estimate temporal variations in the elastic response due to present day ice mass loss. The modeled crustal displacements (elastic + GIA) are compared with GPS time series from five permanent sites (KELY, KULU, QAQ1, THU2, and SCOR). We find, that the modeled pattern of elastic crustal displacements shows pronounced variation during the observation period, where an increase in elastic displacement is found

at the northwest coast of Greenland, while a decrease is found at the southeast coast. This pattern of temporal changes is supported by the GPS observations. We find, that the temporal behavior of the ICESat-based modeled elastic response agrees well with the GPS observations at the sites KELY, QAQ1, and SCOR. This suggests, that our elastic models are able to resolve the temporal changes in the observed uplift, which indicates that the elastic uplift models are reliable at these sites. Therefore, we conclude that these sites are useful for constraining GIA.

Introduction

The Gravity Recovery and Climate Experiment (GRACE) satellites measure the combined gravity change, resulting from e.g. present day ice mass changes and mass movements in the mantle due to GIA. Therefore, reliable estimates of GIA are an important part of ice sheet mass balance studies based on GRACE observations. The currently available GIA models predict quite different present day signals in ice covered regions such as Greenland and Antarctica, because the data (indicators of past sea level, such as marine deposits, and geological evidence of ice sheet extent) used to develop the ice history are sparse in these regions. It is therefore important to constrain the GIA signal in these areas, using additional data such as GPS observations of crustal movement.

Today, several GPS stations are located along the coast of Greenland, continuously measuring the bedrock motion. This motion contains contributions from the elastic deformation of the Earth to ongoing ice mass changes, the viscoelastic response due to past glacial changes, i.e. GIA, and possibly tectonic motion. Due to considerably mass loss of the GrIS over the last decade, and associated unloading of the Earth, the elastic signal of bedrock movement is dominant, compared to the GIA signal, in large parts of the coastal areas. It is therefore important to model the present day elastic response with high resolution and precision when GPS observations are used to constrain the GIA signal. Several studies have used GPS observations to constrain GIA models, in Antarctica (Bevis et al., 2009; Thomas et al., 2011), and in Greenland (Khan et al., 2008; King et al., 2010; Spada et al., 2012). In these studies the elastic signal is subtracted from the GPS observations, to constrain the GIA signal hence relying on the accuracy of the elastic correction or its minor influence at the GPS stations. Over a period of a few decades it is reasonable to assume that the crustal response caused by GIA is constant. Hence, if the elastic response is modeled correctly we expect to find a correlation between the temporal changes in GPS rates and the modeled elastic response. This hypothesis is a way to validate the modeled elastic response, which enables us to obtain more reliable constraints on the GIA response at the GPS locations.

(II.2)

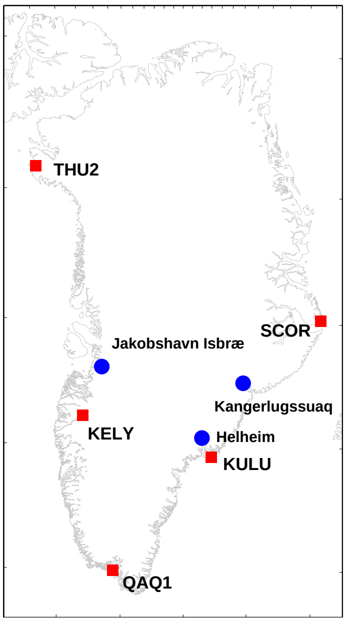

Figure II.1: Locations of the five permanent long term GPS stations, KELY, KULU, QAQ1, THU2, and SCOR indicated with red squares. The location of the three major outlet glaciers, Helheim, Kangerlussuaq and Jakobshavn are indicated with blue dots.

Here, we investigate the temporal changes in the present day elastic response caused by mass changes of the GrIS. To do so, we estimate the elastic response in three overlapping time spans 2004-2007, 2005-2008, and 2006-2009, based on mean mass change grids derived from ICESat data using the methodology described in Sørensen et al. (2011). To assess our modeled elastic response, we analyse GPS time series at five permanent stations SCOR, KULU, QAQ1, KELY and THU2. We analyze and compare the temporal changes found in the modeled elastic response and those observed by GPS. We test if this analysis improves our ability to asses the validity of the elastic signal. This will help us to identify whether the potential discrepancies between the modeled and observed present day uplift are the result of either errors in the GIA model or in the elastic model. Finally, to test the performance of GIA model estimates, which here are based on the deglaciation histories ICE-5G (Peltier, 2004), ANU05 (Fleming and Lambeck, 2004) and Huy2 (Simpson et al., 2009), we compare the sum of the modeled elastic uplift and present day GIA rates, with the observed uplift rates at the five GPS sites.

(II.3)

Data and methods

GPS

We analyze GPS data from five permanent stations, THU2, KELY, SCOR, KULU, and QAQ1. The locations of these are shown in Fig. II.1. To estimate the site coordinates, we use the GIPSY OASIS 6.1 software package (Zumberge et al., 1997) developed at the Jet Propulsion Laboratory (JPL). As an improvement to the processing done in Khan et al. (2010a), we here use IGS repro1 satellite orbits, satellite clock parameters, and Earth orientation parameters, which are probably more accurate, since they represent a combined solution from several orbits processing centers (JPL, MIT, CODE and others). The repro1 products take the satellite antenna phase center offsets into account. The GPS data is processed as described in Khan et al. (2010b). The solutions are given in the Earth's centre of mass reference frame and aligned with the IGS05 frame (Altamimi et al., 2007). Fig. II.2 shows daily vertical GPS averages at the five sites, obtained using IGS products, after removing annual and semi-annual variations. Also shown are the best fitting trends to the data during 2004-2007 (solid red curve), 2005-2008 (solid yellow curve), and 2006-2009 (solid green curve). In the three time spans all years are inclusive.

ICESat

The Geoscience Laser Altimeter System (GLAS) (Abshire et al., 2005) on board the ICESat satellite repeatedly measured the elevation of the ice sheets with a high accuracy in the period 2003 to 2009. Here, we use the data product GLA12 'Antarctic and GrIS Altimetry Data' release 31 (Zwally et al., 2010), downloaded from the National Snow and Ice Data Center. The time span of the data set used here is February 2004 to October 2009. In this analysis we leave out data from 2003 since only one month of data is available with the 91-day repeat cycle. Surface elevation changes of the GrIS are derived by applying a method (M3) presented in Sørensen et al. (2011). A mean elevation change is estimated with an along-track resolution of 500 m by least-squares fitting of rigid planes to the ICESat measurements and assuming a constant rate of elevation change. A part of the observed elevation change is not related to mass changes such as firn compaction, ICESat inter-campaign elevation biases and the response of the bedrock to mass changes. We correct for these, and use a density model to convert the estimated elevation changes into mass changes. Both the firn compaction and density models are forced by climate data from the HIRHAM5 regional climate model (Lucas-Picher et al., 2012). The procedure of deriving mass change grids from ICESat data is

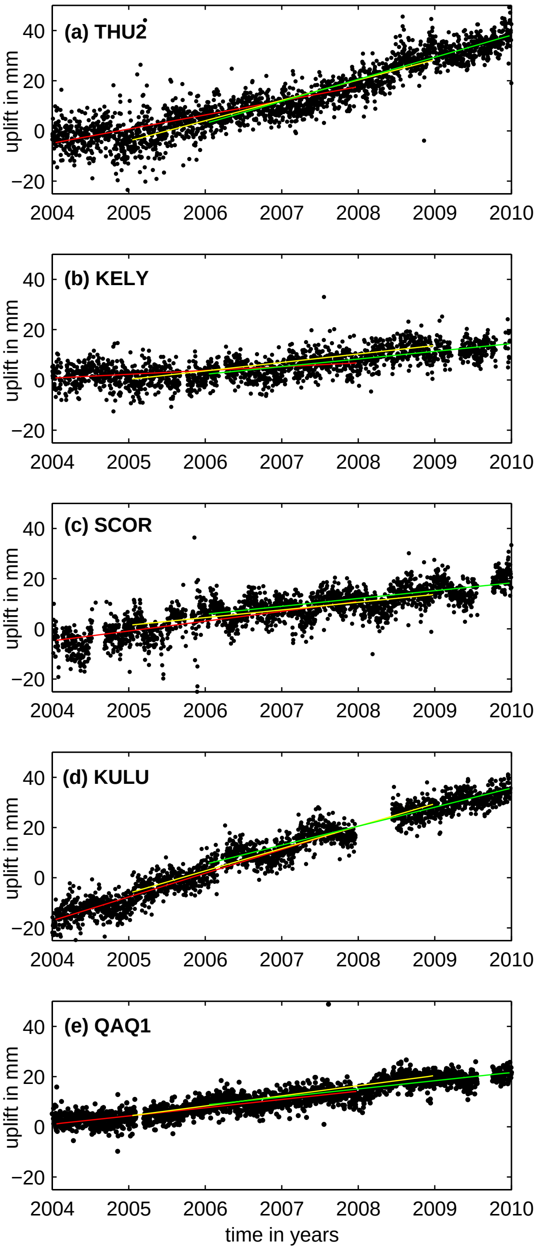

Figure II.2: Daily values of vertical positions in mm at (a) THU2, (b) KELY, (c) SCOR, (d) KULU, (e) QAQ1. Each dot represents a daily solution. The red, yellow, and green curves represents the best fitting linear terms to data during 2004-2007, 2005-2008, 2006-2009, respectively.

described in detail in Sørensen et al. (2011). Here, we derive mean mass change grids (5 km resolution) for the GrIS in three different time spans; 2004-2007, 2005-2008, and 2006-2009. This analysis shows that ICESat data can resolve temporal mass changes of the GrIS, which was not shown in Sørensen et al. (2011), where one mean mass balance estimate was derived for the period 2003-2008.

(II.5)

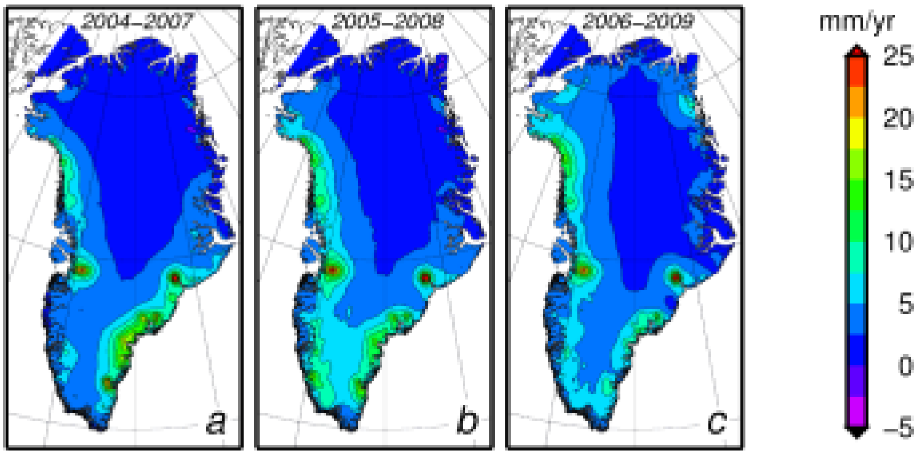

Figure II.3: Modelled elastic uplift as a function of time. The applied loading models are based on ICESat data as described in Sørensen et al. (2011). (A) shows the spatial distribution of elastic uplift, based on the mass changes between 2004 and 2007, (B) between 2005 and 2008 , and (C) between 2005 and 2008.

Modelled crustal movement

The crustal displacements are a combination of the elastic response from present day mass changes and the visoelastic effect from past ice changes occurring since the last glacial maximum. Here, we model the present day elastic movement in three overlapping time spans 2004-2007, 2005-2008, and 2006-2009, based on loading models derived from ICESat data (see section II), using the regional elastic rebound (RER) method (Spada et al., 2012). The RER method follows the Green's functions methods (Farrell, 1972), with load deformation coefficients (LDCs) based on an Earth model with PREM (Dziewonski and Anderson, 1981) structure and given in the Earth's centre of mass reference frame. The LDCs are calculated up to harmonic degree 10^5, corresponding to a spatial resolution of 0.2 km (see Spada et al. (2012) for details). The RER method is a high-resolution method developed specifically to capture the short wavelength components of the vertical elastic response to the current ice mass loss. The 5 × 5 km ICESat mass changes grid cells are converted in to discs (radius of 0.025°) with a matching area, and a convolution is performed between the elastic Green's functions and each disc-shaped mass element in the loading model.

The GIA estimates used here, are taken from the literature, with the ICE-5G and ANU05 results coming from Spada et al. (2012) and the Huy2 result coming from Simpson et al. (2011). The Huy2 is actually a regional deglaciation model for Greenland. In the study by Simpson et al. (2011), this is accounted for by using the ICE-5G deglaciation model for the non-Greenland component of the ice model. The GIA estimates are based on a radially stratified, self-gravitating Earth model. The Huy2 estimates assume a compressible Earth model, while an incompressible Earth model is assumed in the numerical implementation, performed using the Program SELEN (Spada and Stocchi, 2007), of the ICE-5G and ANU05 models. The radial viscosity structure are approximated by an elastic lithosphere, a viscous upper and lower mantle (see Table II.1). All GIA estimates are given in the Earth's centre of mass reference frame.

Table II.1: Lithosphere thickness (LT) and upper and lower mantle viscosities (UMV and LMV) used in the GIA models. These Earth model parameters are taken from Simpson et al. (2011) (Huy2) and Spada et al. (2012) (ICE-5G and ANU05)

Earth parameter	ICE-5G	ANU05	Huy2
LT (km)	90	80	120
UMV ($\times 10^{21}$ Pa s)	0.5	0.4	0.5
LMV ($\times 10^{21}$ Pa s)	2.7	10	1.0

Results

The modeled present day elastic response based on the RER method, is illustrated in Fig. II.3 for each of the three time spans. The result presented in Fig. II.3a covers the time span 2004-2007, and shows pronounced uplift along the southeast coast, with a maximum of 32 mm/yr near the Kangerlugssuaq glacier (location indicated in Fig. II.1). Strong modeled uplift signals are also observed near Jakobshavn Isbræ (location indicated in Fig. II.1) and along the northwest coast. As time evolves, depicted in Fig. II.3b and II.3c we see, that the modeled uplift pattern gradually changes, and that the area of pronounced uplift moves from the southeast coast towards the northwest and north coasts of Greenland. In Fig. II.3b, which covers the time span 2005-2008, the signal intensifies along the west coast and weakens along the southeast coast. In Fig. II.3c, which covers the time span 2006-2009 an increase in modeled elastic uplift along the north and northeast coasts of Greenland is also observed. Over the entire time span 2004-2009 we see from Fig. II.2, that the east coast GPS sites SCOR and KULU observe a decrease in uplift rates, while the west coast sites KELY and THU2 observe an increase. The site QAQ1 located at the southern tip of Greenland shows only little change in uplift rates. Fig. II.4 shows a comparison between the observed and

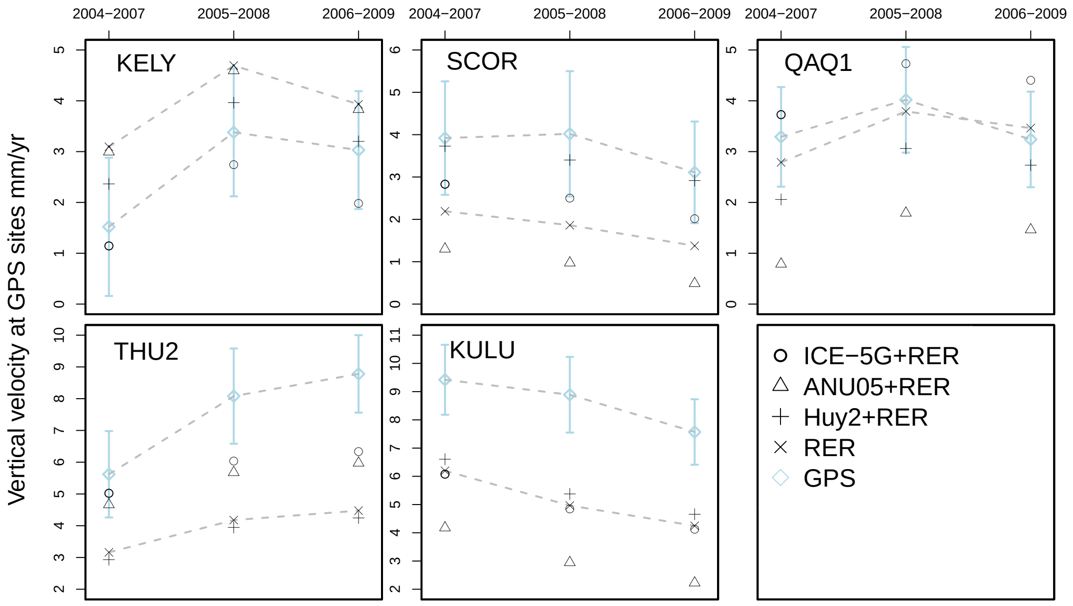

Figure II.4: Observed and modeled vertical velocities in the three time spans 2004-2007, 2005-2008, 2006-2009, at the permanent long term GPS stations KELY, KULU, QAQ1, THU2, and SCOR. The GPS rate indicated with light blue color, where the error bar represents 2σ. The modeled uplift rate, depicted with black symbols, is composed of an elastic (RER) contribution (caused by present day mass changes), and a GIA contribution (caused by past mass changes). Here the three GIA models ICE-5G, ANU05, and Huy2 have been considered. The dotted lines are added to better enlighten the comparison between observed and modeled uplift rates. Notice that the scale is different for the individual sites.

modeled (elastic + GIA) uplift rates in each of the three time spans, at the five GPS sites. For comparison the modeled elastic uplift rate is indicated with a cross. At the sites KELY, QAQ1, and SCOR, a combination of modeled elastic and at least one of the GIA-induced present day uplift rates lies within the error bars ($\pm 2\sigma$) of the GPS rates in all time spans, with RER+Huy2, RER, and RER+Huy2 as the best models, respectively. At the site THU2 we observe a fit within the error bars at the first time span with ICE-5G+RER as the best model, while at KULU none of the models fit within the error bars of the GPS rates. At all sites, we notice, that the modeled elastic and observed response follow the same temporal change (indicated by the dotted lines), though at the site THU2 the offset between the modeled elastic rates and the GPS rates shows a slightly larger variation.

(II.8)

Discussion and Conclusion

The modeled elastic response due to ice mass changes in Greenland (see Fig. II.3) shows pronounced spatial variability over the relatively short observation period of ICESat. This is the first time that the temporal changes of the the entire GrIS based on ICESat data have been used in a comparison with GPS measurements. We observe an increase in mass loss and hence also elastic uplift along the west and northwest coasts of Greenland, and a decrease along the southeast coast, considering the entire observation period 2004-2009. This change in mass loss pattern agrees well with observations made by others, based on e.g. GRACE data (Khan et al., 2010a; Chen et al., 2011; Schrama et al., 2011).

We find that the GPS uplift rates show a similar behaviour to that of the modeled elastic response, with an increase in uplift rates at sites located at the west coast of Greenland, and a decrease at sites located at the southeast coast during the observation period.

Comparing the modeled (GIA + RER) and observed present day uplift rates at the five GPS sites (see Fig. II.4), a good fit is found at the sites KELY, QAQ1, and SCOR, where one or more of the models fit within the error bars of the GPS. At these sites the modeled elastic and the observed uplift rates follow the same temporal behavior (see Fig. II.4). This demonstrates, that the elastic uplift models are able to resolve the temporal changes observed at the GPS sites and indicates that the elastic signal has been captured correctly.

At the site KULU none of the models (GIA+RER) fit the GPS rates, despite the nearly constant offset between the modeled elastic and observed uplift rates (see Fig. II.4). Based on these considerations alone, it is not possible to determine whether these discrepancies between the modeled and observed uplift, are a result of errors in the GIA models or a bias in the mass change estimate, which leads to a bias in the elastic uplift signal. ICESat data has a lower resolution in the southern part of Greenland, where the tracks are separated with up to 30 km, hence ICESat might not be able to capture the entire mass loss signal here. This was shown in a study by Howat et al. (2008), where a higher volume loss was obtained in southeastern Greenland by combining ICESat and ASTER data, compared to only using ICESat data. From this additional knowledge we conclude, that the discrepancies between the modeled and observed uplift are most likely caused by a bias in the mass loss estimate.

At the site THU2 the fit is good at the first time span, but all models fall outside the error bars of the GPS in the last two time spans. This suggests, that the elastic response is not captured completely in the model, at this site. The majority of outlet glaciers along the northwest coast of Greenland have widths near the front of less than 7 km (McFadden et al., 2011), hence the complete mass loss signal might not be captured by the resolution of ICESat, which might explain the under estimation of the modeled elastic uplift in the last two time spans (see Fig. II.4).

The agreement in temporal change between the observed and modeled elastic crustal response is a strong indicator of good quality in the modeled elastic response. However, it can not be ruled out that a constant bias is present in the modeled elastic response, e.g. due to sparsely sampled data, which is most likely the case at the site KULU. Based on our results we notice that generally a better fit between modeled and observed crustal displacements is found at sites located relative far from areas with considerable mass loss (e.g. KELY, QAQ1, and SCOR), while a poorer fit is found at KULU (located 90 km from Helheim glacier, location indicated in Fig. II.1) and THU2 (located 20 km from a smaller glacier). This suggests that the elastic rebound models, derived from ICESat data, captures the main part of the signal well, but miss the very short wavelengths due to the resolution of ICESat.

From analyzing the temporal changes of the observed and modeled elastic uplift we conclude that this approach gives additional information of the validity of the modeled elastic uplift, and hence also in the ability to constrain GIA. Based on the discussion above we find that the sites KELY, QAQ1, and SCOR are suitable for constraining the GIA signal. At these sites, we find the RER+Huy2 to be the best performing model. At the moment the sites KULU and THU2 are not suitable, probably due to errors in the modeled elastic uplift.

Satellite missions such as CryoSat-2 and ICESat-2 will enable us to extend the time series of high resolution elevation changes of the ice sheets. Having longer time series of mass changes will enable us to derive elastic uplift models based on temporal independent data. This will make the method presented here even more applicape in constraining GIA.

Acknowledgements

This work was supported by funding from the ice2sea programme from the European Union 7th Framework Programme, grant number 226375. Ice2sea contribution number 080. This work was partly supported by COST Action ES0701 “Improved Constraints on Models of Glacial Isostatic Adjustment”. We thank the Editor-in-Chief Pascal Willis and the three anonymous reviewers for their constructive comments and suggestions, which have helped to improve this manuscript.

Bibliography

Abshire, J., Sun, X., Riris, H., Sirota, J., McGarry, J., Palm, S., Yi, D., Liiva, P., 2005. Geoscience laser altimeter system (glas) on the icesat mission: On-orbit measurement performance. Geophys. Res. Lett 32 (21), L21S02.

Altamimi, Z., Collilieux, X., Legrand, J., Garayt, B., Boucher, C., 2007. ITRF2005: A new release of the International Terrestrial Reference Frame based on time series of station positions and Earth Orientation Parameters. J. Geophys. Res. 112 (B9), B09401.

Bevis, M., Kendrick, E., Smalley Jr, R., Dalziel, I., Caccamise, D., Sasgen, I., Helsen, M., Taylor, F., Zhou, H., Brown, A., et al., 2009. Geodetic measurements of vertical crustal velocity in West Antarctica and the implications for ice mass balance. Geochem. Geophys. Geosyst 10 (10), Q10005.

Chen, J., Wilson, C., Tapley, B., 2011. Interannual variability of Greenland ice losses from satellite gravimetry. J. Geophys. Res. 116 (B7), B07406.

Dziewonski, A., Anderson, D., 1981. Preliminary reference Earth model. Phys. Earth Planet. In. 25 (4), 297–356.

Farrell, W., 1972. Deformation of the Earth by surface loads. Rev. Geophys. 10 (3), 761–797.

Fleming, K., Lambeck, K., 2004. Constraints on the Greenland Ice Sheet since the Last Glacial Maximum from sea-level observations and glacial-rebound models. Quaternary Sci. Rev. 23 (9-10), 1053–1077.

Howat, I., Smith, B., Joughin, I., Scambos, T., 2008. Rates of southeast Greenland ice volume loss from combined ICESat and ASTER observations. Geophys Res Lett 35 (17), L17505.

Khan, S., Liu, L., Wahr, J., Howat, I., Joughin, I., van Dam, T., Fleming, K., 2010b. GPS measurements of crustal uplift near Jakobshavn Isbræ due to glacial ice mass loss. J. Geophys. Res. 115 (B9), B09405.

Khan, S., Wahr, J., Bevis, M., Velicogna, I., Kendrick, E., 2010a. Spread of ice mass loss into northwest Greenland observed by GRACE and GPS. Geophys. Res. Lett. 37 (6), L06501.

Khan, S., Wahr, J., Leuliette, E., van Dam, T., Larson, K., Francis, O., 2008. Geodetic measurements of postglacial adjustments in Greenland. J. Geophys. Res. 113 (B2), B02402.

King, M., Altamimi, Z., Boehm, J., Bos, M., Dach, R., Elosegui, P., Fund, F., Hernández-Pajares, M., Lavallee, D., Mendes Cerveira, P., et al., 2010. Improved constraints on models of glacial isostatic adjustment: a review of the contribution of ground-based geodetic observations. Surv. Geophys., 1–43.

Lucas-Picher, P., Wulff-Nielsen, M., Christensen, J., Aðalgeirsdóttir, G., Mottram, R., Simonsen, S., 2012. Very high resolution regional climate model simulations over Greenland: Identifying added value. J. Geophys. Res. 117 (D2), D02108.

McFadden, E., Howat, I., Joughin, I., Smith, B., Ahn, Y., 2011. Changes in the dynamics of marine terminating outlet glaciers in west Greenland (2000–2009). J. Geophys. Res. 116 (F2), F02022.

Peltier, W., 2004. Global glacial isostasy and the surface of the ice-age Earth: the ICE-5G (VM2) model and GRACE. Annu. Rev. Earth Planet. Sci. 32, 111–149.

Schrama, E., Wouters, B., Vermeersen, B., 2011. Present day regional mass loss of Greenland observed with satellite gravimetry. Surv. Geophys., 1–9.

Simpson, M., Milne, G., Huybrechts, P., Long, A., 2009. Calibrating a glaciological model of the Greenland ice sheet from the last Glacial Maximum to present-day using field observations of relative sea level and ice extent. Quaternary Sci. Rev. 28 (17), 1631–1657.

Simpson, M., Wake, L., Milne, G., Huybrechts, P., 2011. The influence of decadal-to millennial-scale ice mass changes on present-day vertical land motion in Greenland: Implications for the interpretation of GPS observations. J. Geophys. Res. 116 (B2), B02406.

Sørensen, L. S., Simonsen, S. B., Nielsen, K., Lucas-Picher, P., Spada, G., Adalgeirsdottir, G., Forsberg, R., Hvidberg, C. S., 2011. Mass balance of the Greenland ice sheet (2003–2008) from ICESat data - the impact of interpolation, sampling and firn density. The Cryosphere 5 (1), 173–186.

Spada, G., Ruggieri, G., Sørensen, L., Nielsen, K., Melini, D., Colleoni, F., 2012. Greenland uplift and regional sea level changes from ICESat observations and GIA modelling. Geophys. J. Int. 189, 1457–1474.

URL `http://onlinelibrary.wiley.com/doi/10.1111/j.1365-246X.2012.05443.x/abstract`

Spada, G., Stocchi, P., 2007. SELEN: A Fortran 90 program for solving the“sea-level equation”. Comput. Geosci. 33, 538–562.

Thomas, I., King, M., Bentley, M., Whitehouse, P., Penna, N., Williams, S., Riva, R., Lavallee, D., Clarke, P., King, E., et al., 2011. Widespread low rates of Antarctic glacial isostatic adjustment revealed by GPS observations. Geophys. Res. Lett. 38 (22), L22302.

Zumberge, J., Heflin, M., Jefferson, D., Watkins, M., Webb, F., 1997. Precise point positioning for the efficient and robust analysis of GPS data from large networks. J. Geophys. Res. 102 (B3), 5005–5017.

Zwally, H., Schutz, R., Bentley, C., Bufton, J., Herring, T., Minster, J., Spinhirne, J., Thomas, R., 2010. GLAS/ICESat L2 Antarctic and Greenland ice sheet altimetry data V031. National Snow and Ice Data Center, Boulder, CO.
URL `ftp://n4ftl01u.ecs.nasa.gov/SAN/GLAS/GLA12.031`

III

Crustal uplift due to ice mass variability on Upernavik Isstrøm, west Greenland

By

Nielsen, K., Khan, S. A., Korsgaard, N. J., Kjær, K. H, Wahr, J., Bevis, M., Stearns, L. A, and Timm, L. H.

Publication details

Accepted for publication in *Earth and Planetary Science Letters*.

Abstract

We estimate the mass loss rate of Upernavik Isstrøm (UI) using surface elevation changes between a SPOT 5 Digital Elevation Model (DEM) from 2008 and NASA's Airborne Topographic Mapper (ATM) data from 2010. To assess the validity of our mass loss estimate, we analyze GPS data between 2007 and 2011 from two continuous receivers, UPVK and SRMP which are established on bedrock and located $\sim$65 and $\sim$2 km from the front of UI, respectively. We construct along-track elevation changes on UI for several time intervals during 2005 - 2011, based on ATM, SPOT 5 and Ice, Cloud, and land Elevation Satellite (ICESat) data to assess temporal changes of UI. We estimate a mass loss rate of -6.7 ± 4.2 Gt/yr, over an area of $\sim$1600 km^2. The ice mass loss occurs primarily over the northern glacier of UI. This pattern is also observed $\sim$40 km upstream, where we observe glacier thinning at a rate of -1.6 ± 0.3 m/yr across the northern portion of UI and -0.5 ± 0.1 m/yr across the southern portion. GPS measurements suggest bedrock uplift rates of 7.6 ± 0.6 mm/yr (UPVK) and 16.2 ± 0.6 mm/yr (SRMP). The modeled ice mass loss of UI causes bedrock uplift rates of 1.3 ± 0.6 mm/yr (UPVK) and 8.3 ± 4.2 mm/yr (SRMP). Including additional contributions from ice mass changes outside UI and from Glacial Isostatic Adjustment (GIA), we obtain total modeled uplift rates of 4.7 ± 0.6 mm/yr (UPVK) and 13.8 ± 4.2 mm/yr (SRMP). The modeled uplift rates from our UI ice mass loss are substantially lower, indicating that additional mass loss is taking place outside of UI. We obtain a difference of 0.6 mm/yr between the modeled and observed relative uplift rates (SRMP relative to UPVK), suggesting that the mass loss of UI is well captured in the model. We observe elevation changes from -15 to -40 m/yr near the front during the period 2005 - 2011, indicating that UI undergoes large variations in thinning pattern over short time spans.

Introduction

Over the last decade many outlet glaciers in Greenland have experienced an increase in flow rate (Rignot and Kanagaratnam, 2006; Joughin et al., 2010), initially causing frontal thinning, and later followed by increased thinning inland (Howat et al., 2007; Pritchard et al., 2009). Early in the last decade the Greenland mass loss was most pronounced in the southeast coast of Greenland, with Helheim and Kangerdlugssuaq as the largest individual contributing glaciers. This increase in mass loss later (∼2005) shifted to the northwest and northern coasts of Greenland (Pritchard et al., 2009; Khan et al., 2010a; Schrama et al., 2011). Frontal and inland thinning of the many small glaciers along the northwest coast contribute to ∼20% of the annual mass loss rate (2003 - 2008) of the Greenland ice sheet (Van Den Broeke et al., 2009), making it an important region to understand.

Upernavik Isstrøm (UI), located at the northwest coast of Greenland, is a system of four glaciers (Fig. IV.1). UI has retreated by up to 20 km since the end of the Little Ice Age (LIA) (Weidick, 1958; Kollmeyer, 1980), with the maximum retreat between 1931 - 1946. Here, we present a mass loss estimate for UI, based on elevation changes between a SPOT 5 DEM from June 3 2008 and on NASA's ATM altimetry data from May 2010 (Krabill, 2011). To assess our UI mass loss estimate, we analyse GPS data during the period July 2007 to April 2011 from two permanent sites SRMP and UPVK (Fig. IV.1). We compare observed and modeled rates of vertical crustal displacements, using previously published methodology (Khan et al., 2007, 2010b). Modeled rates consist of three components: elastic uplift caused by UI ice mass changes, elastic uplift caused by ice mass changes outside UI, and GIA, due to changes in the ice load since the last glacial maximum. Here, we use the estimated gridded mass change values to model uplift rates caused by UI. The contribution from ice mass changes outside of UI are based on a mass change grid derived from ICESat data (Zwally et al., 2010) during 2006 - 2009. The GIA contribution is based on ICE-5G(VM2) (Peltier, 2004). To analyze thinning upstream we use time series of ice elevations obtained from a combination of ICESat, ATM, and GPS measurements during 2003 - 2010. The time series are created at three GPS stations located on ice ~40 km from the glacier front (marked as A, B, and C in Fig. IV.1). We quantify changes on UI from 2005 - 2011, by estimating along-track elevation changes based on SPOT 5, ATM and ICESat data.

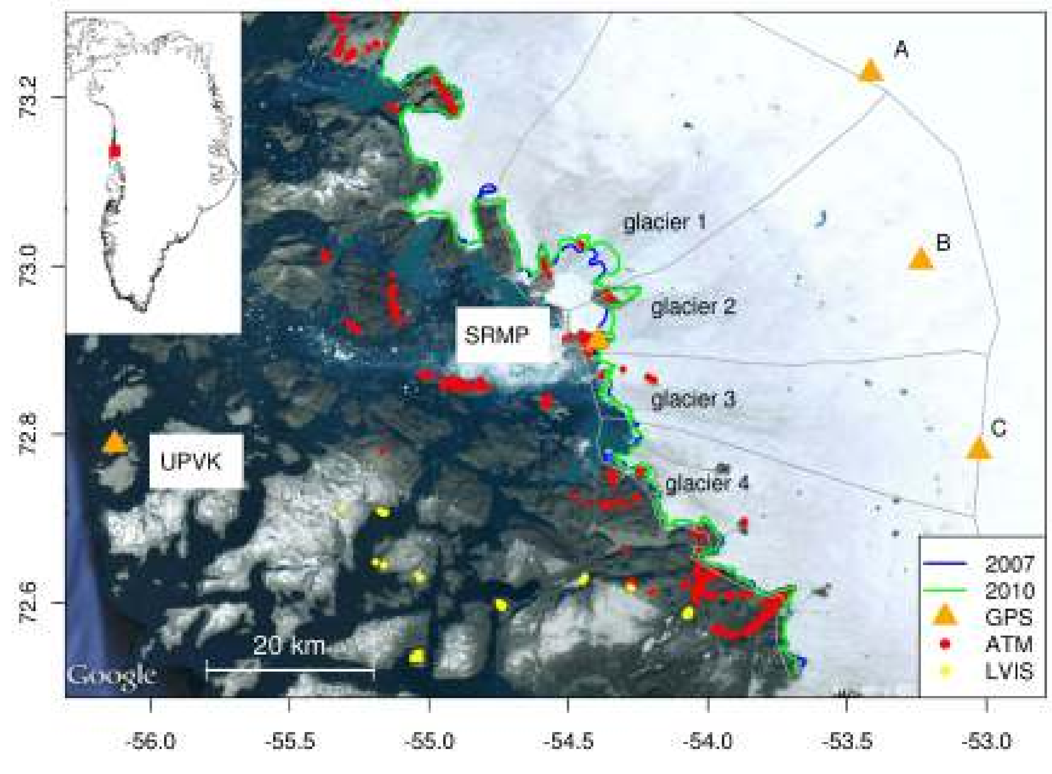

Figure III.1: An overview of UI. The blue and green lines are the August 2007 and 2010 calving fronts, respectively, which are obtained from Landsat images. Orange triangles show the positions of GPS receivers. The red and yellow dots show the positions of the ATM and LVIS data used to validate the SPOT 5 DEM. The gray lines indicate a subdivision of UI into areas that represent the individual glaciers.

(III.3)

Data and methods

SPOT 5 HRS DEM

The SPOT 5 HRS DEM from June 3 2008 used in this study is a product of the SPOT 5 stereoscopic survey of Polar Ice: Reference Images and Topographies (SPIRIT) Polar DALI program. The DEM resolution is 40 m, and it is referenced to the EGM96 geoid. The DEM is automatically generated and hence no ground control points have been used to control it. More information about the SPIRIT program can be found in Korona et al. (2009). To compare the SPOT 5 DEM to ATM measurements, the SPOT 5 DEM is converted to WGS84 ellipsoid heights.

Validation of SPOT 5 DEM

Several studies have shown that distortions and biases are present in SPOT 5 DEMs (Korona et al., 2009; Motyka et al., 2010; Scambos et al., 2011; Nuth and Kääb, 2011). Korona et al. (2009) reported biases between -5.5 m and 3.5 m and uncertainties ranging from 3.5 m to 8.9 m (RMS) using ICESat data over glacier ice for testing. Others, e.g. Nuth and Kääb (2011) have addressed error corrections of elevation models developed from satellite acquired imagery, using stable terrain for validation.

Here, we use ATM data between 1994 and 2011 (Krabill, 2011) and Laser Vegetation Imaging Sensor (LVIS) data from 2010 (Blair and Hofton, 2010) over stable ice free terrain including nunataks, to asses the validity of the SPOT 5 DEM (Fig. IV.1). Areas of interest for validation are manually selected using the 10 m SPOT 5 imagery homologous to the DEM. We extract SPOT 5 elevations corresponding to the ATM and LVIS sample values, using bi-linear interpolation to obtain elevation differences, with SPOT 5 as the reference. To minimize errors in the elevation differences due to possible inaccurate horizontal positions in the SPOT 5 DEM, we filter for SPOT 5 slopes, so that only elevation differences with slopes $<$ 5 degrees are used for validation. After filtering the initial 32946 elevation differences, 3391 elevation differences with a slope $<$ 5 degrees are left for correction. We fit a mixed distribution, consisting of normal and T-distributions to the distribution of elevation changes (Fig. III.2), and obtain a bias of 3.8 ± 3.9 m (σ), which is applied to the SPOT 5 DEM, hence raising the surface by 3.8 m. We apply a bias correction only, because the majority of the investigated area is dominated by gently sloping ice.

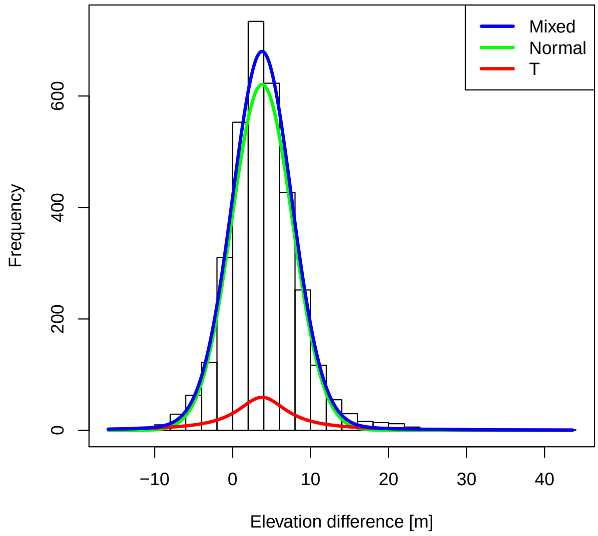

Figure III.2: Histogram and density plot of elevation differences between ATM+LVIS data and the SPOT 5 DEM. The red and green curves represent a T- and a normal distribution. The blue curve, the mixed distribution, is the sum of the normal and T-distributions.

GPS

We analyze data from two permanent continuous GPS receivers located $\sim$2 and $\sim$65 km from the front of UI, west Greenland. The station, UPVK, at Upernavik was established by DTU Space in 2007, and the station, SRMP, located a few km from the calving front of UI was installed in 2007 by Ohio State University as part of the Greenland GPS network (GNET) (Fig. IV.1). Data acquisition has been continuous for both sites. To estimate site coordinates, we use the GIPSY OASIS 6.1.2 software package (Zumberge et al., 1997) released in January 2012 and developed at the Jet Propulsion Laboratory (JPL). The orbit products we use were released in 2010 by the International GNNS Service (IGS) (repro1 products) and include satellite orbits, satellite clock parameters, and Earth orientation parameters. The new orbit products take the satellite antenna phase center offsets into account. Receiver clock parameters are modeled, and the atmospheric delay parameters are modeled using the Global Mapping Function (GMF) (Böhm et al., 2006). Corrections are applied to remove the solid Earth tide and ocean tidal loading. The amplitudes and phases of the main ocean tidal loading terms are calculated with the Automatic Loading Provider (`http://www.oso.chalmers.se/~loading`, Scherneck and Bos (2002)) on the basis of the FES2004 ocean tide model including correction for center of mass motion of the Earth due to the ocean tides. The site coordinates are computed in the non-fiducial frame and transformed to the ITRF2005 frame (Altamimi et al., 2007). We estimate the secular trends and their uncertainty as described by Khan et al. (2010b).

Volume change

To estimate the volume change of UI we first estimate elevation changes between the 2008 SPOT 5 DEM and 2010 ATM data. For each ATM data point we extract the closest SPOT 5 value, where the maximum spatial distance between elevation points is 28 m. Over this distance, it is reasonable to assume that the contribution to the apparent elevation change from topography is negligible. The spatial distribution of the volume change is estimated by ordinary local neighborhood kriging, using a nested exponential variogram model with ranges $R_1 = 1$ km and $R_2 = 5$ km. The error of the total UI mass loss is determined by summing the kriging covariance matrix.

Modeled crustal response

The vertical crustal response consists of the elastic response caused by present day ice unloading of UI, present day ice unloading from areas outside UI, and GIA caused by the Earth's viscous response to past ice mass changes. The vertical present day elastic response from UI mass changes, is modeled by convolving the loading model described in section III with loading Green's functions (Farrell, 1972). To estimate the elastic response from mass changes outside UI, we use a loading model derived from ICESat data in the period 2006 - 2009. This loading model is estimated on a 5 × 5 km grid according to the M3 method described in Sørensen et al. (2011). After removing UI from the loading model, the elastic uplift is estimated according to the regional elastic rebound (RER) method in Spada et al. (2012). In this method the loading model M3 is discretized into disc shaped loads and convolved with loading Green's functions, which are based on an Earth model with PREM (Dziewonski and Anderson, 1981) structure. The corresponding uncertainties are estimated by a bootstrap approach. On the basis of ICESat 2006 - 2009 elevation change data, derived according to the M3 method, we construct 1000 different elevation change data sets, by drawing random samples with replacement among tracks in the original elevation change data set. For each bootstrapped data set we estimate a loading model as described in Sørensen et al. (2011), from which we estimate the elastic uplift using the RER method (Spada et al., 2012). This gives a distribution of the uplift from which the standard deviation can be found.

The GIA contribution to the crustal response is estimated using an improved version (version 2.9.8) of the software SEa Level EquatioN solver (SELEN) available at `http://www.fis.uniurb.it/spada/SOFT.html` (Spada and Stocchi, 2007). We use the ice-history "ICE-5G (VM2 L90) model version 1.2" (Peltier, 2004), where the VM2 viscosity profile is approximated by a two layer mantle model with an upper and lower mantle viscosity of 0.5 and 2.7 $\times 10^{21}$ Pa s respectively. It should be noticed, that ICE-5G does not account for post-LIA and the most recent ice mass changes. The present day GIA estimate depends on the Earth's viscosity structure. Hence, to assess the variation of GIA estimates due to viscosity, we run SELEN for a suite of Earth models, where the upper mantle viscosity range between 0.3 - 1.0 $\times 10^{21}$ Pa s and the lower mantle viscosity range between 1.3 - 5.4 $\times 10^{21}$ Pa s. This corresponds to a variation of the viscosity from the preferred model equal to $10^{20.7\pm0.3}$ Pa s and $10^{21.43\pm0.3}$ Pa s for the upper and lower mantle, respectively.

Results

Volume change of UI between 2008 and 2010

The annual along-track elevation changes between 2008 and 2010 are displayed in Fig. III.3, and the elevation change estimates on a 1 × 1 km grid are shown in Fig. III.4 together with their associated kriging uncertainties. UI is primarily thinning across glacier 1, with an average rate of up to -15 m/yr during 2008 - 2010. Thinning from this glacier extends far inland. Glaciers 2 and 4 show minor thinning near the front with average rates of up to -7 m/yr; glacier 3 shows practically no thinning. The rate of volume change for the total area is -7.3 ± 4.6 km^3/yr (σ). Since the area is below the equilibrium line altitude, it is reasonable to assume an ice density of 917 kg/m^3, which gives an estimated total mass loss rate of -6.7 ± 4.2 Gt/yr (σ). For the entire area the average annual mass loss is not significant at the 5 % level (2σ). Still, we do observe significant local mass loss at individual grid points within UI, primarily over glacier 1. Areas with a significant mass loss are indicated with solid dots in Fig. III.4. To further demonstrate a local significant mass loss within UI, we estimate the mass loss of the individual glaciers in UI. With the subdivision of UI, indicated by the gray lines in Fig. IV.1, the mass loss estimates with one standard deviation σ are 4.4 ± 1.7 Gt/yr, 1.3 ± 1.2 Gt/yr, 0.4 ± 0.7 Gt/yr, 0.6 ± 0.5 Gt/yr, for glacier 1-4, respectively. Hence, only glacier 1 experiences a significant mass loss.

The error estimates are based on the kriging variances, which are sensitive to the location of the data points and to the nature of the variogram. In this case data is distributed along tracks, with a high along-track resolution, but a sparse resolution

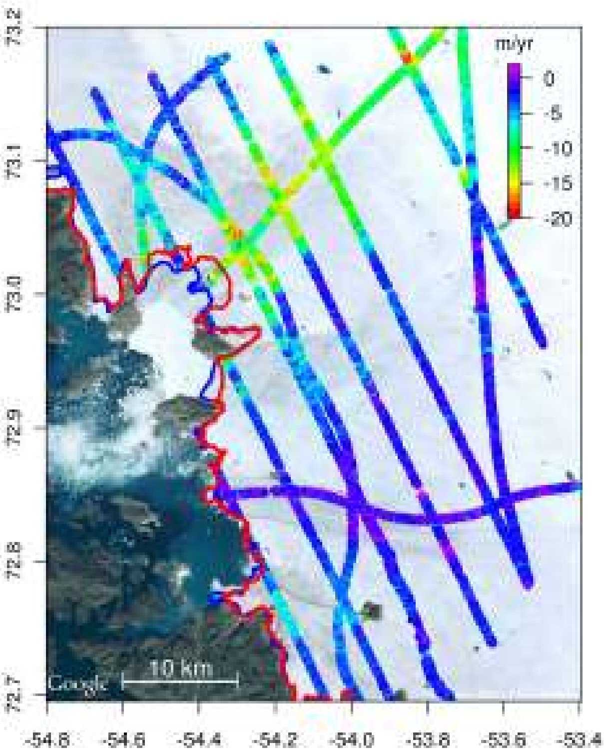

Figure III.3: Annual elevation changes between a SPOT 5 DEM acquired on June 3 2008 and ATM data from May 19-21 2010. The solid blue and red lines represent the 2007 and 2010 summer positions of the front, respectively, which are obtained from Landsat images.

across tracks. Thus, we need to interpolate over relatively large distances. This, together with the fact that the spatial distribution of elevation changes is changing rapidly over relatively short distances, leads to a high variance of the mass loss estimates.

Upstream thinning

To analyze glacier elevation changes upstream, we create elevation change time series at three GPS sites all located ∼40 km upstream from the calving front. The time series show elevations from ICESat, ATM, and GPS campaign measurements from 2010 at the GPS sites A, B, and C (Fig. IV.1). These elevation series, have error sources that introduce temporal correlations into the data. To take temporally correlated, non-Gaussian noise into account, we analyze the time series for white noise plus flicker noise using Maximum Likelihood Estimation (MLE) (Williams et al., 2004). At GPS site A we fit two linear terms to the time series (GPS, ICESat,

(III.8)

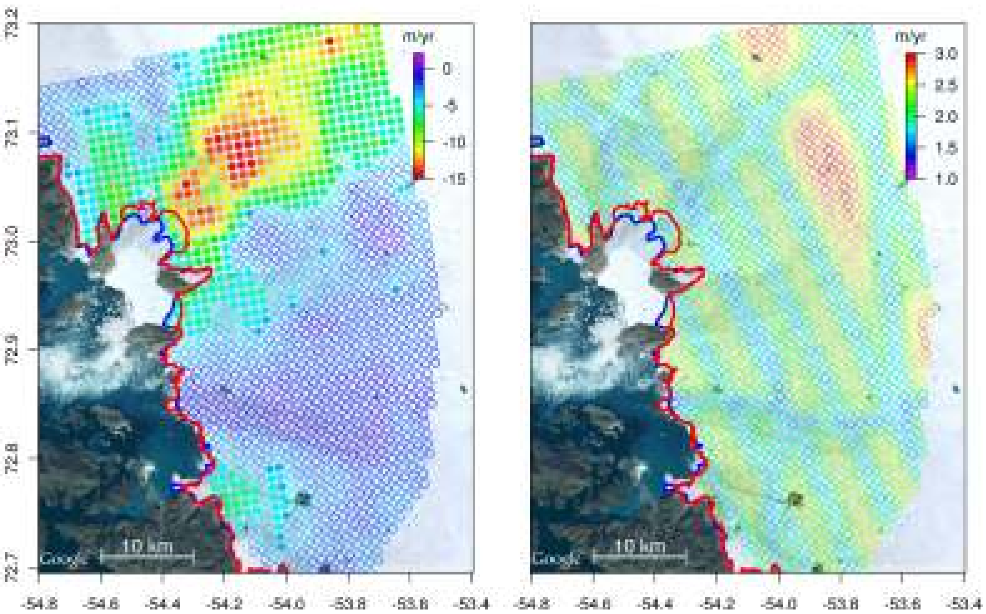

Figure III.4: Left: thinning model of UI on a 1 × 1 km grid. The solid dots indicate areas with significant elevation changes; i.e. where the elevation change is larger than 2σ. The blue and red lines represent the 2007 and 2010 summer glacier front lines, which are obtained from Landsat images. Right: kriging uncertainties (σ).

ATM elevations). We obtain elevation changes of 0.1 ± 0.4 m/yr (ice thickening) during 2003 - 2005, and -1.6 ± 0.3 m/yr (ice thinning) during 2006 - 2010 (Fig. III.5A). At the GPS sites B and C we fit one linear term only. We obtain -0.6 ± 0.3 m/yr, and -0.5 ± 0.1 m/yr at sites B and C, respectively (Fig. III.5B and III.5C). Hence, the thinning rate during 2006 - 2010 is larger upstream from glacier 1 than upstream from glaciers 2 and 3.

Elevation changes between 2005-2011

Previous studies demonstrate that glaciers can show rapid changes in dynamic thinning (Howat et al., 2007; McFadden et al., 2011). Hence, to obtain an understanding of the temporal changes on UI and to put our mass loss estimate into perspective, we estimate along-track elevation changes at various times during 2005 - 2011. Fig. III.6 shows average along-track elevation changes for different time spans, based on ATM, ICESat and SPOT 5 data. Considering the entire period, we observe the largest thinning rates at glacier 1. During the period 2005 - 2007, we observe the largest thinning rate of up to -40 m/yr near the front (Fig.

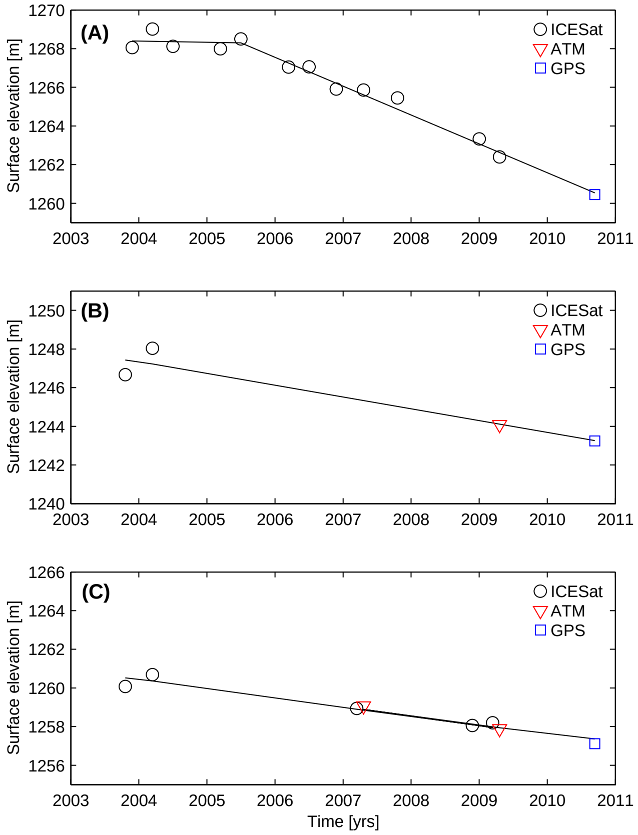

Figure III.5: Time series of elevation measurements at three GPS sites (denoted GPS A, B and C in Fig. 1). The time series show elevations from ICESat (black circles), ATM (red triangles), and GPS campaign measurements (blue squares). The top panel (A) shows elevation time series at GPS A, middle panel at GPS B, and bottom panel at GPS C. The solid lines show the best fitting trends. At GPS site A, two trends are fitted, while one trend is fitted at B and C.

III.6E and III.6F). During 2008 - 2010, we observe a deceleration in thinning (Fig III.6B-D), with the lowest rate between 2009 and 2010. Elevation changes between 2010 and 2011 suggest thinning rates of up to -30 to -35 m/yr (Fig. III.6A): similar to rates observed over the period 2005 - 2007. The observed deceleration is also described in McFadden et al. (2011). Hence, within this relatively short period we observe large variations in thinning rates.

(III.10)

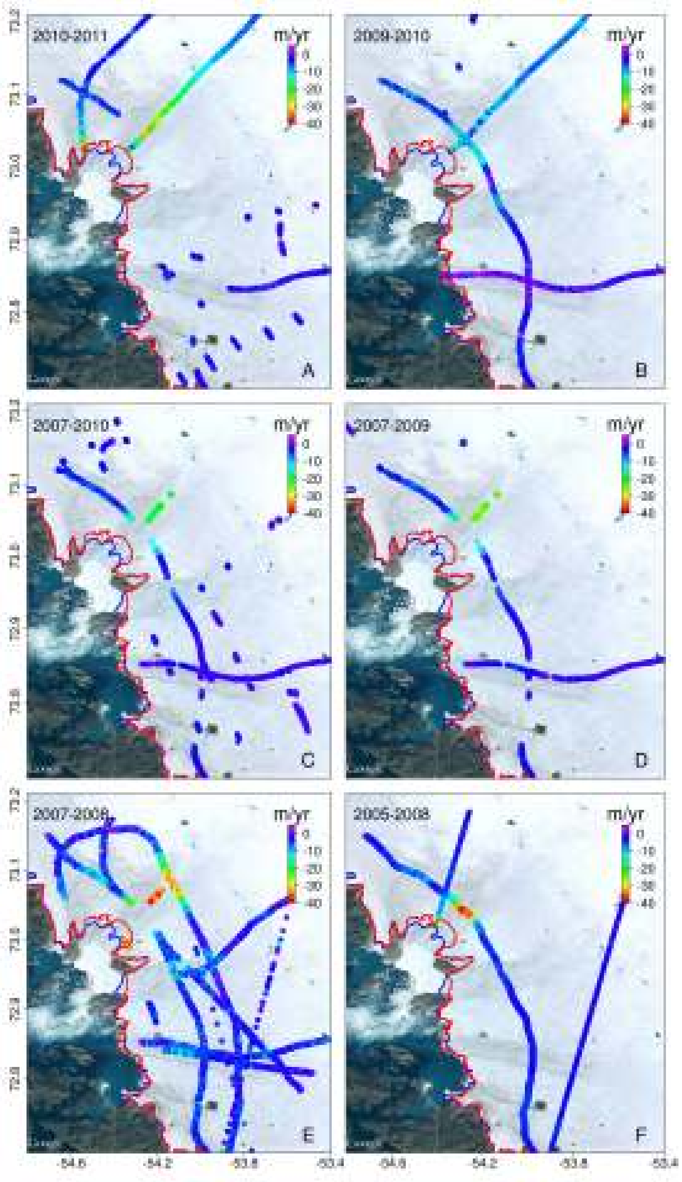

Figure III.6: Average along track elevation changes during the period 2005 - 2011. The blue and red solid curves represent the 2007 and 2010 calving fronts, respectively. (A)-(D) Average elevation changes based om ATM from (A) 2010 and 2011, (B) 2009 and 2010, (C) 2007 and 2010, and (D) 2007 and 2009. (E) and (F) Average elevation changes based on SPOT 5, ATM, and ICESat data from (E) 2007 (ATM and ICESat) and 2008 (SPOT 5) and (F) 2005 (ATM and ICESat) and 2008 (SPOT 5).

Modeled and observed uplift rates

Daily values of vertical positions at SRMP and UPVK are displayed in Fig. III.7, where each dot represents a daily solution. The black curve is the sum of the

(III.11)

best fitting secular, annually, and semi-annually varying terms to the daily vertical solutions. The SRMP time series shows an increased uplift rate starting in summer 2010. This is demonstrated by fitting a secular, an annual and a semi-annual term to data between July, 2007 and May 2010. The fitted curve does not fit SRMP observations during June 2010 to April 2011 (Fig. III.7A). In this time span the observed daily solutions lie above the fitted curve suggesting accelerated uplift.

Table III.1: Modeled and observed uplift rates at the GPS sites UPVK and SRMP. The second column displays GPS rates, third column the total modeled uplift rates, consisting of the elastic response from UI (column 4), the elastic response from outside UI (column 5), and GIA (column 6)

Station	GPS	Modeled total	Response of UI	Response outside UI	GIA[b]	
UPVK	7.7±0.6	4.7±0.6	1.3±0.6	3.8±0.1	-0.4	(-1.4;0.8)
UPVK[a]	7.6±0.6	4.7±0.6	1.3±0.6	3.8±0.1	-0.4	(-1.4;0.8)
SRMP	17.1±0.6	13.9±4.3	8.3±4.2	5.5±0.2	0.1	(-0.8;1.0)
SRMP[a]	16.2±0.6	13.9±4.2	8.3±4.2	5.5±0.2	0.1	(-0.8;1.0)
SRMP-UPVK[a]	8.6±0.8	9.2±4.2	7.0±4.2	1.7±0.3	0.5	(0.1;0.7)

[a] using data until April, 2010

[b] The GIA estimate is based on ICE-5G(VM2). Ranges of the GIA estimates are indicated in brackets. The ranges are based on a viscosity variation of 0.3 to 1.0 $\times 10^{21}$ Pa s for the upper mantle and 1.3 to 5.4 $\times 10^{21}$ Pa s for the lower mantle.

The observed and modeled rates of crustal uplift at the sites UPVK and SRMP are summarised in Table III. Here, column 2 contains observed uplift rates and column 3 contains the total modeled uplift rates, which consists of: the elastic response due to ice mass loss of UI (column 4), the elastic response due to ice mass changes outside UI (column 5), and GIA (column 6). All rates are in mm/yr and presented with one standard deviation σ, except for the GIA estimates, where a range is given instead. This range represents the possible GIA estimates related to the viscosity intervals described in Section III. "Site-name[a]" indicates that the observed uplift rate is based on GPS data until April 2010, else data until April 2011 is used. Rows 1-4 account for the absolute motions at the two sites UPVK and SRMP, while the fifth row contains the vertical rates at SRMP relative to UPVK. By considering the relative rates rather than the absolute rates for sites located relatively close to one another, we reduce errors related to GPS orbits, reference frame drift, the elastic response from loads outside the UI, and GIA. For instance we notice that the range of GIA estimates is much smaller when relative motion are

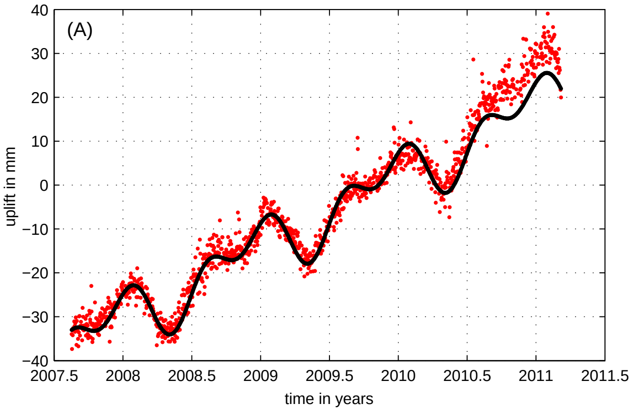

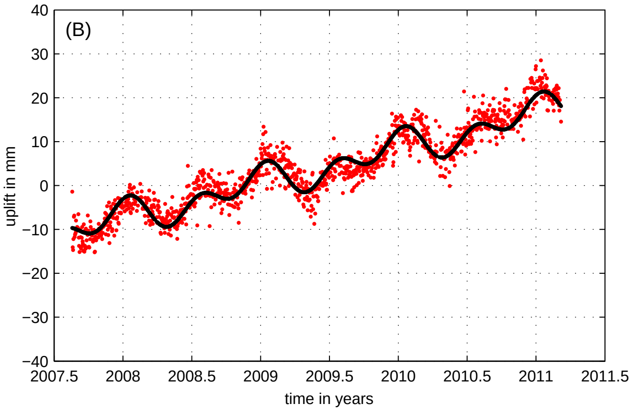

Figure III.7: (A) Daily solutions of vertical displacements in mm at SRMP. The black curve shows the sum of the best fitting annual, semi-annual, and secular terms. (B) same as (A) but for UPVK.

considered compared to absolute. When comparing observed and total modeled uplift rates we find a discrepancy of 0.6 mm/yr between the relative rates, 2.9 mm/yr in the absolute rate at UPVK, and 2.3 mm/yr at SRMP.

Discussion and Conclusions

We estimate the average annual mass loss of UI in the time span 2008 - 2010 to be -6.7 ± 4.2 Gt/yr (σ), based on elevation changes between a SPOT 5 DEM from June 3 2008 and ATM data from May 2010. Considering the entire UI, the total estimated mass loss is not significant at the 5% level. But locally within the ice stream a significant mass loss is observed, primarily at glacier 1 (indicated with solid dots on Fig. III.4). We find thinning rates of up to -15 m/yr at glacier 1, -7 m/yr at glaciers 2 and 4, and ∼0 m/yr at glacier 3. This thinning pattern is also observed upstream at three GPS stations on ice, located ∼40 km from the front (marked A, B, and C in Fig. IV.1), where station A shows a larger thinning rate than stations B and C. This suggests that the upstream thinning is dominated by frontal thinning at glacier 1.

We use GPS measurements from two permanent sites UPVK and SRMP to constrain our mass loss estimate, by comparing the modeled and observed relative motion of SRMP with respect to UPVK. We find a modeled relative uplift rate of 9.2 ± 4.2 mm/yr compared to an observed rate of 8.6 ± 0.8 mm/yr: a discrepancy of 0.6 mm/yr. This discrepancy may be slightly larger (or smaller) if the range of GIA estimates are considered (Table III). Despite the spread in the GIA estimates, there is a good agreement between the modeled and observed relative uplift rates, which suggests that the overall mass loss pattern of UI is captured correctly. However, when considering the observed and modeled absolute rates at UPVK and SRMP, we find a discrepancy of 2.9 mm/yr and 2.3 mm/yr, respectively.

These discrepancies may be caused by various sources e.g. errors in the modeled elastic uplift, errors related to GIA, errors related to GPS, and other sources. The loading model we use to estimate the Earth's elastic response from ice mass changes outside UI, does not entirely coincide in time with the GPS time series and the time span used to estimate the UI mass loss. This, together with the fact that the Greenland ice sheet shows large spatial variations in ice mass loss as a function of time (Pritchard et al., 2009; Khan et al., 2010a; Schrama et al., 2011), might cause a slight shift in the uplift estimates at UPVK and SRMP. In Section III we find that the GIA estimates at UPVK and SRMP can vary by ∼ ± 1 mm, when the upper and lower mantle viscosities are ranging as described in Section III. Hence, errors in the assumed mantle viscosities can lead to a lowering of the discrepancies between modeled and observed absolute rates, but might also result in larger discrepancies. The ICE-5G deglaciation model, that is used here, does not include the Earth's viscous response from ice mass changes related to the LIA. Early studies of UI (Weidick, 1958; Kollmeyer, 1980) have presented ice front variations since the end of the LIA, where the ice front was 10 - 20 km further away from it's present position. This retreat will have some effect on the Earth's present day viscous response, which might explain a portion of the difference between the observed and modeled absolute uplift rates. Simpson et al. (2011) shows that ice mass changes during the last 100 years, based on the ice-history Huy2 (Simpson et al., 2009), may cause a viscous response around ±0.2 mm/yr, with a positive value in the area of Upernavik. A larger signal around ±1.2 mm/yr is found for a weak upper mantle (of 10^{20} Pa s). Furthermore, previous studies have demonstrated that the GIA estimate may vary depending on which ice-history that is used (Spada et al., 2012; King et al., 2010). Additionally, unmodeled GPS orbit errors and reference frame errors, would tend to be correlated over long distances, and so would have essentially the same effect at each GPS station. Khan et al. (2010b) found a difference in uplift rate of about 0.8 mm/yr between MIT and JPL orbits. Hence, the observed discrepancy of 2.3 to 2.9 mm/yr is presumably due to a combination of unmodeled orbit errors, reference frame errors, ice load errors, and GIA errors.

The mass loss estimate of -6.7 ± 4.2 Gt/yr should not be interpreted as a long term trend, since outlet glaciers show rapid changes in discharge (Howat et al., 2007; McFadden et al., 2011). We find large variations in elevation change rates ranging from -15 to -40 m/yr, based on ATM data, ICESat data, and a SPOT 5 DEM during 2005 - 2011. The observed changes in thinning rate are consistent with observed changes in uplift rate at SRMP. For instance, we see an increase in the observed uplift rate at SRMP by considering data through April 2011 (see Table III), at UPVK the uplift rate practically remains constant, suggesting that the acceleration in 2010 at SRMP is due to ice unloading close to SRMP. This is consistent with the increased along-track thinning seen between 2010 and 2011 (Fig. III.6A). In a more general sense, this suggests that GNET GPS data will be useful for future assessments of annual variations in glacier mass balance.

Acknowledgement

We thank Louise S. Sørensen for access to the ICESat loading model, derived from data between 2006 and 2009 and Giorgio Spada for access to his software. We thank DTU Space and Finn Bo Madsen for providing GPS data from UPVK. We thank UNAVCO and Ohio State University for providing GPS data from SRMP. We thank the anonymous reviewers for their comments and suggestions, which have improved this manuscript. Work done by Karina Nielsen and Shfaqat Abbas Khan was partly funded by KVUG. GNET is supported by the Arctic Sciences Division of the U.S. National Science Foundation.

(III.16)

Bibliography

Altamimi, Z., Collilieux, X., Legrand, J., Garayt, B., Boucher, C., 2007. ITRF2005: A new release of the International Terrestrial Reference Frame based on time series of station positions and Earth Orientation Parameters. J. Geophys. Res. 112 (B9), B09401.

Blair, B., Hofton, M., 2010. IceBridge LVIS L2 geolocated ground elevation and return energy quartiles, [2010]. Boulder, Colorado USA: NASA Distributed Active Archive Center at the National Snow and Ice Data Center.
URL `http://nsidc.org/data/ilvis2.html`

Böhm, J., Niell, A., Tregoning, P., Schuh, H., 2006. Global Mapping Function (GMF): A new empirical mapping function based on numerical weather model data. Geophys. Res. Lett. 33 (7), L07304.

Dziewonski, A., Anderson, D., 1981. Preliminary reference Earth model. Phys. Earth Planet. In. 25 (4), 297–356.

Farrell, W., 1972. Deformation of the Earth by surface loads. Rev. Geophys. 10 (3), 761–797.

Howat, I., Joughin, I., Scambos, T., 2007. Rapid changes in ice discharge from Greenland outlet glaciers. Science 315 (5818), 1559.

Joughin, I., Smith, B., Howat, I., Scambos, T., Moon, T., 2010. Greenland flow variability from ice-sheet-wide velocity mapping. J. Glaciol. 56 (197), 415–430.

Khan, S., Liu, L., Wahr, J., Howat, I., Joughin, I., van Dam, T., Fleming, K., 2010b. GPS measurements of crustal uplift near Jakobshavn Isbræ due to glacial ice mass loss. J. Geophys. Res. 115 (B9), B09405.

Khan, S., Wahr, J., Bevis, M., Velicogna, I., Kendrick, E., 2010a. Spread of ice mass loss into northwest Greenland observed by GRACE and GPS. Geophys. Res. Lett. 37 (6), L06501.

Khan, S., Wahr, J., Stearns, L., Hamilton, G., van Dam, T., Larson, K., Francis, O., 2007. Elastic uplift in southeast Greenland due to rapid ice mass loss. Geophys. Res. Lett. 34 (21), L21701.

King, M., Altamimi, Z., Boehm, J., Bos, M., Dach, R., Elosegui, P., Fund, F., Hernández-Pajares, M., Lavallee, D., Mendes Cerveira, P., et al., 2010. Improved constraints on models of glacial isostatic adjustment: a review of the contribution of ground-based geodetic observations. Surv. Geophys., 1–43.

Kollmeyer, R., 1980. West Greenland outlet glaciers: an inventory of the major iceberg producers. In: World Glacier Inventory Workshop: Proceedings of the Workshop at Riederalp, Switzerland September 1978. IAHS-AISH Publication. No. 126.

Korona, J., Berthier, E., Bernard, M., RÃ©my, F., Thouvenot, E., 2009. SPIRIT. SPOT 5 stereoscopic survey of Polar Ice: Reference Images and Topographies during the fourth International Polar Year (2007-2009). ISPRS J Photogramm 64 (2), 204 – 212.

Krabill, W. B., 2011. IceBridge ATM L2 Icessn Elevation, Slope, and Roughness, [1994-2011]. Boulder, Colorado USA: NASA Distributed Active Archive Center at the National Snow and Ice Data Center. Digital media.
URL `http://nsidc.org/data/ilatm2.html`

McFadden, E., Howat, I., Joughin, I., Smith, B., Ahn, Y., 2011. Changes in the dynamics of marine terminating outlet glaciers in west Greenland (2000–2009). J. Geophys. Res. 116 (F2), F02022.

Motyka, R., Fahnestock, M., Truffer, M., 2010. Volume change of Jakobshavn Isbræ, West Greenland:: 1985–1997–2007. J. Glaciol. 56 (198), 635–646.

Nuth, C., Kääb, A., 2011. Co-registration and bias corrections of satellite elevation data sets for quantifying glacier thickness change. The Cryosphere 5, 271–290.

Peltier, W., 2004. Global glacial isostasy and the surface of the ice-age Earth: the ICE-5G (VM2) model and GRACE. Annu. Rev. Earth Planet. Sci. 32, 111–149.

Pritchard, H., Arthern, R., Vaughan, D., Edwards, L., 2009. Extensive dynamic thinning on the margins of the Greenland and Antarctic ice sheets. Nature 461 (7266), 971–975.

Rignot, E., Kanagaratnam, P., 2006. Changes in the velocity structure of the Greenland Ice Sheet. Science 311 (5763), 986.

Scambos, T., Berthier, E., Shuman, C., et al., 2011. The triggering of subglacial lake drainage during rapid glacier drawdown: Crane Glacier, Antarctic Peninsula. Ann. Glaciol. 52 (59), 74.

Scherneck, H., Bos, M., 2002. Ocean Tide and Atmospheric Loading. In: Vandenberg, N. R., Baver, K. D. (Eds.), IVS 2002 General Meeting Proceedings, Tsukuba, Feb. 4-7, 2002. NASA Goddard Space Flight Center, pp. 205–214. URL `ftp://ivscc.gsfc.nasa.gov/pub/general-meeting/2002/pdf/scherneck.pdf`

Schrama, E., Wouters, B., Vermeersen, B., 2011. Present day regional mass loss of Greenland observed with satellite gravimetry. Surv. Geophys., 1–9.

Simpson, M., Milne, G., Huybrechts, P., Long, A., 2009. Calibrating a glaciological model of the Greenland ice sheet from the last Glacial Maximum to present-day using field observations of relative sea level and ice extent. Quaternary Sci. Rev. 28 (17), 1631–1657.

Simpson, M., Wake, L., Milne, G., Huybrechts, P., 2011. The influence of decadal- to millennial-scale ice mass changes on present-day vertical land motion in Greenland: Implications for the interpretation of GPS observations. J. Geophys. Res. 116 (B2), B02406.

Sørensen, L. S., Simonsen, S. B., Nielsen, K., Lucas-Picher, P., Spada, G., Adalgeirsdottir, G., Forsberg, R., Hvidberg, C. S., 2011. Mass balance of the Greenland ice sheet (2003–2008) from ICESat data - the impact of interpolation, sampling and firn density. The Cryosphere 5 (1), 173–186.

Spada, G., Ruggieri, G., Sørensen, L., Nielsen, K., Melini, D., Colleoni, F., 2012. Greenland uplift and regional sea level changes from ICESat observations and GIA modelling. Geophys. J. Int. 189, 1457–1474. URL `http://onlinelibrary.wiley.com/doi/10.1111/j.1365-246X.2012.05443.x/abstract`

Spada, G., Stocchi, P., 2007. SELEN: A Fortran 90 program for solving the“sea-level equation”. Comput. Geosci. 33, 538–562.

Van Den Broeke, M., Bamber, J., Ettema, J., Rignot, E., Schrama, E., Van de Berg, W., Van Meijgaard, E., Velicogna, I., Wouters, B., 2009. Partitioning recent Greenland mass loss. Science 326 (5955), 984–986.

Weidick, A., 1958. Frontal variations at Upernaviks Isstrom in the last 100 years. Gronland Geologiske Undersogelse. Misc. Papers no. 21, Geological Survey of Greenland, Copenhagen.

(III.19)

Williams, S., Bock, Y., Fang, P., Jamason, P., Nikolaidis, R., Prawirodirdjo, L., Miller, M., Johnson, D., 2004. Error analysis of continuous GPS position time series. J. Geophys. Res. 109 (B3), B03412.

Zumberge, J., Heflin, M., Jefferson, D., Watkins, M., Webb, F., 1997. Precise point positioning for the efficient and robust analysis of GPS data from large networks. J. Geophys. Res. 102 (B3), 5005–5017.

Zwally, H., Schutz, R., Bentley, C., Bufton, J., Herring, T., Minster, J., Spinhirne, J., Thomas, R., 2010. GLAS/ICESat L2 Antarctic and Greenland ice sheet altimetry data V031. National Snow and Ice Data Center, Boulder, CO.
URL `ftp://n4ftl01u.ecs.nasa.gov/SAN/GLAS/GLA12.031`

IV

Vertical and horizontal surface displacements near Jakobshavn Isbræ driven by melt-induced and dynamic ice loss

By

Nielsen, K., Khan, S. A., Spada, G., Wahr, J., Bevis, M., Liu, L., and van Dam, T.

Publication details

Submitted to *Journal of Geophysical Research*.

Abstract

We analyze Global Positioning System (GPS) time series of relative vertical and horizontal displacements from 2009 - 2011, at four GPS sites located between ∼5 and ∼150 km from the front of Jakobshavn Isbræ (JI), west Greenland. The horizontal displacements at KAGA, ILUL, and QEQE, relative to the site AASI, are directed towards west-north-west, suggesting that the main mass loss signal is south-east of these sites. The directions of the observed displacements are supported by modelled displacements, derived from NASA's Airborne Topographic Mapper (ATM) surveys of surface elevations from 2006 - 2011. In 2010, we observe a rapid increase in the uplift at all four sites. This uplift anomaly, defined as the deviation at 2010.75 from the 2006 - 2009.75 trend is estimated to 8.8 ± 2.4 mm (KAGA), 9.3 ± 2.2 mm (ILUL), 5.1 ± 2.0 mm (QEQE), and 6.1 ± 2.3 mm (AASI). The relative large anomalies at the sites QEQE and AASI, located

$\sim$150 km from the front of JI, suggests that the uplift anomalies are caused by a large wide-spread melt-induced ice loss. The relatively low uplift anomaly at KAGA, located only 5 km from the front, indicates that there has been a dramatic decrease in dynamic-driven ice loss near the front of JI. This is supported by elevation changes derived from ATM measurements between 2010 and 2011, where we observe an elevation increase in the flow direction of up to 10 m at the frontal part of JI.

Introduction

Jakobshavn Isbræ (JI), located at the west coast of Greenland is one of Greenland's largest outlet glaciers in terms of drainage basin. It has been losing mass at a rate of between 25 Gt/yr and 34 Gt/yr since the end of 2002 (Howat et al., 2011), which is approximately 10 % of Greenland's total ice loss. The present day unloading of ice causes the Earth to respond elastically, thus resulting in both vertical and horizontal deformation of the crust. The vertical deformation pattern is proportional to the load distribution and the pattern of the horizontal field provides information regarding the origin of the load. Hence, by considering the full displacement field, we achieve a better understanding of the ice loss rate and its location.

Presently, more than 50 GPS receivers are located around the edge of the Greenland ice sheet, providing continuous measurements of vertical and horizontal crustal displacements. Here, we use data from four sites (KAGA, ILUL, QEQE, and AASI, Fig IV.1), which are located between 5 and 150 km from the glacier front of JI. The crustal displacements around JI can be divided into three primary contributions: the Earth's elastic response owing to present day ice mass loss from JI; the elastic response as a result of ice mass loss outside JI; and glacial isostatic adjustment (GIA), i.e. the Earth's viscoelastic response to past glacial changes. GPS measurements of crustal displacements have been used previously, in Patagonia (Dietrich et al., 2010), on Svalbard (Sato et al., 2006; Mémin et al., 2011), and in southeast Greenland (Khan et al., 2007), to study the present ice mass variability. Other studies have used GPS measurements to constrain the GIA signal; e.g. in Greenland (Khan et al., 2008; King et al., 2010; Spada et al., 2012) and Antarctica (Thomas et al., 2011).

A previous study conducted by Khan et al. (2010b) used GPS measurements from 2006-2009 to study vertical crustal motion near Jakobshavn Isbræ. Here, we expand the time series with an additional 2 years of data, and analyze both vertical and horizontal GPS displacements. In addition, we analyze inter-annual displacements related to the 2010 melting anomaly (Tedesco et al., 2011; Bevis et al.,

2012) and, based on the uplift pattern, we distinguish between ice loss caused by dynamic thinning and melt-induced ice loss. In general, dynamic thinning is largest near the glacier front (up to 20 m/yr), and decreases to a few m/yr about 20-30 km upstream. Melt-induced thinning is on the order of a few m/yr near the ice margin, and decreases very slowly inland. Consequently, melt-induced thinning can be huge when covering large regions (Van Den Broeke et al., 2009).

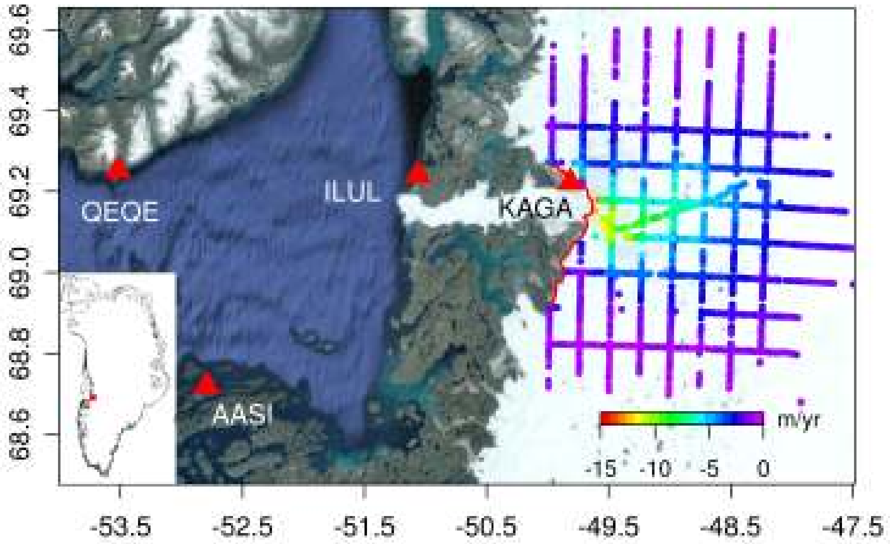

Figure IV.1: An overview of the area of JI. The red triangles indicates the position of the four GPS sites KAGA, ILUL, QEQE, and AASI. The positions of ATM tracks and elevation changes along tracks at 500 m segments, based on ATM data from 2006, 2009, 2010, and 2011 are also shown. The red line indicates the 2006 late summer calving front, acquired from Landsat imagery.

To assess the mass loss of JI, we compare observed and modelled displacement rates. The modelled rates, relating to ice mass loss from JI, derive from surface elevation changes based on NASA's ATM data from 2006, 2009, 2010 and 2011 (Krabill, 2011). Displacements outside JI are estimated from an Ice, Cloud,and land Elevation Satellite (ICESat) derived mass change grid, based on data between 2006 and 2009 (Zwally et al., 2010). We account for the GIA contribution by using the ICE-5G (VM2) deglaciation history of the late-Pleistocene ice sheets (Peltier, 2004).

(IV.3)

Data and Methods

GPS data analysis

To estimate site coordinates we follow the procedure of Khan et al. (2010b). We use the GIPSY OASIS 6.1.2 software package (Zumberge et al., 1997) released in January 2012, and developed at the Jet Propulsion Laboratory (JPL). The orbit products we use were released in 2010 by the International GNNS Service (IGS) (the repro1 products) and include satellite orbits, satellite clock parameters and Earth orientation parameters. The new orbit products take the satellite antenna phase centre offsets into account. Receiver clock parameters are modelled, and the atmospheric delay parameters are modelled using the Global Mapping Function (GMF) (Böhm et al., 2006). Corrections are applied to remove the solid Earth tide and ocean tidal loading. The amplitudes and phases of the main ocean tidal loading terms are calculated using the Automatic Loading Provider (`http://www.oso.chalmers.se/~loading`, Scherneck and Bos (2002)), applied to the TPXO.7.1 ocean tide model (Egbert and Erofeeva, 2002) including correction for center of mass motion of the Earth due to the ocean tides. The site coordinates are computed in the ITRF2005 frame (Altamimi et al., 2007). The secular trends and their uncertainty are estimated as described in Khan et al. (2010b).

Elevation changes

To estimate elevation changes on JI between 2006 and 2011 we use NASA's ATM laser altimetry data (Krabill, 2011) from 2006, 2009, 2010 and 2011 (see Fig IV.1). From these surface elevation data sets we estimate a linear trend along tracks at 500 m segments. To construct an elevation change map of JI, we interpolate the along-track elevation changes on a grid with a resolution of 1×1 km, using ordinary local neighborhood kriging. Based on an area of 7700 km^2 we estimate a volume loss rate of 19.4 ± 5.7 km^3/yr (1σ). The corresponding uncertainty is estimated as the sum of the individual elements in the kriging covariance matrix. Since the considered mass loss is below the equilibrium-line altitude, we use an ice density of 917 kg/m^3 to convert volume loss to mass loss. This results in a mass loss rate of 17.8 ± 5.2 Gt/yr (1σ). The elevation change grid (Fig IV.2) shows a thinning rate of -12 m/yr near the front, which decreases gradually to $\sim$-2 m/yr $\sim$80 km upstream.

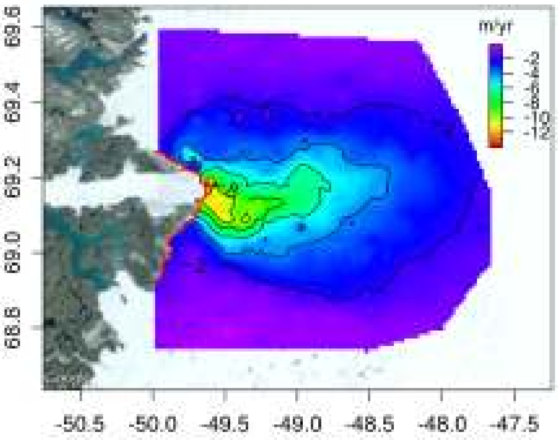

Figure IV.2: Elevation change grid for JI, based on ATM data from 2006, 2009, 2010, and 2011. The red line indicates the 2006 late summer calving front, acquired from Landsat imagery.

Modelled crustal displacement

The horizontal displacement for a disc shaped load as a function of the colatitude α is given by (see e.g. Spada (2003))

$$V(\alpha) = 3\Delta H \left(\frac{\rho_i}{\rho_e}\right) \sum_{n=0}^{n_{max}} l_n \frac{\sigma_n}{2n+1} \frac{\partial P_n(\cos\alpha)}{\partial \alpha}, \tag{IV.1}$$

where ρ_i is the density of ice, ρ_e is the average density of the Earth, ΔH is the ice thickness change, P_n is the Legendre polynomial, n is the harmonic degree, l_n is the nth harmonic component of the horizontal loading deformation coefficient (LDC), and σ_n is the nth harmonic component of the surface load. An expression of σ_n for an axis-symmetric load is found in Spada et al. (2011). Here, we only account for the horizontal displacement $V(\alpha)$. An expression for the vertical displacement $U(\alpha)$ is given by Eq. (4) in Spada et al. (2012). The vertical and horizontal displacements as a function of colatitude are displayed in Fig IV.3. These curves represent the response of a disc load with a radius of 500 m and an ice thickness variation of $\Delta H = -1$ m. The horizontal displacement attains its largest amplitude at the periphery of the load and zero displacement right beneath the load due to symmetry. In the case of unloading, the horizontal motion is directed away from the area with mass loss, and towards in case of mass gain. The displacement curves displayed in Fig IV.3 are based on two different Earth's models a PREM (Dziewonski and Anderson, 1981) and a CRUST2.0-type crust (Bassin et al., 2000) for the area of JI overlying a REF (or STW105) like mantle (Kustowski et al.,

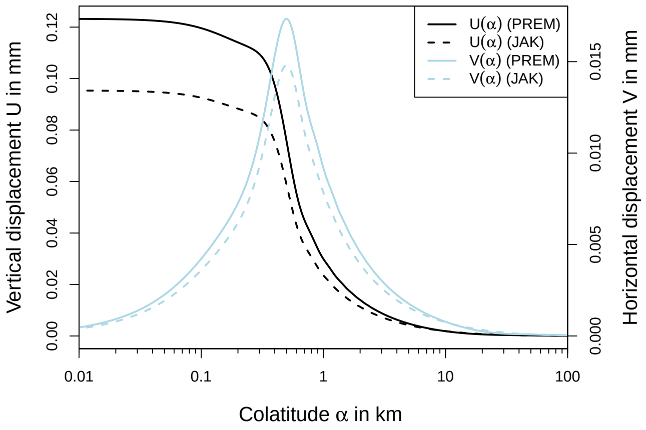

Figure IV.3: Vertical (black curves) and horizontal (blue curves) displacements in response to a disc load with a radius of 500 m (4.5×10^{-3} degrees) and a thickness variation $\Delta H = -1$ m. The solids curves represents an Earth model with PREM structure and the dashed curves represents the JAK Earth model (see Section IV. The displacement estimates are summed up to $n_{max} = 10^5$.

2008), which are discussed in more detail below. We refer to this latter Earth model as JAK.

Crustal displacements due to ice mass loss from Jakobshavn Isbræ

To model the elastic response due to ice mass loss from JI we use elastic LDCs based on the Earth model JAK, where the crustal characteristics are given in Table IV.1. This Earth model has a thicker crust and a lower compressibility in the upper crust compared to the PREM model, which influences the displacement pattern in the near field of the source (see Fig IV.3). The LDCs are estimated by assuming a radially stratified, isotropic and compressible Earth model and they are defined in the Earth's centre of mass reference frame. The vertical h and and horizontal nl LDCs are displayed in Fig IV.4 up to harmonic degree $n = 1024$ (dashed lines). For higher harmonic degrees we assume that the asymptotic value of the LDCs is reached. Hence, for $n \rightarrow \infty$ the horizontal LDC is $nl_\infty = \frac{\gamma m}{4\pi a^2} \frac{1}{\lambda + \mu}$ (Farrell, 1972), where γ is the gravitational acceleration, m and a are the mass and radius of the Earth, λ and μ are the Lamé constants of the uppermost crustal layers. The crustal displacement patterns caused by the ice mass loss of JI are estimated by convolving the mass change grid for JI with the response of a single disc element, where the horizontal part is represented by Eq. (IV.1).

(IV.6)

Table IV.1: Crustal characteristics for the Crust2.0 type Earth model for the area of JI and the average PREM model.

Layer	Thickness	v_p	v_s	ρ
	km	km/s	km/s	kg/cm^3
Crust2.0 type crust for JI				
Ice	0.500	3.810	1.940	0.920
Upper crust	13.000	6.200	3.600	2.800
Middle crust	12.000	6.400	3.600	2.850
Lower crust	12.000	6.800	3.800	2.950
Average PREM crust				
Water	3.000	1.450	0.000	1.020
Crust	12.000	5.800	3.200	2.600
Crust	10.000	6.800	3.900	2.900

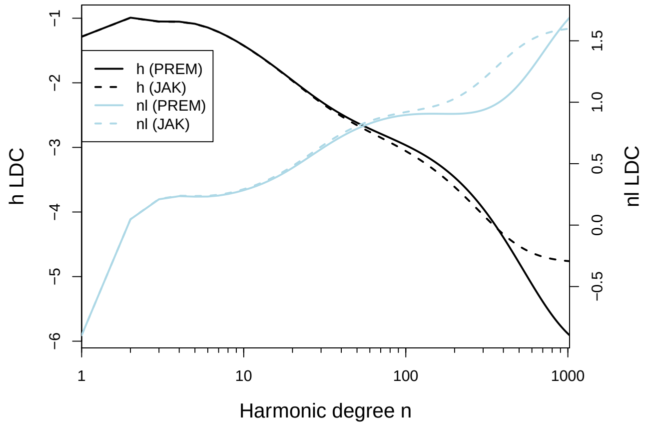

Figure IV.4: Vertical and horizontal LDSs h and l up to harmonic degree $n = 1024$, representing an Earth model with PREM structure (solid lines) and the JAK Earth model (dashed lines).

Crustal displacements due to ice mass loss outside Jakobshavn Isbræ

The elastic displacements caused by ice mass loss from the Greenland ice sheet outside JI are estimated in the same manner as the local contribution, except that a different set of LDCs are used. The LDCs in this estimation are based on an Earth model with PREM structure and are acquired from the Atmospheric pressure loading service (APLO). The vertical h and horizontal nl LDCs are displayed in FigIV.4 up to harmonic degree 1024 (solid lines). To represent the mass changes outside JI, we use an ICESat derived mass change grid based on data from 2006 - 2009, with a spatial resolution of 5 × 5 km. The mass change grid is estimated

(IV.7)

using a method (M3) presented in Sørensen et al. (2011). The time span of this mass change grid is two years shorter than the JI mass change grid, and this difference could contribute an additional error in the displacement estimates from the regional mass changes. To quantify this error, we examine the variation in displacements at the GPS sites located near JI from two additional ICESat derived mass change grids based on data from 2004 - 2007 and 2005 - 2008. When comparing the absolute displacements at each site we find a variation range of approximately ± 0.5 mm and ± 0.2 mm for the relative displacements (with AASI as the reference).

We derive a formal error estimate for the displacements due to uncertainties in the 2006 - 2009 ICESat-derived mass change grid using bootstrapping. We following the procedure described in Sørensen et al. (2011), which is summarize below. The 2006 - 2009 elevation change data set consists of m tracks. From this data set we create 1000 new bootstrapped data sets, by randomly drawing m tracks with replacements among the tracks in the 2006 - 2009 elevation change data set. Hence, in the bootstrapped data sets some tracks might appear more than once. For each bootstrapped data set we estimate the crustal displacements. The 1000 estimates of crustal displacements form a distribution from which the standard deviation is deduced.

Crustal displacements due to GIA

To account for the present day GIA signal, we use the GIA displacement grids based on the ICE-5G(VM2) deglaciation history, which are estimated by W. R. Peltier. The GIA grids are available at `http://www.atmosp.physics.utoronto.ca/~peltier/data.php`. GIA estimates are sensitive to e.g. the viscoelastic structure of the Earth and the deglaciation history.

To assess the variation of GIA estimates due to viscosity, we use an improved version (version 2.9.8) of the software SEa Level EquatioN solver (SELEN) available at `http://www.fis.uniurb.it/spada/SOFT.html` (Spada and Stocchi, 2007). We approximate the VM2 viscosity profile with a two layer mantle model with an upper and lower mantle viscosity of 0.5 and 2.7 $\times 10^{21}$ and let the upper and lower mantle viscosity range between $5\times10^{20\pm0.3}$ Pa s and $2.7\times10^{21\pm0.3}$ Pa s, respectively. Hence, by estimating the GIA contribution within these viscosity bounds we find a range of other possible GIA values.

Results

2010 uplift anomaly

Fig IV.5 shows vertical positions at the GPS sites, where the blue curves represent 30-day averages and their associated uncertainties. The red curves are the sums of the best fitting secular, annual, and semi-annual varying terms for the daily vertical solutions between 2006 and 2009.75. In the first half of 2010, the fitted curves start to deviate from the 30-day averages, indicating an acceleration in uplift. To estimate the 2010 anomaly we use the fitted annual, semi-annual and secular terms, the red curve in Fig IV.5, to predict uplift at 2010.75. The 2010 uplift anomaly is then defined as the difference between the observed and predicted uplift at 2010.75. Hence, the anomaly represents the additional mass loss during the hydrological year 2009-2010. The uplift anomalies at the GPS sites are estimated to be 8.8 ± 2.4 mm (KAGA), 9.3 ± 2.2 mm (ILUL), 5.1 ± 2.0 mm (QEQE), and 6.1 ± 2.3 mm (AASI). Somewhat surprisingly, the spread in the anomalies is quite low. We would intuitively expect the anomaly at KAGA (located less than 5 km from the JI front) to be considerable higher owing to its location. To understand the source of these anomalies we create a simple surface mass balance (SMB) model to represent the 2010 melting event, and estimate the related uplift signals.

Following the melting pattern in the 2010 anomaly map of melting days (Tedesco et al., 2011), we assume that melting occurs up to 75 degrees of latitude on the western side of Greenland, and up to 73 degrees of latitude on the eastern side. Above 70 degrees of latitude melting decreases linearly up to 1500 m altitude, with an ice mass loss of 2.6 m at zero elevation, and below 70 degrees of latitude melting occurs up to 2500 m elevation. The ice loss at zero elevation is chosen so that the total mass loss sums to 300 Gt, which is approximately the SMB anomaly suggested by Tedesco et al. (2011). The SMB model is estimated on a 5 × 5 km grid. Following the method described in Section IV, we estimate the uplift anomalies to be 18.3 mm (KAGA), 9.1 mm (ILUL), 5.3 mm (QEQE), and 6.4 mm (AASI). The observed and modelled anomalies at the sites ILUL, QEQE, and AASI agree very well, while the modelled anomaly at KAGA is too large.

An explanation for this discrepancy could be a decrease in dynamic mass loss near the front of JI. A reduction in ice mass loss near the front will have the largest influence on the elastic uplift signal at KAGA, while the sites further away will be less affected. To test this, we map elevation changes derived from NASA's ATM data between 2010 and 2011. This elevation change map (Fig IV.6 shows a clear reduction in ice loss compared to the trend based on data between 2006 and 2011 (Fig IV.2). The elevation changes between 2010 and 2011 are dominated by a

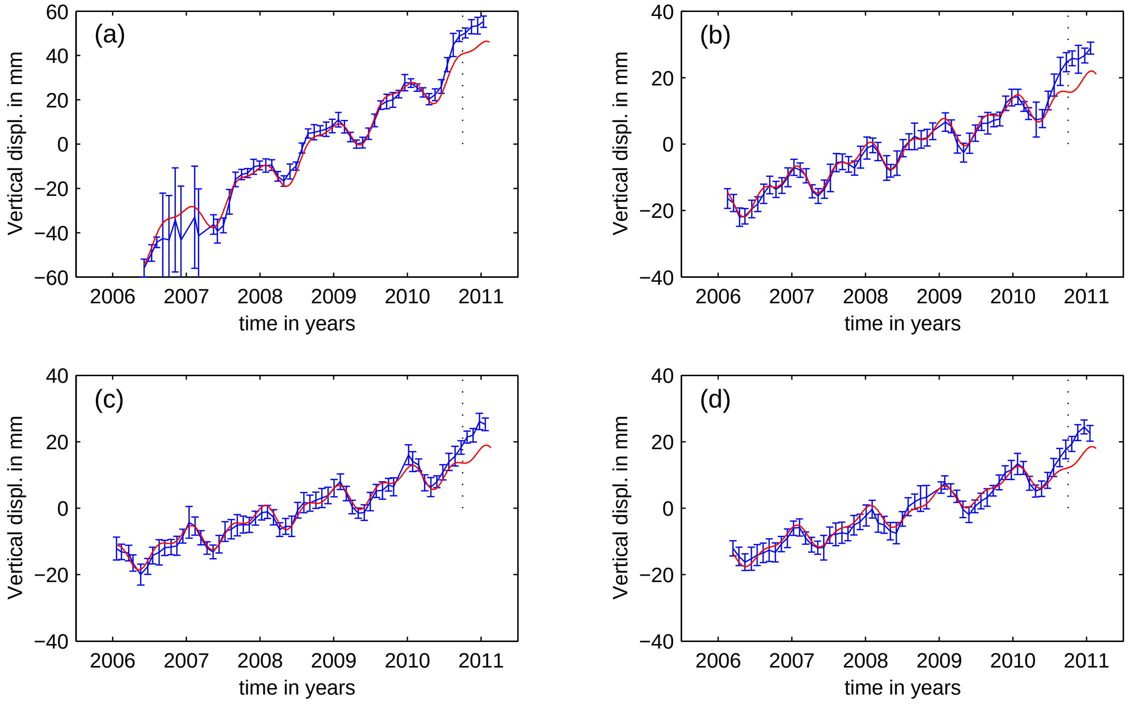

Figure IV.5: 30-day averages of vertical displacements and their associated uncertainties (blue bars) at (a) KAGA, (b) ILUL, (c) QEQE, and (d) AASI. The red curves display the best fitting linear, annual, and semi-annual term, based on data from 2006-2009.75.

more wide-spread thinning pattern compared to the elevation changes between 2006 and 2011 (Fig IV.2). Near the front, we observe an elevation increase of up to 10 m in the flow direction.

Horizontal displacements

To study horizontal displacements we consider relative rather than absolute geocentric displacements. Horizontal displacements are dominated by plate motion, which is effectively removed by considering relative displacements between sites located relatively close to one another. This also reduces displacements related to, for example, ice loss outside JI, and GIA, as these far-field contributions are similar at each GPS site. Thus, the relative rates can be used to validate the local mass balance of JI. The observed displacements rates at KAGA, ILUL, and QEQE, relative to AASI are displayed in Fig IV.7, where the blue dots represent daily solutions between 2006 and 2011. The red lines are the best fitting linear terms.

The modelled and observed rates of crustal displacements, relative to the AASI

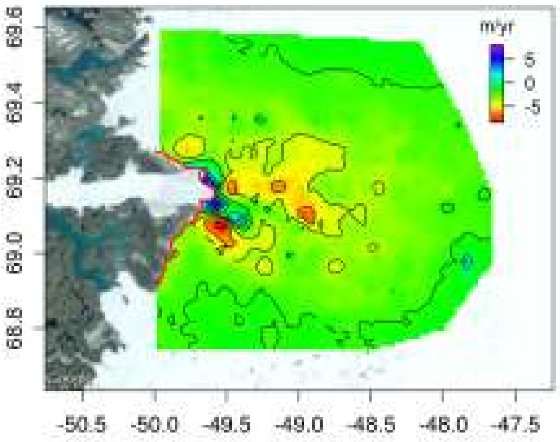

Figure IV.6: Elevation change grid for JI, based on ATM data from 2010 and 2011. The red line indicates the 2011 summer calving front, acquired from Landsat imagery.

site, are summarized in Table IV.2. Column 2 contains observed GPS rates based on data from 2006 - 2011. Column 3 contains the total modelled rates, including contributions from elastic displacements related to mass loss from JI, elastic displacements related to mass loss outside JI, and displacements related to GIA. The discrepancy between the observed and modelled rates is between 0.8 and 0.1 mm/yr for the vertical component, 0.6 and 0.3 mm/yr for the east component, and 0.5 and 0.2 mm/yr for the north component. The vectors in Fig IV.8 display the direction and size of the horizontal displacements at KAGA, ILUL, and QEQE, relative to AASI, where the black and red arrows represent observed and modelled rates, respectively. The horizontal displacements are directed generally towards the west-north-west.

Absolute vertical displacements

The modelled and observed absolute vertical rates are summarized in Table IV.3. Column 2 contains observed GPS rates based on data from 2006 - 2009.75. Column 3 contains the total modelled rates, including contributions from elastic displacements related to mass loss from JI, elastic displacements related to mass loss outside JI, and displacements related to GIA. We find a discrepancy between the observed and modelled rates between 1.5 and 3.1 mm/yr. Assuming that the elastic rates are well captured, the absolute rates can be used to constrain the GIA signal.

(IV.11)

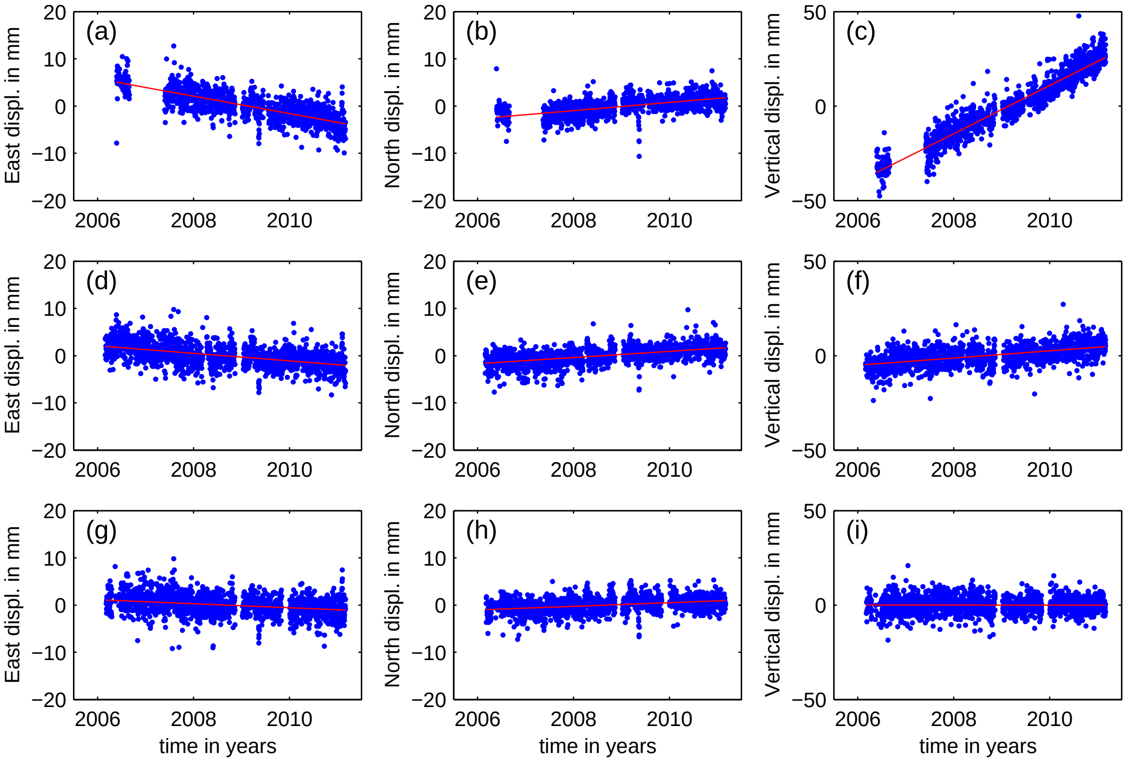

Figure IV.7: Daily values of east, north, and vertical displacements in mm relative to AASI. The annual term is removed. The red curves show the best fitting liner term. (a)-(c) display relative east, north, and vertical displacements at KAGA, respectively. (d)-(f) display relative east, north, and vertical displacements at ILUL. (g)-(h) display relative east, north, and vertical displacements at QEQE.

Discussion and conclusions

We have analyzed GPS time series of vertical and horizontal displacements from 2006 - 2011 at the sites KAGA, ILUL, and QEQE, relative to AASI, to study the displacement pattern and assess the mass loss estimate of JI. The overall good agreement between the observed and modelled displacements suggest that the mass loss signal from JI is well captured. The horizontal displacements are directed towards the west-north-west, indicating that the main part of the mass loss occurs south of the sites KAGA, ILUL, and QEQE, since the horizontal motion points away from an area with mass loss. This agrees well with the elevation change grid based on ATM measurements (Fig IV.2).

When comparing our modelled vertical rates to those estimated in Khan et al. (2010b) we have improved the agreement between the observed and modelled rates, both for the absolute and the relative displacements. The major difference

Table IV.2: Observed and modelled vertical and horizontal displacements at the sites KAGA, ILUL, and QEQE relative to AASI. The second column displays GPS rates, third column the total modelled uplift rates, consisting of the elastic response from JI (column 4), the elastic response from outside JI (column 5), and GIA (column 6). The observed rates are based on data from 2006-2011. The GIA estimates are based on ICE-5G(VM2). All rates are given in mm/yr. The errors represent one standard deviation σ, except for the GIA estimates, where ranges are given instead. These ranges represent viscosity variations corresponding to $5\times10^{20\pm0.3}$ Pa s and $2.7\times10^{21\pm0.3}$ Pa s, for the upper and lower mantles,respectively.

Station	GPS	Modelled total	Response of JI	Response outside JI	GIA	
			Vertical component U			
KAGA-AASI	12.8 ± 0.6	12.0 ± 2.1	11.4 ± 2.1	1.8 ± 0.4	-1.2	(-0.6;1.1)
ILUL-AASI	1.9 ± 0.4	2.1 ± 0.9	1.7± 0.8	0.9 ± 0.3	-0.5	(-0.5;0.8)
QEQE-AASI	-0.1 ± 0.4	-0.2 ± 0.5	-0.2 ± 0.4	-0.1 ± 0.3	0.1	(-0.6;0.5)
			East component E			
KAGA-AASI	-1.8 ± 0.3	-2.1 ± 0.5	-3.1 ± 0.5	0.4 ± 0.1	0.6	(-0.6;0.5)
ILUL-AASI	-0.8 ± 0.2	-0.2 ± 0.3	-0.6 ± 0.3	0.0 ± 0.1	0.4	(-0.2;0.4)
QEQE-AASI	-0.4 ± 0.2	0.0 ± 0.1	0.1 ± 0.1	0.1 ± 0.1	-0.2	(-0.2;0.0)
			North component N			
KAGA-AASI	0.9 ± 0.3	0.3 ± 0.1	0.5 ± 0.1	0.0 ± 0.1	-0.2	(-0.1;0.2)
ILUL-AASI	0.7 ± 0.2	0.2 ± 0.1	0.3 ± 0.1	0.0 ± 0.1	-0.1	(-0.1;0.1)
QEQE-AASI	0.4 ± 0.2	0.1 ± 0.1	0.2 ± 0.1	-0.1 ± 0.0	0.0	(0.0;0.0)

is the treatment of the mass loss outside JI. In Khan et al. (2010b), the elastic rates, as a result of mass loss outside JI, are derived from a mass balance model based on Gravity Recovery and Climate Experiment (GRACE) data (Velicogna, 2009), whereas here we use a high resolution (5 × 5 km) mass balance model derived from ICESat data. With this model we obtain a much more detailed mass change pattern than can be obtained with GRACE data. This is important in terms of the elastic displacement in the near field of a GPS receiver, since a small disc will produce a larger elastic signal compared to a larger disc, assuming that the discs contain the same mass. This demonstrates the importance of using a high resolution loading model to fully capture the elastic response from nearby sources.

To estimate the uplift related to the 2010 melting anomaly, we have analyzed GPS time series of vertical displacements. The 2010 melting anomaly is clearly visible in the GPS time series (Fig IV.5), in terms of a pronounced deviation from the underlying trend, starting in the first half of 2010. The anomaly is present even at

(IV.13)

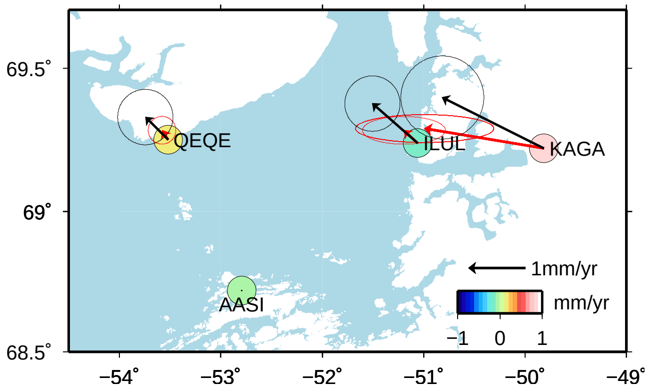

Figure IV.8: Observed (black) and modelled (red) horizontal displacements relative to AASI including contributions from the elastic response from JI, the elastic response from outside JI, and GIA. The arrows indicate the direction and size of the displacements and the ellipses indicate the 95 % confidence intervals. The colors of the circles represents the offset between the observed and modelled vertical displacements relative to AASI.

Table IV.3: Modelled and observed uplift rates in mm/yr at the GPS sites KAGA, ILUL, QEQE, and AASI. The second column displays GPS rates, third column the total modelled uplift rates, consisting of the elastic response from JI (column 4), the elastic response from outside JI (column 5), and GIA (column 6). The observed rates are based on data from 2006 - 2009.75. The errors represent one standard deviation σ, except for the GIA estimates, where ranges are given instead. These ranges represent viscosity variations corresponding to $5\times10^{20\pm0.3}$ Pa s and $2.7\times10^{21\pm0.3}$ Pa s, for the upper and lower mantles,respectively.

Station	GPS	Modelled total	Response of JI	Response outside JI	GIA	
KAGA	18.6 ± 0.7	15.5 ± 2.1	12.7 ± 2.1	4.5 ± 0.3	-1.7	(-3.2;3.6)
ILUL	7.1 ± 0.5	5.6 ± 0.7	3.0 ± 0.7	3.6 ± 0.2	-1.0	(-3.2;3.3)
QEQE	6.1 ± 0.5	3.3 ± 0.3	1.1 ± 0.2	2.7 ± 0.2	-0.5	(-2.3;2.1)
AASI	5.9 ± 0.5	3.6 ± 0.4	1.3 ± 0.3	2.7 ± 0.2	-0.4	(-2.8;2.6)

the sites furthest from the front of JI; e.g. at AASI we estimate the anomaly to be 6.1 mm. This indicates that the 2010 anomaly was a large and wide-spread melting event, primarily in terms of melting from the surface, and was not caused by an increased dynamic signal. For instance, the mass loss pattern of the Greenland ice sheet derived from ICESat data between 2006 and 2009, only causes an uplift of 3.7 mm at AASI. The anomaly of 8.8 mm at KAGA is smaller than expected considering its location. This is most likely a result of a considerable decrease in the dynamic signal on JI. The thinning pattern of JI has changed dramatically during 2010 to 2011 (Fig IV.6) compared to previous years (Joughin et al., 2008; Khan et al., 2010b). During this period, we observe an elevation increase of up to 10 m in the flow direction of JI. This is consistent with observed decrease in the ice-flow velocity during 2010 - 2011 relative to 2009 - 2010 (Joughin et al., 2012)

Furthermore, we compare observed and modelled vertical displacement rates, where we find a discrepancy of 3.1 mm/yr (KAGA), 1.5 mm/yr (ILUL), 2.8 mm/yr (QEQE), and 2.3 mm/yr (AASI). These discrepancies may originate from various sources, such as errors in the elastic rates related to unmodelled mass loss outside JI, errors related to GPS, and errors in the GIA rates owing to inaccuracies in the ice history and viscosity profile. The fact that the offsets are of similar size suggests that the error might be caused by a long wavelength signal e.g. GIA. For instance, we have demonstrated that the GIA estimates may vary with more than 2-3 mm in each direction, by varying the viscosity of the upper and lower mantles. Hence the GIA estimates are not particularly well determined at these sites.

At the moment, 55 permanent GPS receivers, most of which are part of the Greenland GPS network (GNET), are measuring the crustal displacements continuously around the edge of the Greenland ice sheet. Potentially, horizontal displacements may be an important supplement to the vertical displacements, since these motions contribute information about the origin of the mass loss. This information can be particularly valuable in areas with a more complex mass loss pattern, such as the southeast coast of Greenland where the mass loss results from many different glacier types and inland thinning.

Acknowledgments

We thank Louise S. Sørensen for providing the ICESat mass change grids and Pascal Gegout for the elastic LDCs and the corresponding elastic Earth model. Work done by Karina Nielsen and Shfaqat Abbas Khan was partly funded by KVUG. GNET is supported by the Arctic Sciences Division of the U.S. National Science Foundation.

(IV.16)

Bibliography

Altamimi, Z., Collilieux, X., Legrand, J., Garayt, B., Boucher, C., 2007. ITRF2005: A new release of the International Terrestrial Reference Frame based on time series of station positions and Earth Orientation Parameters. J. Geophys. Res. 112 (B9), B09401.

Bassin, C., Laske, G., Masters, G., 2000. The current limits of resolution for surface wave tomography in North America. EOS, Trans. Am. Geophys. Un. 81, F897.

Bevis, M., Wahr, J., Khan, S., Madsen, F., Brown, A., Willis, M., Kendrick, E., Knudsen, P., Box, J., van Dam, T., et al., 2012. Bedrock displacements in Greenland manifest ice mass variations, climate cycles and climate change. P. Natl. Acad. Sci. USA.

Böhm, J., Niell, A., Tregoning, P., Schuh, H., 2006. Global Mapping Function (GMF): A new empirical mapping function based on numerical weather model data. Geophys. Res. Lett. 33 (7), L07304.

Dietrich, R., Ivins, E., Casassa, G., Lange, H., Wendt, J., Fritsche, M., 2010. Rapid crustal uplift in Patagonia due to enhanced ice loss. Earth Planet. Sc. Lett. 289 (1-2), 22–29.

Dziewonski, A., Anderson, D., 1981. Preliminary reference Earth model. Phys. Earth Planet. In. 25 (4), 297–356.

Egbert, G., Erofeeva, S., 2002. Efficient inverse modeling of barotropic ocean tides. J. of Atmos. Ocean. Tech. 19 (2), 183–204.

Farrell, W., 1972. Deformation of the Earth by surface loads. Rev. Geophys. 10 (3), 761–797.

Howat, I. M., Ahn, Y., Joughin, I., van den Broeke, M. R., Lenaerts, J. T. M., Smith, B., 2011. Mass balance of Greenland's three largest outlet glaciers, 2000-2010. Geophys. Res. Lett. 38, L12501.

Joughin, I., Howat, I., Fahnestock, M., Smith, B., Krabill, W., Alley, R., Stern, H., Truffer, M., 2008. Continued evolution of Jakobshavn Isbrae following its rapid speedup. J Geophys Res 113 (F4), F04006.

Joughin, I., Smith, B., Howat, I., Floricioiu, D., Alley, R., Truffer, M., Fahnestock, M., 2012. Seasonal to decadal scale variations in the surface velocity of Jakobshavn Isbrae, Greenland: Observation and model-based analysis. J. Geophys. Res. 117 (F2), F02030.

Khan, S., Liu, L., Wahr, J., Howat, I., Joughin, I., van Dam, T., Fleming, K., 2010b. GPS measurements of crustal uplift near Jakobshavn Isbræ due to glacial ice mass loss. J. Geophys. Res. 115 (B9), B09405.

Khan, S., Wahr, J., Leuliette, E., van Dam, T., Larson, K., Francis, O., 2008. Geodetic measurements of postglacial adjustments in Greenland. J. Geophys. Res. 113 (B2), B02402.

Khan, S., Wahr, J., Stearns, L., Hamilton, G., van Dam, T., Larson, K., Francis, O., 2007. Elastic uplift in southeast Greenland due to rapid ice mass loss. Geophys. Res. Lett. 34 (21), L21701.

King, M., Altamimi, Z., Boehm, J., Bos, M., Dach, R., Elosegui, P., Fund, F., Hernández-Pajares, M., Lavallee, D., Mendes Cerveira, P., et al., 2010. Improved constraints on models of glacial isostatic adjustment: a review of the contribution of ground-based geodetic observations. Surv. Geophys., 1–43.

Krabill, W. B., 2011. IceBridge ATM L2 Icessn Elevation, Slope, and Roughness, [1994-2011]. Boulder, Colorado USA: NASA Distributed Active Archive Center at the National Snow and Ice Data Center. Digital media.
URL `http://nsidc.org/data/ilatm2.html`

Kustowski, B., Ekström, G., Dziewonski, A., 2008. Anisotropic shearwave velocity structure of the Earth's mantle: a global model. J. geophys. Res. 113 (10.1029).

Mémin, A., Rogister, Y., Hinderer, J., Omang, O., Luck, B., 2011. Secular gravity variation at Svalbard (Norway) from ground observations and GRACE satellite data. Geophysical Journal International 184 (3), 1119–1130.

Peltier, W., 2004. Global glacial isostasy and the surface of the ice-age Earth: the ICE-5G (VM2) model and GRACE. Annu. Rev. Earth Planet. Sci. 32, 111–149.

Sato, T., Okuno, J., Hinderer, J., MacMillan, D., Plag, H., Francis, O., Falk, R., Fukuda, Y., 2006. A geophysical interpretation of the secular displacement and gravity rates observed at Ny-ålesund, Svalbard in the Arctic-effects of post-glacial rebound and present-day ice melting. Geophys. J. Int. 165 (3), 729–743.

Scherneck, H., Bos, M., 2002. Ocean Tide and Atmospheric Loading. In: Vandenberg, N. R., Baver, K. D. (Eds.), IVS 2002 General Meeting Proceedings, Tsukuba, Feb. 4-7, 2002. NASA Goddard Space Flight Center, pp. 205–214.
URL `ftp://ivscc.gsfc.nasa.gov/pub/general-meeting/2002/pdf/scherneck.pdf`

Sørensen, L. S., Simonsen, S. B., Nielsen, K., Lucas-Picher, P., Spada, G., Adalgeirsdottir, G., Forsberg, R., Hvidberg, C. S., 2011. Mass balance of the Greenland ice sheet (2003–2008) from ICESat data - the impact of interpolation, sampling and firn density. The Cryosphere 5 (1), 173–186.

Spada, G., 2003. The theory behind TABOO. Samizdat Press, Golden-White River Junction.
URL `http://samizdat.mines.edu/taboo/`

Spada, G., Barletta, V., Klemann, V., Riva, R., Martinec, Z., Gasperini, P., Lund, B., Wolf, D., Vermeersen, L., King, M., 2011. A benchmark study for glacial isostatic adjustment codes. Geophys J Int 185, 106–132.

Spada, G., Ruggieri, G., Sørensen, L., Nielsen, K., Melini, D., Colleoni, F., 2012. Greenland uplift and regional sea level changes from ICESat observations and GIA modelling. Geophys. J. Int. 189, 1457–1474.
URL `http://onlinelibrary.wiley.com/doi/10.1111/j.1365-246X.2012.05443.x/abstract`

Spada, G., Stocchi, P., 2007. SELEN: A Fortran 90 program for solving the“sea-level equation”. Comput. Geosci. 33, 538–562.

Tedesco, M., Fettweis, X., Van den Broeke, M., Van de Wal, R., Smeets, C., van de Berg, W., Serreze, M., Box, J., 2011. The role of albedo and accumulation in the 2010 melting record in Greenland. Environ. Res. Lett. 6, 014005.

Thomas, I., King, M., Bentley, M., Whitehouse, P., Penna, N., Williams, S., Riva, R., Lavallee, D., Clarke, P., King, E., et al., 2011. Widespread low rates of Antarctic glacial isostatic adjustment revealed by GPS observations. Geophys. Res. Lett. 38 (22), L22302.

Van Den Broeke, M., Bamber, J., Ettema, J., Rignot, E., Schrama, E., Van de Berg, W., Van Meijgaard, E., Velicogna, I., Wouters, B., 2009. Partitioning recent Greenland mass loss. Science 326 (5955), 984–986.

Velicogna, I., 2009. Increasing rates of ice mass loss from the Greenland and Antarctic ice sheets revealed by GRACE. Geophys Res Lett 36 (19), L19503.

Zumberge, J., Heflin, M., Jefferson, D., Watkins, M., Webb, F., 1997. Precise point positioning for the efficient and robust analysis of GPS data from large networks. J. Geophys. Res. 102 (B3), 5005–5017.

Zwally, H., Schutz, R., Bentley, C., Bufton, J., Herring, T., Minster, J., Spinhirne, J., Thomas, R., 2010. GLAS/ICESat L2 Antarctic and Greenland ice sheet altimetry data V031. National Snow and Ice Data Center, Boulder, CO.
URL `ftp://n4ftl01u.ecs.nasa.gov/SAN/GLAS/GLA12.031`